



Title	Study on Synthesis and Photo-functionalization of Magnetic Semiconductor Lanthanide Nanocrystals
Author(s)	川島, 祥
Citation	北海道大学. 博士(工学) 甲第12062号
Issue Date	2015-12-25
DOI	10.14943/doctoral.k12062
Doc URL	http://hdl.handle.net/2115/60472
Type	theses (doctoral)
File Information	Akira_Kawashima.pdf



[Instructions for use](#)

Study on Synthesis and Photo-functionalization of Magnetic Semiconductor Lanthanide Nanocrystals

磁性半導体希土類ナノ結晶の合成と
光機能化に関する研究

Akira Kawashima

December 2015

Graduate School of Chemical Sciences and Engineering
Hokkaido University

Contents

Chapter 1

General Introduction **5**

- 1.1 Lanthanide Materials
- 1.2 Lanthanide Magnetic Semiconductors
- 1.3 Magneto-optical Properties
- 1.4 Nanomaterials
- 1.5 Europium Chalcogenide Nanocrystals
- 1.6 Nanoaggregates
- 1.7 Objectives
- 1.8 Contents of This Thesis
- 1.9 References

Chapter 2

EuS Nano-assemblies Linked with Photo-functional Naphthalenedithiols **31**

- 2.1 Introduction
- 2.2 Experiments
- 2.3 Results and Discussion

2.4 Conclusions

2.5 References

Chapter 3

Enhanced Magneto-optical Properties of Semiconductor EuS Nanocrystals Assisted by Surface Plasmon Resonance of Gold Nanoparticles

59

3.1 Introduction

3.2 Experiments

3.3 Results and Discussion

3.4 Conclusions

3.5 References

Chapter 4

Photo-switchable Faraday Effect in EuS-Au Nanosystems

99

4.1 Introduction

4.2 Experiments

4.3 Results and Discussion

4.4 Conclusions

4.5 References

Chapter 5

Terbium Oxide, Fluoride, and Oxyfluoride Nanocrystals with Magneto-optical Properties

115

5.1 Introduction

5.2 Experiments

5.3 Results and Discussion

5.4 Conclusions

5.5 References

Chapter 6

Summary

144

List of Publications

148

Acknowledgement

151

Chapter 1

General Introduction

1.1 Lanthanide Materials

Lanthanide (Ln) elements have attracted the attention of researchers for decades^[1-11]. They are characterized by gradual filling of 4f orbitals from $4f^0$ (for La) to $4f^{14}$ (Lu). Given that the 4f orbitals are shielded from the surrounding environment by the filled $5s^2$ and $5p^2$ orbitals, the characteristic properties of lanthanide ions, such as optical, electronic, magnetic, and catalytic, are largely independent of their environment. Hence, lanthanide elements have been widely used in many fields (Figure 1-1 and Table 1-1). For example, europium, terbium, samarium, and thulium are widely used as luminescent elements in displays and fluorescent lights. Ytterbium, neodymium, and erbium are known for their near-infrared luminescence. Compounds of neodymium and dysprosium are well-known as the strongest permanent magnets and are used in electric motors, computer hard drive spindles, cell phones, and actuators. Cerium compounds have excellent catalytic properties.

Table 1-1. Electronic structure of the lanthanide.

Element	Symbol	Atomic number	Configuration Ln atom	Configuration Ln(III)
Lanthanum	La	57	[Xe] 5d ¹ 6s ²	[Xe]
Cerium	Ce	58	[Xe] 4f ¹ 5d ¹ 6s ²	[Xe] 4f ¹
Praseodymium	Pr	59	[Xe] 4f ³ 6s ²	[Xe] 4f ²
Neodymium	Nd	60	[Xe] 4f ⁴ 6s ²	[Xe] 4f ³
Promethium	Pm	61	[Xe] 4f ⁵ 6s ²	[Xe] 4f ⁴
Samarium	Sm	62	[Xe] 4f ⁶ 6s ²	[Xe] 4f ⁵
Europium	Eu	63	[Xe] 4f ⁷ 6s ²	[Xe] 4f ⁶
Gadolinium	Gd	64	[Xe] 4f ⁷ 5d ¹ 6s ²	[Xe] 4f ⁷
Terbium	Tb	65	[Xe] 4f ⁹ 6s ²	[Xe] 4f ⁸
Dysprosium	Dy	66	[Xe] 4f ¹⁰ 6s ²	[Xe] 4f ⁹
Holmium	Ho	67	[Xe] 4f ¹¹ 6s ²	[Xe] 4f ¹⁰
Erbium	Er	68	[Xe] 4f ¹² 6s ²	[Xe] 4f ¹¹
Thulium	Tm	69	[Xe] 4f ¹³ 6s ²	[Xe] 4f ¹²
Ytterbium	Yb	70	[Xe] 4f ¹⁴ 6s ²	[Xe] 4f ¹³
Lutetium	Lu	71	[Xe] 4f ¹⁴ 5d ¹ 6s ²	[Xe] 4f ¹⁴

1.2 Lanthanide Magnetic Semiconductors

In this study, the author focused on the lanthanide magnetic semiconductors. Magnetic semiconductors work based on interaction between light and magnetic field in a medium (Figure 1-2). Their magnetic properties can be controlled using optical excitation (opto-magnetic effect), and the optical properties of magnetic semiconductors can be controlled using an external magnetic field (magneto-optical effect). Such characteristic properties are induced by interactions between electric charge and magnetic spin.

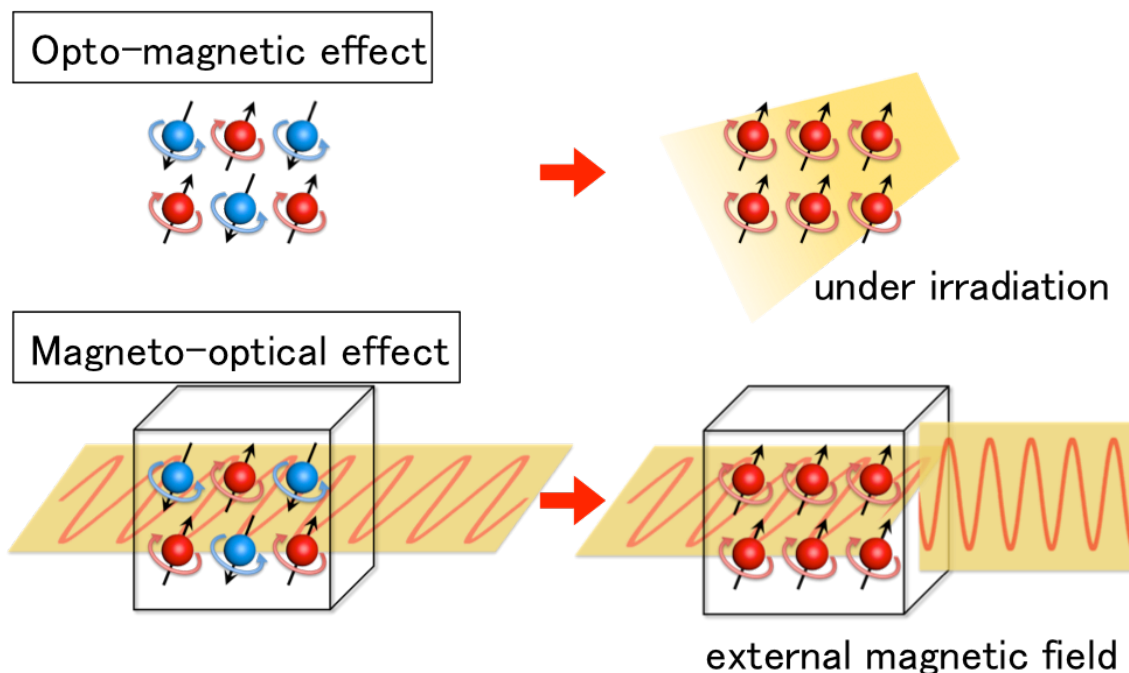


Figure 1-2. Schematic illustrations of opto-magnetic and magneto-optical effects.

Europium chalcogenides (EuX; X = O, S, Se, and Te), among other materials, are lanthanide magnetic semiconductors^[12-18]. EuX have the NaCl structure, and they are magnetic semiconductors, characterized by degenerate 4*f* orbitals of Eu(II) ions existing between the conduction band (5*d* orbitals of Eu(II)) and the valence band (*p* orbitals of O²⁻, S²⁻, Se²⁻, or Te²⁻) (Figure 1-3). The 4*f*-5*d* electronic transition and spin configuration of EuX lead to a large magneto-optical effect. Among EuXs, EuS is distinctly characterized by its ferromagnetic properties with Curie temperature ($T_c = 16.6$ K), which makes it a promising candidate for use as an active material in magneto-optic devices.

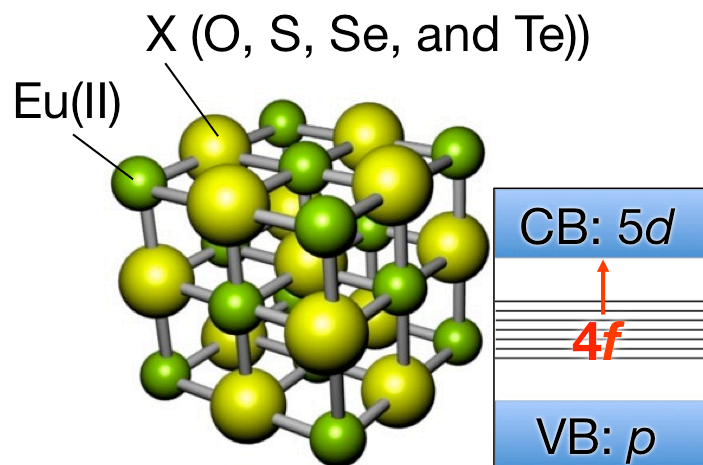


Figure 1-3. Schematic illustrations of crystal structure of europium chalcogenides and the 4*f*-5*d* electronic transition.

1.3 Magneto-optical Properties

The Faraday effect, a magneto-optical effect, causes rotation of the plane of polarized light, and the amount of rotation is linearly proportional to the magnetic field component along the direction of propagation (Figure 1-4). This phenomenon is caused by the propagation of right and left circularly polarized light at different speeds. Linearly polarized light can be decomposed into a superposition of two equal-amplitude right and left circularly polarized light components. In the passage of linearly polarized light through a material acted upon by an external magnetic field, if one of these circularly polarized light components is slowed more than the other, the effect of relative phase difference rotates the orientation of linearly polarized light by an angle θ as follows:

$$\theta = VHI \quad (1-1)$$

where V is the Verdet constant, H is the external magnetic field, and l is the length of the path. The Verdet constant is a proportionality constant that varies according to the wavelength of light and the temperature of the materials.

The Faraday effect is the basis of optical isolators and optical circulators. These optical devices are required in optical communication systems and laser applications^[19-29].

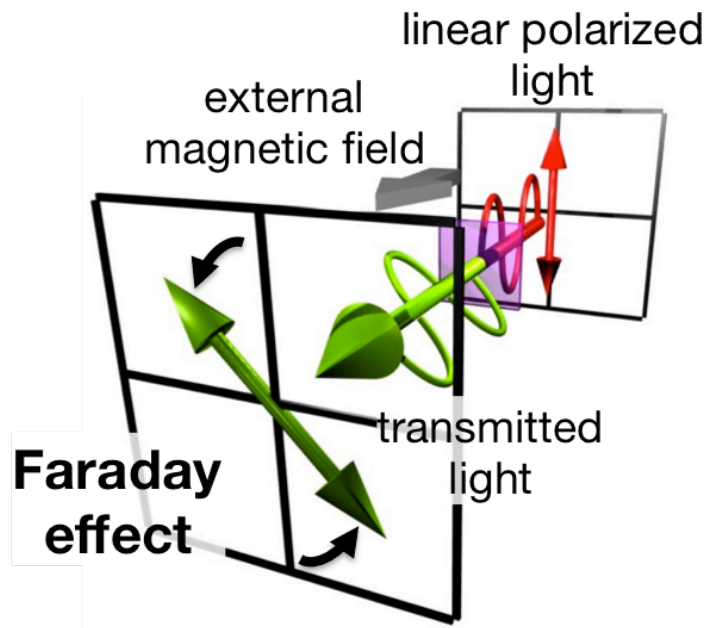


Figure 1-4. A schematic illustration of Faraday effect.

1.4 Nanomaterials

Nanomaterials frequently show intermediate behavior between macroscopic solid and atomic or molecular systems. A variety of materials (metal, semiconductor, polymer, and carbon) and nanostructures (nanocrystal, nanorod, nanowire, and nanoplane) have been studied^[30-40]. In particular, semiconductor nanocrystals have attracted considerable interest because of their characteristic physical features such as optical, magnetic, electronic, and catalytic. These characteristic features can be scribed to several reasons. One is the surface effect caused by an increase in the number of atoms on a nanocrystals surface compared to the total number of atoms in the nanocrystal. Therefore, surface atoms have a large influence on the overall properties of nanocrystals. For example, an increase in the number of surface atoms on a nanocrystal surface can lead to heightened chemical reactivity and low melting point compared to the corresponding bulk solid. The other reason is the quantum size effect, according to which the energy level of a semiconductor nanocrystals can be regarded as a hybrid between the energy levels of small molecules and the corresponding bulk material (Figure 1-5)^[41]. In contrast to bulk materials, the energy levels of a semiconductor nanocrystal are discrete, and their band gap is larger. However, their density of state is much higher, and their spacing is smaller than that of the corresponding levels of one atom or a small atomic cluster.

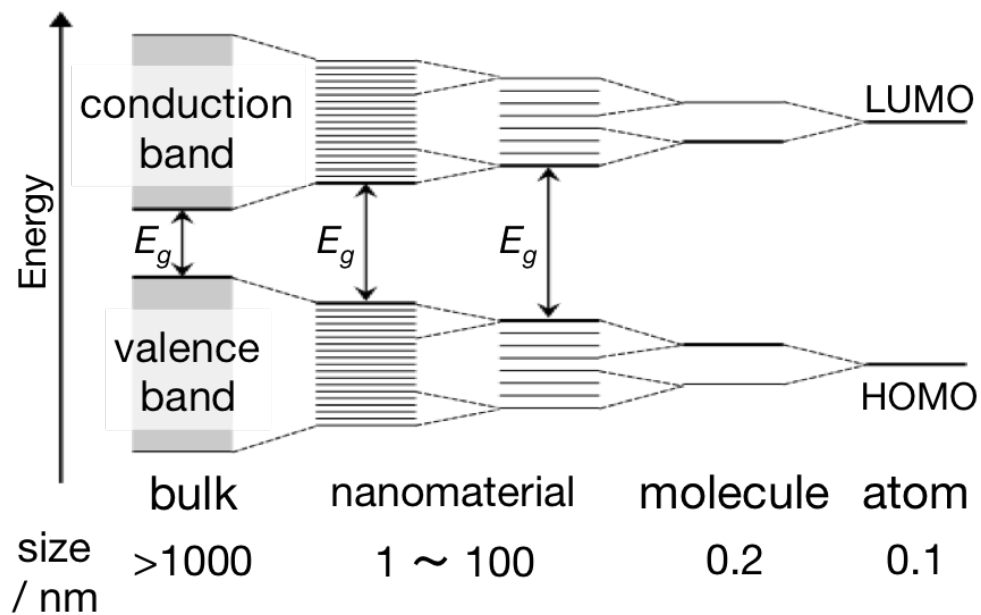


Figure 1-5. A schematic illustration of the quantum size effect.

The magnetic properties of nanocrystals are different from molecules and bulk materials as well, and they strongly depend on nanocrystal size^[42]. If the crystal size is large enough to support a multidomain structure, magnetization reversal occurs via a domain walls motion. In contrast, a small magnetic nanocrystal is a single-domain magnet. This shows that the direction of magnetization can be changed only by coherent rotation of spins, and such a change results in single-domain particles having higher coercivity than multidomain particles. Upon a further decrease in the particle size, the coercivity decreases because of the progressively increasing role of thermal fluctuations, leading to superparamagnetism.

Magnetic semiconductor nanocrystals have both semiconducting and magnetic properties. To manipulate their magneto-optical properties, various types of structured magnetic semiconductor nanocrystals have been prepared, and stochastic control for a number of magnetic dopants in II–VI or III–V semiconductor nanocrystals has been investigated^[24,43,44]. However, the characteristic magneto-optical properties of nanocrystals have not been studied extensively because there are only few classes of materials that exhibit both intrinsic magnetic and semiconducting properties.

1.5 Europium Chalcogenide Nanocrystals

Here, the author focused on lanthanide nanocrystals composed of photo- and magneto-functional lanthanide ions as the intrinsic magnetic semiconductors. In particular, EuX nanocrystals were synthesized, and their resulting magnetic and magneto-optical properties were explored.

Bulk EuO and EuS can be prepared by solid-phase reactions of europium with chalcogens at high temperatures ($> 1000^{\circ}\text{C}$). However, chemical and physical instability of their surfaces constitute an obstacle to the synthesis and isolation of europium chalcogenide nanocrystals. To prepare europium chalcogenide nanocrystals, Hasegawa and co-workers reported the liquid-phase reactions of europium in liquid ammonia (Figure 1-6a)^[45-48]. Recently, they successfully synthesized monodisperse EuX nanocrystals via thermal decomposition of Eu(III) complexes as single-source precursors^[49-52]. In this method, a suitable capping reagent is decomposed to synthesize nanocrystals (Figure 1-6b). Currently, various types of single-source precursor for the preparation of EuX nanocrystals and their photophysical and magnetic properties have been reported^[53-67]. Their characteristic photophysical and magneto-optical properties in the visible region have been observed. It has been found that the energy level of a conduction band constructed from $5d$ orbitals is affected by the size of nanocrystals, as is the case with other semiconductor nanocrystals.

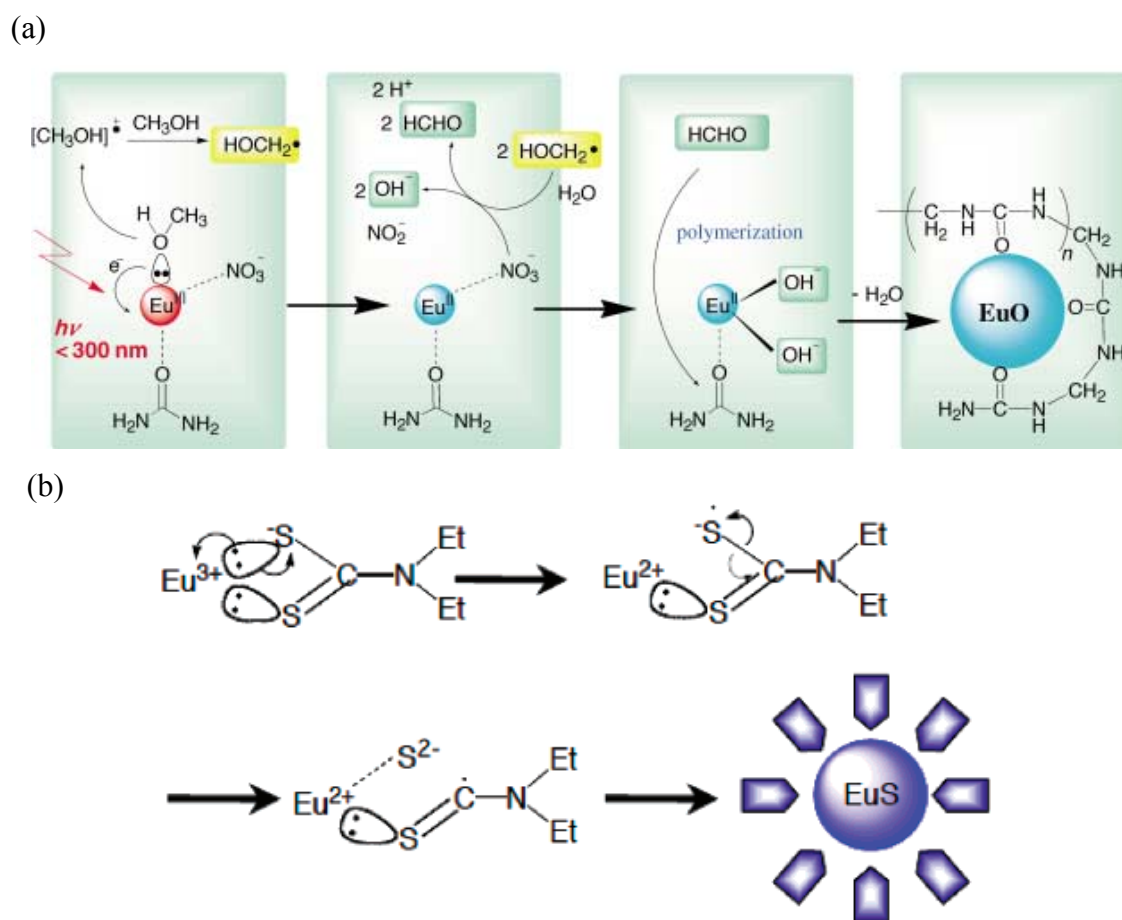


Figure 1-6. Mechanism of (a) the liquid-phase reactions of Eu(III) in liquid ammonia^[46], and (b) the thermal decomposition of Eu(III) complexes as single-source precursors^[51].

1.6 Nanoaggregates

Recently, nano-assemblies composed of semiconductor, metal, or magnetic nanocrystals have been studied extensively for potential applications in fields such as optoelectronics, nanoelectronics, storage systems, biological labels, and three-dimensional waveguides^[68-72]. These nanocrystals can be used as “building blocks” for larger nano-assemblies (Figure 1-7), and they show not only enhanced physical properties but also the emergence of novel physical properties due to the interactions between nanocrystals. For example, Koole and co-workers reported effective exciton energy transfer and electronic coupling of aggregates of semiconductor CdTe nanocrystals in solution (Figure 1-8)^[71]. Kelley and co-workers observed drastic red-shifts of absorption and emission bands of nanosized aggregates composed of semiconductor GaSe nanocrystals^[69]. Chaudret and co-workers reported on the formation and magnetic properties of superlattice structures comprising cubic iron nanocrystals^[70]. Talapin and co-workers reported self-assembled binary superlattices of CdSe and Au nanocrystals, and their changed fluorescence properties^[72].

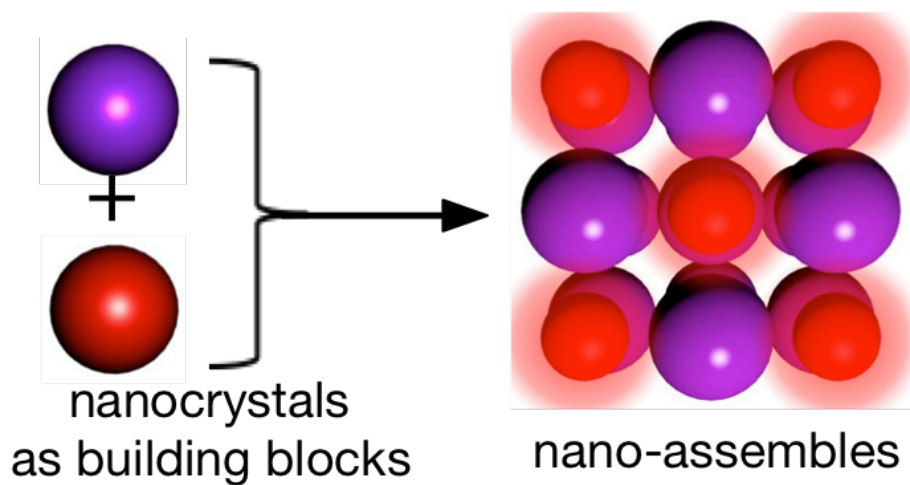


Figure 1-7. A schematic illustration of nano-assemblies.

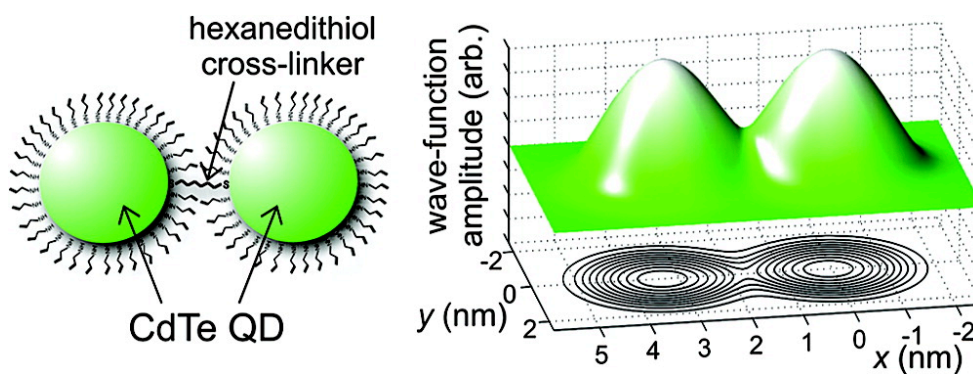


Figure 1-8. A schematic illustration of CdTe nano-assemblies linked by hexanedithiol, and contour-plot of the electron wave functions in two neighboring nanocrystals.

Superlattice structures composed of cubic EuS nanocrystals have been reported by Hasegawa and co-workers as well (Figure 1-9)^[73]. Superlattice structures of EuS nanocrystals were prepared successfully via slow evaporation of a toluene solution containing EuS nanocrystals. When using an alcohol solution, they reported that they could successfully tune the particle aggregate size and interparticle distances of

superlattice structures by manipulating the alkyl chain length of the solvent alcohol^[74].

The optical band gap and the active wavelength of magneto-optical properties of EuS nanocrystal aggregates showed a characteristic red shift.

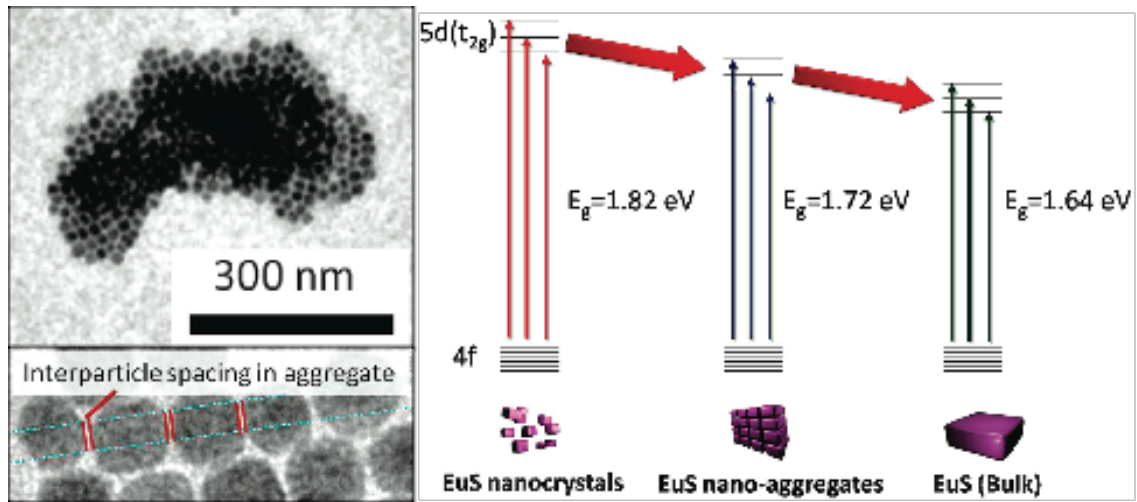


Figure 1-9. TEM images of EuS nano-aggregates and band gap energy of monomeric EuS nanocrystals of 14 nm, EuS NCs-aggregates with a cubic superlattice structure, and bulk EuS^[74].

1.7 Objectives

As mentioned above, the formation of nano-assemblies could be effective for enhancing the photophysical properties of lanthanide magnetic semiconductor nanocrystals. Although the nano-assemblies reported in previous works were composed only of EuS nanocrystals, hybrid nano-assemblies composing different nanocrystals and photo-functional molecules as building blocks are expected not only to combine the properties of the constituent building blocks but also to generate new, collective phenomena based on interparticle interactions at the nanoscale. The study and development of novel hybrid nano-assemblies composed of magnetic semiconductor nanocrystals, metal nanocrystals, and linker molecules as building blocks are expected to open up a new field of photophysics and photonic science (Figure 1-10).

In this thesis, the author investigated the synthesis and surface-functionalization of magneto-optical lanthanide nanocrystals were investigated. In particular, (1) the formation of lanthanide magnetic semiconductor nano-assemblies with photo-functional linker molecules, (2) the formation of hybrid nano-systems composed of magnetic semiconductor and metal nanocrystals, and (3) the synthesis and characterization of novel terbium nanocrystals with magneto-optical properties are demonstrated.

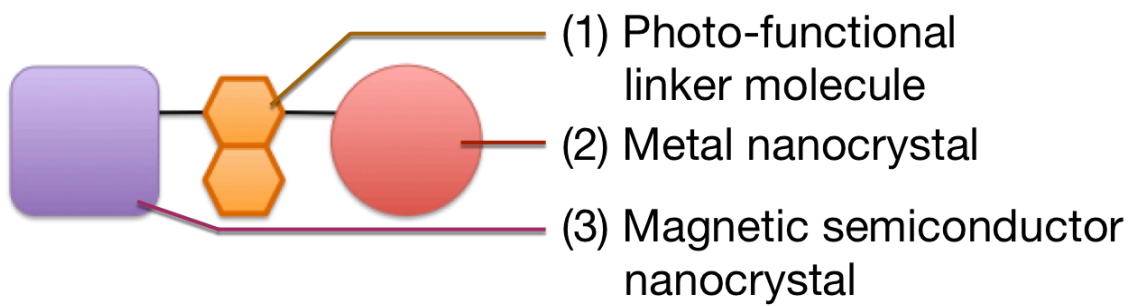


Figure 1-10. A schematic illustration of formation of novel hybrid nano-assemblies composed of (1) linker molecules, (2) metal nanocrystals, and (3) magnetic semiconductor nanocrystals as building blocks.

1.8 Contents of this thesis

This thesis consists of six chapters. Chapter 1 presents a review of existing literature on the topic and describes the significance and objectives of this study. In Chapter 2, the author proposes the use of EuS nano-assemblies with photo-functional naphthalenedithiol as linker molecules to control the aggregate size of EuS nano-assemblies. In addition, the characteristic photophysical properties of EuS nano-assemblies with naphthalene obtained using the emission spectra and emission quantum yields are demonstrated. In Chapter 3, EuS nanocrystals linked directly with gold nanocrystals (EuS-Au nanosystems) based on the molecular synthetic technology are described. Au nanocrystals are well known to show localized surface plasmon resonance (LSPR) leading to unique and unusual photophysical enhancement. The enhanced magneto-optical properties of a EuS-Au nanosystem dependent on the interparticle distance between EuS and Au and Au nanoparticle size are demonstrated for the first time. Chapter 4 presents the photo-switching magneto-optical properties of EuS-Au nanosystems based on the results in Chapter 3. The observed drastic change in the absorption band and magneto-optical properties might be related to enhanced LSPR and specific interaction between EuS and Au in the nanosystem under irradiation. In Chapter 5, novel nano-materials composed of Tb lattice structures, namely, TbX nanocrystals (terbium oxides (TbO_n ; $1.5 \leq n \leq 2$), terbium fluorides (TbF_3) and terbium oxyfluorides (TbOF)), are reported. The TbO_n , TbF_3 and TbOF nanocrystals were synthesized by the thermal decomposition of the following single-source precursors:

Tb(III) complex [Tb(acac)₃(CH₃OH)₂], [Tb(acac)₃(tppo)₂], [Tb(hfa)₃(CH₃OH)₂], and [Tb(hfa)₃(tppo)₂]. The prepared TbOF and TbF₃ nanocrystals showed effective Faraday rotations under a magnetic field. Finally, all the results and achievements of this study are summarized in Chapter 7.

1.9 References

- 1 L. R. Morss, *Chemical Reviews* **1976**, 76, 827-841.
- 2 T. Siegrist, H. W. Zandbergen, R. J. Cava, J. J. Krajewski, and W. F. Peck, *Nature* **1994**, 367, 254-256.
- 3 M. Bau, *Contributions to Mineralogy and Petrology* **1996**, 123, 323-333.
- 4 S. Hong and T. J. Marks, *Accounts of Chemical Research* **2004**, 37, 673-686.
- 5 Y. Hasegawa, Y. Wada, and S. Yanagida, *Journal of Photochemistry and Photobiology C: Photochemistry Reviews* **2004**, 5, 183-202.
- 6 J.-C. G. Bünzli, *Accounts of Chemical Research* **2006**, 39, 53-61.
- 7 F. Wang, Y. Han, C. S. Lim, Y. Lu, J. Wang, J. Xu, H. Chen, C. Zhang, M. Hong, and X. Liu, *Nature* **2010**, 463, 1061-1065.
- 8 J. D. Rinehart and J. R. Long, *Chemical Science* **2011**, 2, 2078-2085.
- 9 J. Della Rocca, D. Liu, and W. Lin, *Accounts of Chemical Research* **2011**, 44, 957-968.
- 10 K. Miyata, Y. Konno, T. Nakanishi, A. Kobayashi, M. Kato, K. Fushimi, and Y. Hasegawa, *Angewandte Chemie International Edition* **2013**, 52, 6413-6416.
- 11 K. Miyata. in *Highly Luminescent Lanthanide Complexes with Specific Coordination Structures* 10.1007/978-4-431-54944-4_1 *Springer Theses* Ch. 1, 1-13 (Springer Japan, 2014).
- 12 J. C. Suits, B. E. Argyle, and M. J. Freiser, *Journal of Applied Physics* **1966**, 37, 1391-1397.

- 13 P. Wachter, *CRC Critical Reviews in Solid State Sciences* **1972**, 3, 189-241.
- 14 P. Wachter. in *Handbook on the Physics and Chemistry of Rare Earths* Vol. 2 (eds Karl A. Gschneidner, Jr. and Eyring LeRoy) 507-574 (Elsevier, 1979).
- 15 D. Görlitz and J. Kötzler, *European Physical Journal B - Condensed Matter and Complex Systems* **1998**, 5, 37-43.
- 16 T. Kasuya, *Journal of Magnetism and Magnetic Materials* **1999**, 195, 141-147.
- 17 U. K. Sakalle, P. K. Jha, and S. P. Sanyal, *Bulletin of Materials Science* **2000**, 23, 233-235.
- 18 J. Kunes, W. Ku, and W. E. Pickett, *Journal of the Physical Society of Japan* **2005**, 74, 1408-1411.
- 19 J. A. Gaj, J. Ginter, and R. R. Gałazka, *Physica Status Solidi B* **1978**, 89, 655-662.
- 20 Y. Wang, N. Herron, K. Moller, and T. Bein, *Solid State Communications* **1991**, 77, 33-38.
- 21 H. Ohno, A. Shen, F. Matsukura, A. Oiwa, A. Endo, S. Katsumoto, and Y. Iye, *Applied Physics Letters* **1996**, 69, 363-365.
- 22 J. M. Kikkawa and D. D. Awschalom, *Nature* **1999**, 397, 139-141.
- 23 Y. Ohno, D. K. Young, B. Beschoten, F. Matsukura, H. Ohno, and D. D. Awschalom, *Nature* **1999**, 402, 790-792.
- 24 K. Ando, H. Saito, Z. Jin, T. Fukumura, M. Kawasaki, Y. Matsumoto, and H. Koinuma, *Journal of Applied Physics* **2001**, 89, 7284-7286.
- 25 Y.-w. Jun, Y.-y. Jung, and J. Cheon, *Journal of the American Chemical Society*

- 2002**, *124*, 615-619.
- 26 H. Kato, T. Matsushita, A. Takayama, M. Egawa, K. Nishimura, and M. Inoue, *Journal of Applied Physics* **2003**, *93*, 3906-3911.
- 27 N. S. Norberg, K. R. Kittilstved, J. E. Amonette, R. K. Kukkadapu, D. A. Schwartz, and D. R. Gamelin, *Journal of the American Chemical Society* **2004**, *126*, 9387-9398.
- 28 W. Li, K. Zou, M. Lu, B. Peng, and W. Zhao, *International Journal of Applied Ceramic Technology* **2010**, *7*, 369-374.
- 29 M. S. Kang, ButschA, and P. S. J. Russell, *Nat Photon* **2011**, *5*, 549-553.
- 30 S. L. Cumberland, K. M. Hanif, A. Javier, G. A. Khitrov, and G. F. Strouse, *Chemistry of Materials* **2002**, *14*, 1576-1584.
- 31 Z. L. Wang and X. Feng, *The Journal of Physical Chemistry B* **2003**, *107*, 13563-13566.
- 32 J. Wang, *Analyst* **2005**, *130*, 421-426.
- 33 T. Jamieson, R. Bakhshi, D. Petrova, R. Pocock, M. Imani, and A. M. Seifalian, *Biomaterials* **2007**, *28*, 4717-4732.
- 34 S. Guo and E. Wang, *Analytica Chimica Acta* **2007**, *598*, 181-192.
- 35 J. M. Pingarrón, P. Yáñez-Sedeño, and A. González-Cortés, *Electrochimica Acta* **2008**, *53*, 5848-5866.
- 36 C. N. R. Rao, A. K. Sood, K. S. Subrahmanyam, and A. Govindaraj, *Angewandte Chemie International Edition* **2009**, *48*, 7752-7777.
- 37 Z. L. Wang, *Materials Science and Engineering: R: Reports* **2009**, *64*, 33-71.

- 38 D. Golberg, Y. Bando, Y. Huang, T. Terao, M. Mitome, C. Tang, and C. Zhi, *ACS Nano* **2010**, *4*, 2979-2993.
- 39 L. Mai, L. Xu, C. Han, X. Xu, Y. Luo, S. Zhao, and Y. Zhao, *Nano Letters* **2010**, *10*, 4750-4755.
- 40 X. Zhao, B. M. Sanchez, P. J. Dobson, and P. S. Grant, *Nanoscale* **2011**, *3*, 839-855.
- 41 A. P. Alivisatos, *Endeavour* **1997**, *21*, 56-60.
- 42 G. C. Papaefthymiou, *Nano Today* **2009**, *4*, 438-447.
- 43 H. Akinaga, S. Miyanishi, K. Tanaka, W. Van Roy, and K. Onodera, *Applied Physics Letters* **2000**, *76*, 97-99.
- 44 M. Inoue, R. Fujikawa, A. Baryshev, A. Khanikaev, P. B. Lim, H. Uchida, O. Aktsipetrov, A. Fedyanin, T. Murzina, and A. Granovsky, *Journal of Physics D: Applied Physics* **2006**, *39*, R151.
- 45 S. Thongchant, Y. Hasegawa, Y. Wada, and S. Yanagida, *Chemistry Letters* **2001**, *30*, 1274-1275.
- 46 Y. Hasegawa, S. Thongchant, Y. Wada, H. Tanaka, T. Kawai, T. Sakata, H. Mori, and S. Yanagida, *Angewandte Chemie International Edition* **2002**, *41*, 2073-2075.
- 47 S. Thongchant, Y. Hasegawa, Y. Wada, and S. Yanagida, *Journal of Physical Chemistry B* **2003**, *107*, 2193-2196.
- 48 S. Thongchant, *Chemistry Letters* **2003**, *32*, 706-707.
- 49 Y. Hasegawa, M. Afzaal, P. O'Brien, Y. Wada, and S. Yanagida, *Chemical*

- Communications* **2005**, 242-243.
- 50 Y. Hasegawa, Y. Wada, and S. Yanagida, *Journal of Alloys and Compounds* **2006**, 408–412, 207-211.
- 51 Y. Hasegawa, Y. Okada, T. Kataoka, T. Sakata, H. Mori, and Y. Wada, *Journal of Physical Chemistry B* **2006**, 110, 9008-9011.
- 52 Y. Hasegawa, T. Adachi, A. Tanaka, M. Afzaal, P. O'Brien, T. Doi, Y. Hinatsu, K. Fujita, K. Tanaka, and T. Kawai, *Journal of the American Chemical Society* **2008**, 130, 5710-5715.
- 53 M. D. Regulacio, K. Bussmann, B. Lewis, and S. L. Stoll, *Journal of the American Chemical Society* **2006**, 128, 11173-11179.
- 54 A. S. Pereira, P. Rauwel, M. S. Reis, N. J. Oliveira Silva, A. Barros-Timmons, and T. Trindade, *Journal of Materials Chemistry* **2008**, 18, 4572-4578.
- 55 M. D. Regulacio, S. Kar, E. Zuniga, G. Wang, N. R. Dollahon, G. T. Yee, and S. L. Stoll, *Chemistry of Materials* **2008**, 20, 3368-3376.
- 56 S. Kar, W. L. Boncher, D. Olszewski, N. Dollahon, R. Ash, and S. L. Stoll, *Journal of the American Chemical Society* **2010**, 132, 13960-13962.
- 57 R. S. Selinsky, J. H. Han, E. A. Morales Pérez, I. A. Guzei, and S. Jin, *Journal of the American Chemical Society* **2010**, 132, 15997-16005.
- 58 M. A. Harrison, S. Somarajan, S. V. Mahajan, D. S. Koktysh, K. van Benthem, and J. H. Dickerson, *Materials Letters* **2011**, 65, 420-423.
- 59 W. He and J. H. Dickerson, *Applied Physics Letters* **2011**, 98, 081914.
- 60 T. Mirkovic, D. Rossouw, G. A. Botton, and G. D. Scholes, *Chemistry of*

- Materials* **2011**, *23*, 181-187.
- 61 J. G. Kelly, W. He, S. Somarajan, K. G. Yager, and J. H. Dickerson, *Materials Letters* **2012**, *89*, 198-201.
- 62 Y. Hasegawa, M. Kumagai, A. Kawashima, T. Nakanishi, K. Fujita, K. Tanaka, and K. Fushimi, *Journal of Physical Chemistry C* **2012**, *116*, 19590-19596.
- 63 Y. Hasegawa, *Chemistry Letters* **2013**, *42*, 2-7.
- 64 Y. Hasegawa, M. Maeda, T. Nakanishi, Y. Doi, Y. Hinatsu, K. Fujita, K. Tanaka, H. Koizumi, and K. Fushimi, *Journal of the American Chemical Society* **2013**, *135*, 2659-2666.
- 65 T. Nakanishi, M. Maeda, A. Kawashima, S. Kamiya, K. Fushimi, K. Fujita, K. Tanaka, and Y. Hasegawa, *Journal of Alloys and Compounds* **2013**, *562*, 123-127.
- 66 W. L. Boncher, N. Rosa, S. Kar, and S. L. Stoll, *Chemistry of Materials* **2014**, *26*, 3144-3150.
- 67 C. E. Johnson, L. Costa, J. A. Johnson, D. E. Brown, S. Somarajan, W. He, and J. H. Dickerson, *Journal of Physics D: Applied Physics* **2014**, *47*, 075001.
- 68 S. A. Maier, P. G. Kik, H. A. Atwater, S. Meltzer, E. Harel, B. E. Koel, and A. A. G. Requicha, *Nature Materials* **2003**, *2*, 229-232.
- 69 H. Tu, S. Yang, V. Chikan, and D. F. Kelley, *The Journal of Physical Chemistry B* **2004**, *108*, 4701-4710.
- 70 F. Dumestre, B. Chaudret, C. Amiens, P. Renaud, and P. Fejes, *Science* **2004**, *303*, 821-823.

- 71 R. Koole, P. Liljeroth, C. de Mello Donegá, D. Vanmaekelbergh, and A. Meijerink, *Journal of the American Chemical Society* **2006**, *128*, 10436-10441.
- 72 E. V. Shevchenko, M. Ringler, A. Schwemer, D. V. Talapin, T. A. Klar, A. L. Rogach, J. Feldmann, and A. P. Alivisatos, *Journal of the American Chemical Society* **2008**, *130*, 3274-3275.
- 73 A. Tanaka, H. Kamikubo, Y. Doi, Y. Hinatsu, M. Kataoka, T. Kawai, and Y. Hasegawa, *Chemistry of Materials* **2010**, *22*, 1776-1781.
- 74 A. Tanaka, H. Kamikubo, M. Kataoka, Y. Hasegawa, and T. Kawai, *Langmuir* **2010**, *27*, 104-108.

Chapter 2

EuS Nano-assemblies Linked with Photo-functional Naphthalenedithiols

2.1 Introduction

Semiconductor nanocrystals have attracted considerable attention in the field of advanced materials science because of their remarkable optical, electric, and magnetic properties^[1-7]. In particular, the potential applications of magnetic semiconductor nanocrystals with magnetic and optical properties include use as optical isolators and magneto-optical memories in photo-magnetic devices^[8-10]. Europium chalcogenides, EuX (X = O, S, Se, and Te), comprise one of the most important series of intrinsic magnetic semiconductors^[11-13]. EuX is a magnetic semiconductor characterized by degenerate $4f$ orbitals of Eu(II) ions existing between the conduction band ($5d$ orbitals of Eu(II)) and the valence band (p orbitals of O²⁻, S²⁻, Se²⁻, or Te²⁻).

The $4f-5d$ electronic transition and spin configuration result in the generation of a large magneto-optical effect, which makes EuX promising candidates as active materials in future optical isolators^[14-18]. Among them, EuS nanocrystals have been focused on as promising materials because of their ferromagnetic properties and characteristic Faraday effects in the visible region^[15,16].

As described in Chapter 1, various types of nano-assemblies composed of colloidal nanocrystals (such as semiconductor, metal or magnetic nanocrystals) have been studied extensively for potential applications in fields such as photovoltaic, biological labels, and three-dimensional waveguides^[19-21]. They show unique and remarkable coupled properties, optical, electric, and magnetic properties, as well as originally properties of only nanocrystals^[20-22]. In particular, magnetic semiconductor nanocrystals are expected to be active materials having various potential applications including use in photo-magnetic devices as optical isolators and magneto-optical memory because of their magnetic and optical properties. The EuS nanocrystal is one such material. Hasegawa and co-workers have also reported size-controlled EuS nano-assemblies^[23,24]. They successfully prepared EuS nano-assemblies with tunable aggregation sizes and interparticle distances depending on the solvent alcohol used. The active wavelength of magneto-optical properties of EuS nano-assemblies showed a characteristic red shift in the aggregated structures. Such a shift is caused by exciton coupling and specific magneto-interactions between EuS nanocrystals. To analyze the optical and magnetic interactions in EuS nano-assemblies, specific functional molecules linked with EuS nanocrystals are required.

In this chapter, the author focuses on photo-functional naphthalenedithiol (NpDDT) as a linker for the formation of EuS nano-assemblies (Figure 2-1). Naphthalene molecules show photo-luminescence with high emission yield in terms of quantity, which is dependent on surrounding environment, that is, dielectric constant of the matrix. The dithiol unit has also been used as an ideal linker part for creating chemical connections between semiconductor nanocrystals and organic molecules. The NpDDT molecule is expected to be a sensing linker unit in the analysis of EuS nano-assemblies. NpDDT is synthesized by a reaction in which hydroxyl groups of 1,4-dihydroxynaphthalene are replaced by dithiol groups^[25]. Self-assembled structures of the EuS nano-assemblies with NpDDT were characterized with powder X-ray diffractometer (XRD) and transmission electron microscope (TEM). Photophysical properties of EuS nano-assemblies with naphthalene were characterized using the emission spectra and the emission quantum yields. Here, synthesis and photophysical properties of EuS nano-assemblies with photo-functional NpDDT have been investigated.

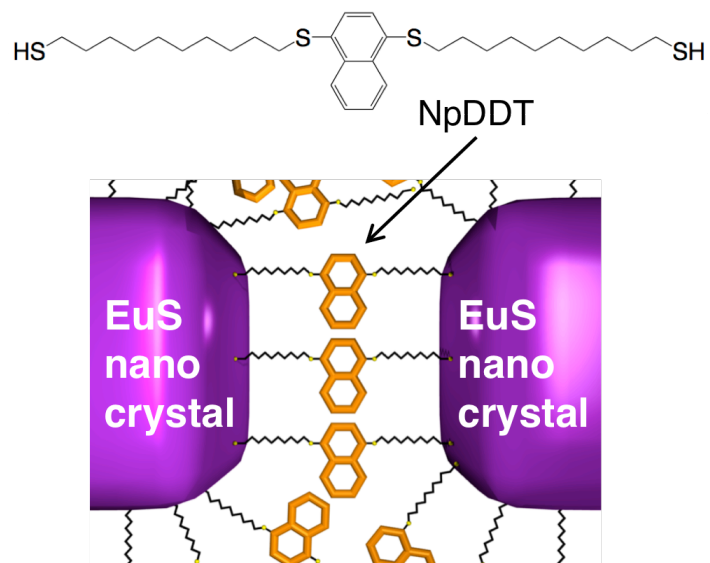


Figure 2-1. Illustration of the EuS nano-assemblies linked with photo-functional linker, NpDDT.

2.2 Experiments

2.2.1 Materials

Europium(III) chloride hexahydrate ($\text{EuCl}_3 \cdot 6\text{H}_2\text{O}$) and sodium *N,N*-diethyldithiocarbamate trihydrate ($\text{Na}(\text{S}_2\text{CNET}_2) \cdot 3\text{H}_2\text{O}$) were purchased from Kanto Chemical Co. Inc. Tetraphenylphosphonium bromide (BrPPH_4) was purchased from Wako Pure Chemical Industry, Ltd. Oleylamine (OLA) and 1,10-decanedithiol (DDT), 1,4-naphthalenediol and *p*-toluenesulfonic acid was obtained from Tokyo Chemical Industry Co., Ltd. *p*-Toluenesulfonic acid was purified by recrystallization from ethyl acetate and dried under vacuum before use. All other chemicals and solvents were reagent grade and were used without further purification.

2.2.2 Apparatus

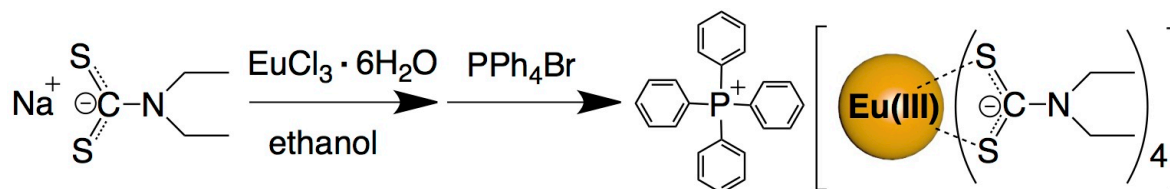
Fourier-transform infrared spectroscopy (FT-IR) measurements were performed at room temperature using a Perkin-Elmer system 2000 FT-IR spectrometer. Hydrogen nuclear magnetic resonance (^1H NMR) spectra were measured using JEOL AL-300 (300 MHz). ^1H NMR chemical shifts were determined by using tetramethylsilane (TMS) as an internal standard. Elemental analyses were performed on a J-Science Lab JM 10 Micro Corder and an Exeter Analytical CE440. XRD patterns were characterized by Bruker AXS using Cu K α radiation source ($\lambda = 0.15418$ nm) and identified using the International Centre for Diffraction Data (ICDD). Ultraviolet-visible (UV-vis) absorption spectra were measured using a JASCO V-570

spectrophotometer at room temperature. Emission spectra were measured using a JASCO F-6300-H spectrometer and corrected for the response of the detector system. The emission quantum yields excited at 330 nm were calculated using a JASCO F-6300-H spectrofluorometer attached with a JASCO ILF-533 integrating sphere unit ($\varphi = 100$ mm). The wavelength dependences of the detector response and the beam intensity of Xe light source for each spectrum were calibrated using a standard light source. EuS nano-assemblies were identified using a TEM (JEOL JEM-2010 FASTEM 200 kV) with an energy dispersive X-ray spectroscopy (EDS) detector. The chemical compositions of EuS nano-assemblies were determined by inductively coupled plasma optical emission spectroscopy (ICP-OES, Shimadzu ICPE-9000) and the EDS analysis.

2.2.3 Syntheses

Synthesis of Tetraphenylphosphonium Tetrakis(diethyldithiocarbamate)

Europium(III) ((PPh₄)[Eu(S₂CEt₂)₄]):



Scheme 2-1. Reaction scheme of (PPh₄)[Eu(S₂CEt₂)₄].

A solution of Na(S₂CNEt₂)·3H₂O (14 g) in 30 mL of methanol was added to EuCl₃·6H₂O (5.6 g) dissolved in 30 mL of methanol while stirring and reacted for 3 h. After the reaction mixture was filtered, a solution of BrPPh₄ (6.4 g) in 30 mL of methanol was added to the filtrated solution and stirred for 9 h. The resulting precipitate was separated by filtration and washed 2 times with ethanol. Yield: 30%. ¹H NMR (300 MHz, CDCl₃, 25°C, TMS): δ = 7.91–7.70 (m, 20H; Ar-H), 3.17 (m, 16H; CH₂), 1.61 ppm (t, ³J (H,H) = 7 Hz, 24H; CH₃); IR (KBr): $\tilde{\nu}$ = 1485–1482 cm⁻¹ (C–N), 1442 cm⁻¹ (P–Phenyl), 1007 cm⁻¹ (C–S); elemental analysis calcd (%) for C₄₄H₆₀EuN₄PS₈: C 48.73, H 5.58, N 5.17, S 23.65; found: C 48.55, H 5.51, N 5.00, S 23.41.

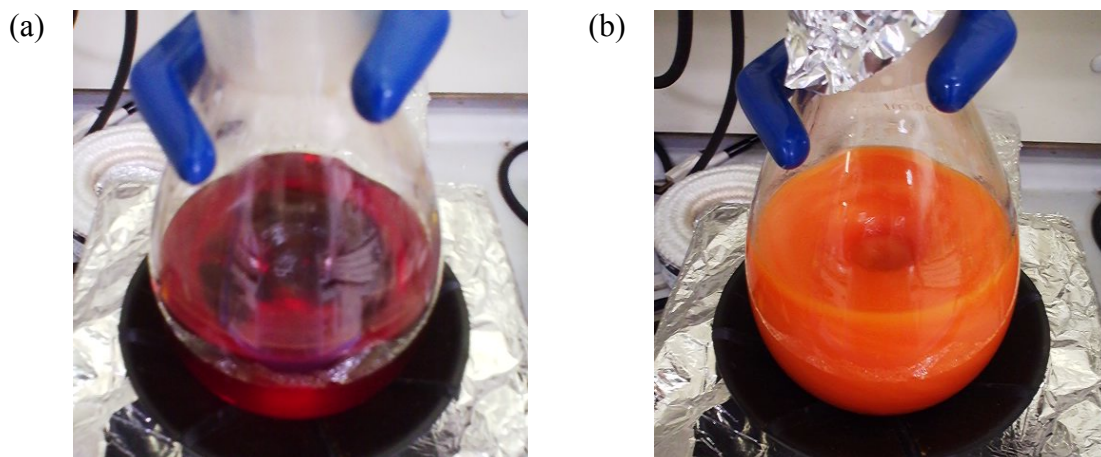
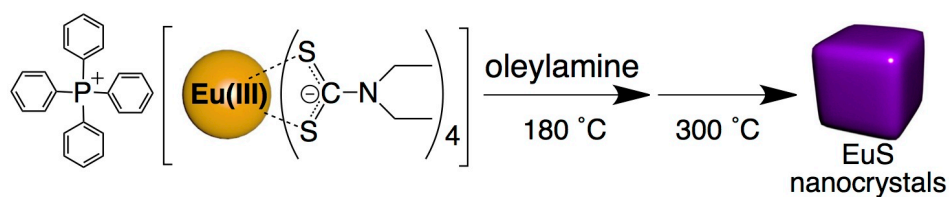


Figure 2-2. Photographs of the synthesis of $(\text{PPh}_4)[\text{Eu}(\text{S}_2\text{CEt}_2)_4]$ (a) before and (b) after reaction.

Preparation of Cube-Shaped EuS nanocrystals:



Scheme 2-2. Reaction scheme of EuS nanocrystals.

Under N_2 atmosphere, $(\text{PPh}_4)[\text{Eu}(\text{S}_2\text{CNEt}_2)_4]$ (0.5 g) was dissolved into oleylamine (4.5 g), and the mixture was heated at 180°C and stirred for 20 min. After the reaction solvent was heated to 300°C and stirred for 6 h, the purple liquid was centrifuged at 4000 rpm for 10 min. The precipitation was added to 8 mL of chloroform and centrifuged at 4000 rpm for 15 min, and the clear purple liquid of oleylamine capped EuS nanocrystals was obtained.

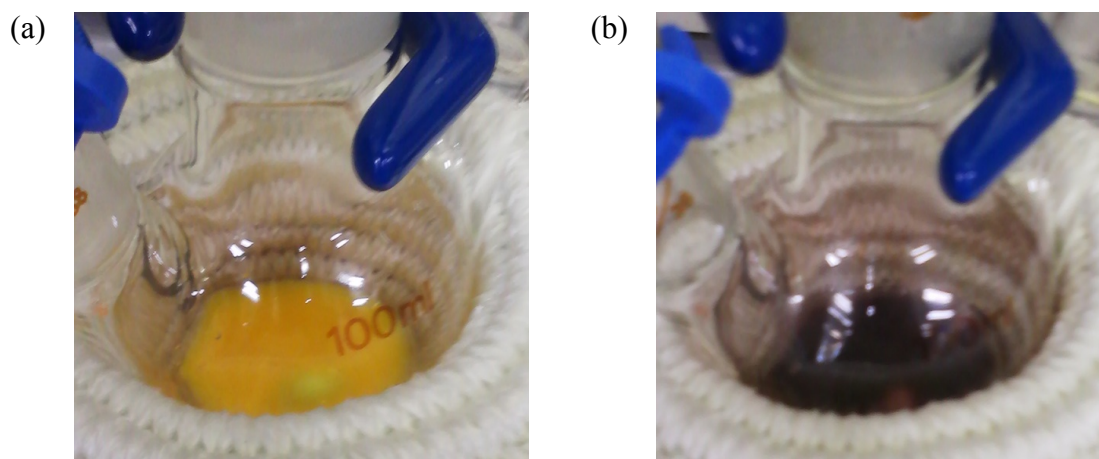
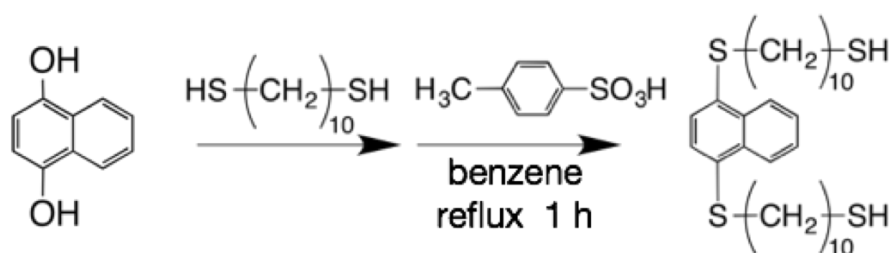


Figure 2-2. Photographs of the synthesis of EuS nanocrystals (a) before and (b) after reaction.

Synthesis of 1,4-bisdecanethionaphthalene (NpDDT):

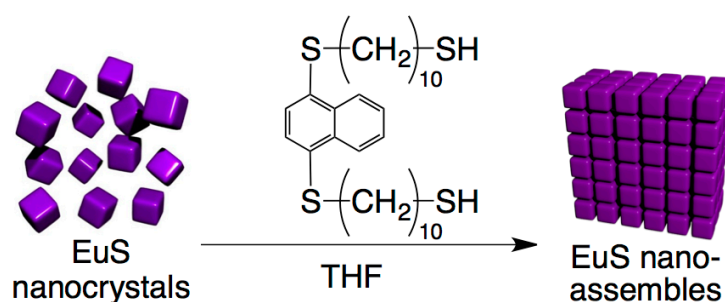


Scheme 2-3. Reaction scheme of NpDDT.

1,4-bisdecanethionaphthalene (NpDDT) was prepared by the similar method as previously reported^[25]. Under N₂ atmosphere, 1,4-dihydroxynaphthalene (0.81 g, 5.0 mmol), *p*-toluenesulfonic acid (0.48 g, 2.5 mmol) and 1,10-decanedithiol (10 mL, 46 mmol) were dissolved into benzene (50 mL), and the mixture was refluxed at 80°C for 1 h. After aqueous workup, the product was purified by column chromatography on silica gel using ethyl acetate as an eluent. The collected product was crystallized from a mixture of ethyl acetate and hexane to give NpDDT as a white solid. ¹H NMR (300 MHz, CDCl₃, 25°C, TMS): δ = 1.2-1.4 (m, 26H), 1.5-1.7 (m, 8H), 2.5-2.6 (m, 4H),

2.9-3.0 (m, 4H), 7.5 (s, 2H), 7.5-7.6 (m, 2H), 8.4-8.5 (m, 2H); IR (KBr): $\tilde{\nu} = 2924, 2849$ cm^{-1} (C-H), 2567 cm^{-1} (S-H), 1564 cm^{-1} (C=C of Ar), 1466 cm^{-1} (C-H); elemental analysis calcd (%) for $\text{C}_{30}\text{H}_{48}\text{S}_4$: C, 67.10; H, 9.01; N, 0; S, 23.89; found: C, 66.87, H, 9.06, N, 0.00, S, 24.00.

Preparation of EuS nano-assemblies:



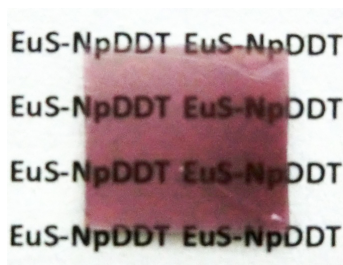
Scheme 2-4. Reaction scheme of EuS nano-assemblies.

EuS nano-assemblies were formed by adding NpDDT (0.14 g, 0.25 mmol) dissolved in 10 mL of THF to a solution of 30 mg of oleylamine capped EuS nanocrystals dissolved in 120 mL of THF. After the reaction solvent was stirred at room temperature for 20 min (EuS-NpDDT-20min) and 3 h (EuS-NpDDT-3h), the resulting solution was centrifuged at 4000 rpm for 10 min. The precipitation was added to 20 mL of chloroform and EuS nano-assemblies were obtained.

2.2.4 Preparation of Polymer Thin Films

The obtained EuS nano-assemblies (20 mg) were added to a chloroform solution (1 mL) of polymethylmethacrylate (PMMA) (2.0 g) and dispersed well under ultrasonic treatment, giving the colloidal suspension. The PMMA thin films were prepared on a glass substrate from the colloidal suspension using drop-casted method for measurements of photophysical properties. The thickness of the PMMA thin films containing EuS nano-assemblies were measured by a surface profiler KLA Tencor ALPHA STEP 500.

The Faraday effect measurements were performed using a measurement system for Faraday and Kerr effects (JASCO, Model K-250). A Xe lamp was used as the light source. The external magnetic field was 15000 Oe.



Scheme 2-2. A photograph of the PMMA thin films containing EuS nano-assemblies.

2.3 Results and Discussion

2.3.1 Synthesis of EuS Nanocrystals

Cubic EuS nanocrystals with oleylamine were prepared by thermal reduction of the single source precursor, $(\text{PPh}_4)[\text{Eu}(\text{S}_2\text{CNEt}_2)_4]$, in oleylamine under N_2 atmosphere at 300°C for 6 h. The formation of crystalline EuS nanocrystals was confirmed with XRD (Figure 2-3). Diffraction peaks 2θ of the XRD patterns at 25.5, 29.8, 42.6, 50.6, 53.1, 62.1, and 70.5 degree were assigned as (111), (200), (220), (222), (400), (420), and (422), respectively, of NaCl-type EuS (ICDD 26-1419, $Fm\bar{3}m$). The crystal grain size of the EuS nanocrystals was calculated from the XRD pattern using the Scherer equation (equation (2-1)).

$$D = \frac{K\lambda}{\beta_{1/2} \cos \theta} \quad (2-1)$$

where D , K , λ , $\beta_{1/2}$, and θ denote crystal grain size, shape factor (0.9), X-ray wavelength (0.154056 nm), line broadening at half the maximum intensity, and Bragg angle, respectively. The crystal grain size was found to be 18 nm.

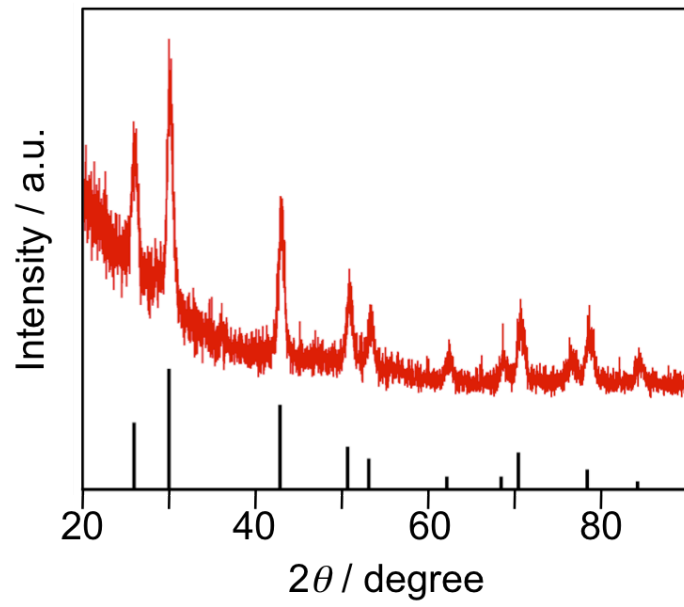


Figure 2-3. XRD pattern of EuS nanocrystals and ICDD data (EuS, 26-1419, *Fm3m*).

A typical TEM image, electron diffraction pattern, and a size distribution histogram of EuS nanocrystals are shown in Figure 2-4. Cubic images were observed and their electron diffraction pattern was found agree well with the isometric EuS lattice. The crystal size determined from TEM observations was found to be approximately 18.5 nm and similar to the size measured by XRD (18 nm).

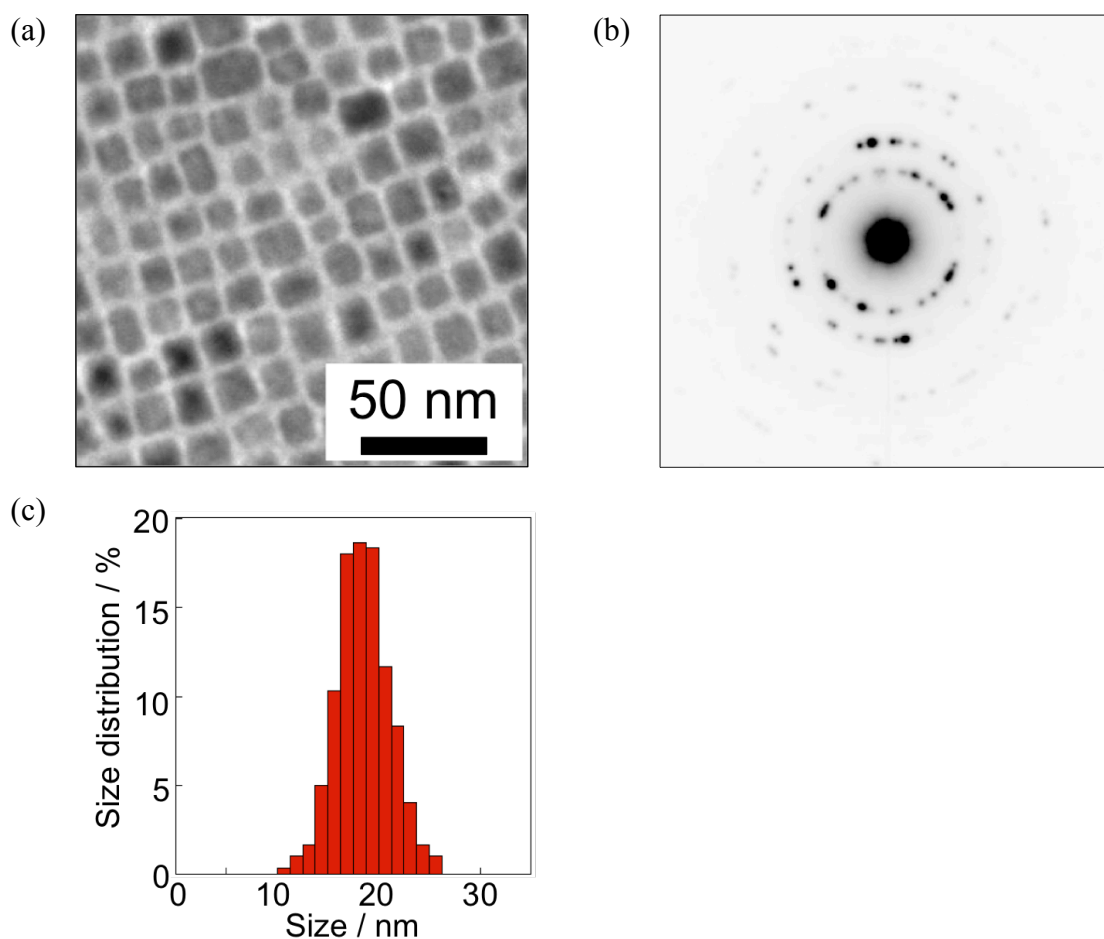


Figure 2-4. (a) TEM image, (b) the electron diffraction pattern, and (c) size distribution histogram of cubic shaped EuS nanocrystals.

2.3.2 Formation of EuS Nano-assemblies

Naphthalenedithiol, NpDDT, is a promising photo-functional linker with a luminescent naphthalene unit and two dithiol units as a connecting part to EuS nanocrystals. NpDDT was synthesized by the reaction of 1,4-dihydroxynaphthalene with 1,10-decanedithiol in benzene at 80°C for 1 h.

Prepared NpDDT linkers were added into THF solution of EuS nanocrystals at room temperature for 20 min (EuS-NpDDT-20min) and 3 h (EuS-NpDDT-3h). Each THF solution containing EuS-NpDDT-20min or EuS-NpDDT-3h were separated by centrifugation and re-dispersed into chloroform. The TEM images of EuS-NpDDT-20min and EuS-NpDDT-3h are shown in Figures 2-5, respectively. The aggregation size of EuS-NpDDT-3h was estimated to be greater than 1000 nm. The author observed that the average aggregation size of EuS-NpDDT-3h was much larger than that of EuS-NpDDT-20min. Aggregation growth of EuS nano-assemblies was found to be dependent on the replacement reaction time of NpDDT from oleylamine on the EuS nanocrystals' surfaces.

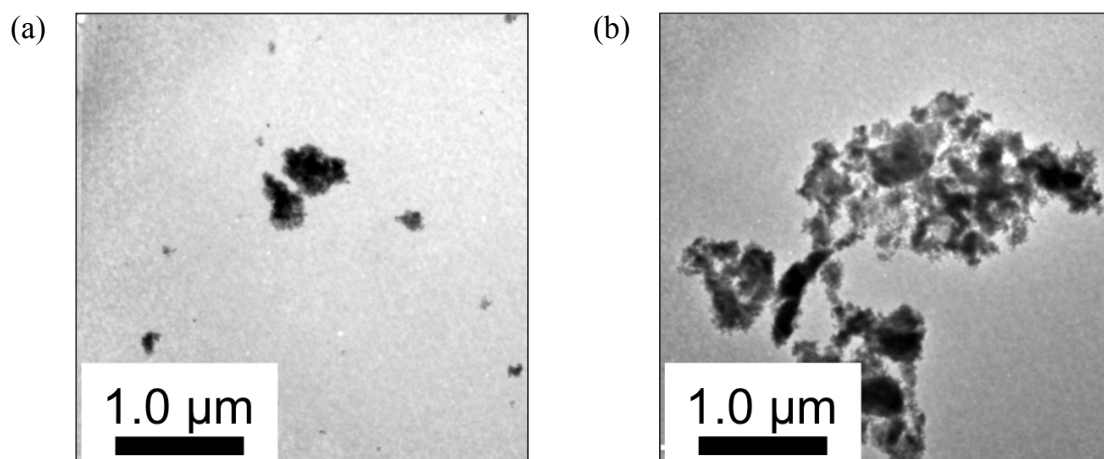


Figure 2-5. TEM images of (a) EuS-NpDDT-20min and (b) EuS-NpDDT-3h.

To confirm the chemical bonding of EuS-NpDDT nano-assemblies, UV-vis absorption spectra of PMMA thin films containing EuS nanocrystals, EuS-NpDDT-20min and EuS-NpDDT-3h, were measured (Figure 2-6 and Table 2-1). All of them showed the broad absorption bands assigned to the electronic transition between $4f^7$ and $4f^6(7F_J)5d(t_{2g})$ ^[11,12,24].

The active wavelength of the UV-vis spectra of EuS-NpDDT nano-assemblies were red-shifted depending on the replacement time of oleylamine with NpDDT. Specific red shift of the absorption spectra of EuS-NpDDT nano-assemblies might have been caused by the binding energy of EuS-NpDDT and exciton coupling between EuS nanocrystals. The binding energy of Eu-NpDDT might be higher than that of Eu-oleylamine. Additionally, the characteristic red shift of the active wavelength depending on the condensed structures of semiconductor nanocrystals has been elucidated in terms of exciton coupling between nanocrystals^[24,26,27]. Thus, the energy

gap of $4f-5d$ bands in the EuS-NpDDT nano-assemblies might be smaller than that in monomeric EuS nanocrystals.

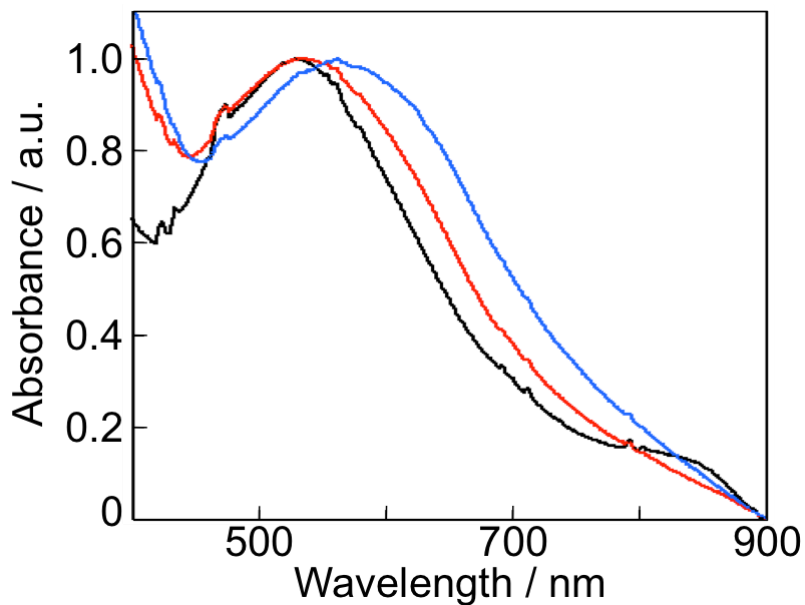


Figure 2-6. UV-vis absorption spectra of PMMA thin films containing EuS nanocrystals (black), EuS-NpDDT-20min (red) and EuS-NpDDT-3h (blue).

Table 2-1. Peak top wavelength of UV-vis absorption spectra of PMMA thin films containing EuS nano-assemblies depended on the replacement time of oleylamine with NpDDT.

Reaction time / min	Peak top wavelength / nm
0	531
10	532
20	533
60	542
180	562
300	562

The author measured the concentration ratio of Eu and S using inductively coupled plasma optical emission spectroscopy (ICP-OES). For EuS-NpDDT-3h, the Eu/S ratio was found to be 1/2.2, although the Eu/S ratio for EuS nanocrystals was 1/1 according to EDS analysis. Since NpDDT has two sulfur atoms in one molecule, EuS/NpDDT is estimated to be 1/0.6. The author calculated the number of atoms in cubic EuS nanocrystals (average diameter: 18 nm). The total number of Eu atoms in the EuS nanocrystals was approximately 100,000; in contrast, the number of Eu atoms on the EuS surface ($\text{Eu}_{\text{surface}}$) is 10,000. From this estimate, the author determined the excess amount of NpDDT on the surface of the EuS nanocrystals ($\text{Eu}_{\text{surface}}/\text{NpDDT} = 1/6$), even after the purification of EuS-NpDDT via centrifugation of the THF solutions. Oleylamine molecules on the EuS nanocrystals might have been replaced by large amounts of NpDDT molecules. In contrast, the peak-top wavelength of the $4f-5d$ transition band in EuS-NpDDT-20min is considerably similar to that in EuS-oleylamine. Thus, the surface of EuS-NpDDT-20min might be covered with large amounts of oleylamine.

2.3.3 Magneto-optical properties of EuS nano-assemblies

The wavelength dependence of the Faraday rotation angle was measured for the PMMA thin films containing the EuS nano-assemblies. The Faraday rotation spectrum at room temperature under an external magnetic field of 15,000 Oe had clear positive and negative peaks, which could have contributed to the $4f-5d$ transition in the EuS nanocrystals. The Verdet constant, which indicates the strength of the Faraday rotation, is calculated using the following equation (2-2).

$$V = \theta/Hl \quad (2-2)$$

where θ , H , and l denote the Faraday rotation angle, the external magnetic field and the thickness of the thin film, respectively. To estimate the Faraday rotation efficiency of the EuS nano-assemblies, the author considered that the Verdet constant should be normalized by the photon-absorption ability of the EuS nano-assemblies, which contains information on the absorption coefficient ε of EuS, concentration of EuS and optical-pass length l . The normalized Verdet constants (V_{abs}) can be re-written as follows.

$$V_{\text{abs}} = \theta/HA \quad (2-3)$$

where A is the absorbance of the PMMA thin films containing the EuS nano-assemblies.

The calculated V_{abs} values are shown in Figure 2-7 and Table 2-2.

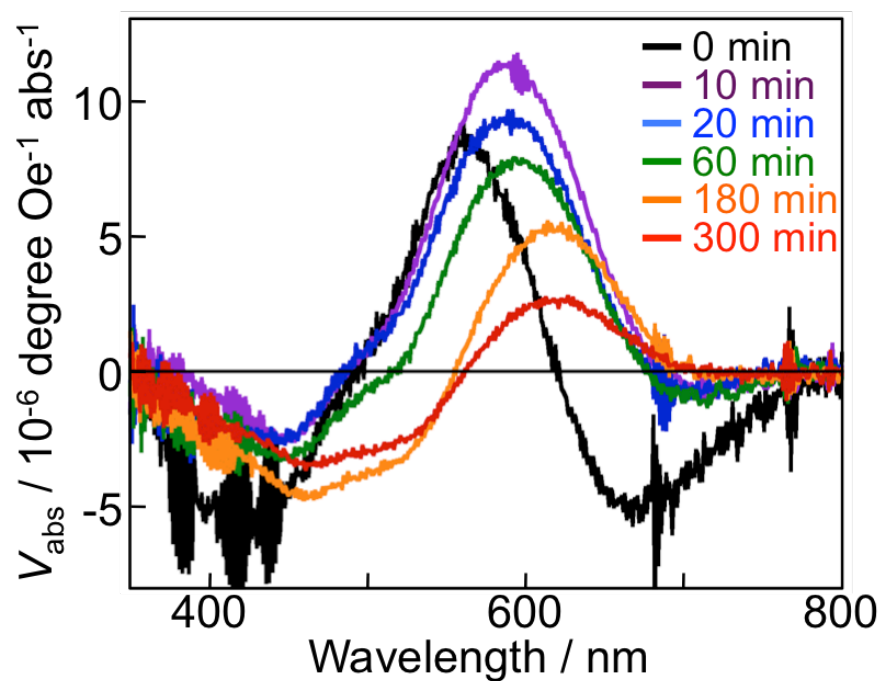


Figure 2-7. The calculated V_{abs} constants of polymer thin films containing EuS nanocrystals (black) and EuS nano-assemblies with reaction time for 10 (purple), 20 (blue), 60 (green), 180 (orange), and 300 min (red) under an external magnetic field of 15000 Oe.

Table 2-2. Magneto-optical properties of PMMA thin films containing EuS nano-assemblies depended on the replacement time of oleylamine with NpDDT.

Reaction time / min	V_{abs} Peak position	
	λ_{max} / nm	$V_{\text{abs, peak}}$ / 10^{-6} degree Oe $^{-1}$ abs $^{-1}$
0	561	10.1
10	595	12.5
20	592	9.68
60	593	7.16
180	614	6.14
300	627	3.70

The active wavelength of the EuS nano-assemblies' Faraday rotation spectra is markedly longer than that of monomeric EuS nanocrystals in PMMA, as well as that of the UV-vis spectra of the EuS-NpDDT nano-assemblies. In addition, the characteristic red shifts in the Faraday rotation spectra of EuS nano-assemblies were observed depending on the replacement time of oleylamine with NpDDT. These shifts might be related to the formation of nano-assemblies, as reported by Hasegawa and co-workers, who suggested that the red shifts in the Faraday rotation spectra are caused by exciton coupling between the EuS nanocrystals^[24]. The author considers that changing of the Faraday rotation spectra might be caused by the ligand field of Eu(II) ions on the EuS surface, as shown in Figure 2-6, and exciton coupling between the EuS nanocrystals.

In addition, the author observed that the Faraday rotation angle was, first, increased at 10 min; subsequently, it decreased with increasing replacement time. These results might also be related to the ligand change and the subsequent formation of EuS nano-assemblies. These results suggest that control over the formation of EuS nano-assemblies is important for enhancing magneto-optical properties of the EuS nano-assemblies.

2.3.4 Emission properties of EuS nano-assemblies

The emission spectra of PMMA thin films excited at 330 nm are shown in Figure 2-8. The emission spectra are normalized at the absorption bands of the π - π^* transition of naphthalene units in NpDDT linkers. The author observed the characteristic emission band at 392 nm, which is also assigned to the π - π^* transition of naphthalene units. The emission intensity of the PMMA thin films with EuS-NpDDT-3h was much lower than that of the PMMA thin films with EuS-NpDDT-20min. Additionally, the emission wavelength of NpDDT molecules excited at 330 nm in chloroform was found to be 403 nm, longer than that of NpDDT linkers in PMMA thin films with EuS nano-assemblies. The characteristic red shift of the emission spectrum of naphthalene units in PMMA films with EuS nano-assemblies might have been affected by the aggregation of NpDDT units on the EuS nanocrystal surface.

The emission quantum yields of NpDDT and PMMA thin films with EuS-NpDDT-20min and EuS-NpDDT-3h are summarized in Table 2-3. The emission quantum yield of NpDDT excited at 330 nm in chloroform was found to be 16%. The emission quantum yields of PMMA thin films with EuS-NpDDT-20min and EuS-NpDDT-3h were estimated to be 11 and 6%, respectively. The excited state of the naphthalene units in NpDDT may have been quenched by the adsorption of EuS nanocrystals because of EuS nanocrystals' broad absorption bands at around 400 nm. Moreover, the emission quantum yield of EuS-NpDDT-3h with larger aggregation size was lower than that of EuS-NpDDT-20min. The emission quantum yield of NpDDT

might be related to the size of EuS nano-assemblies.

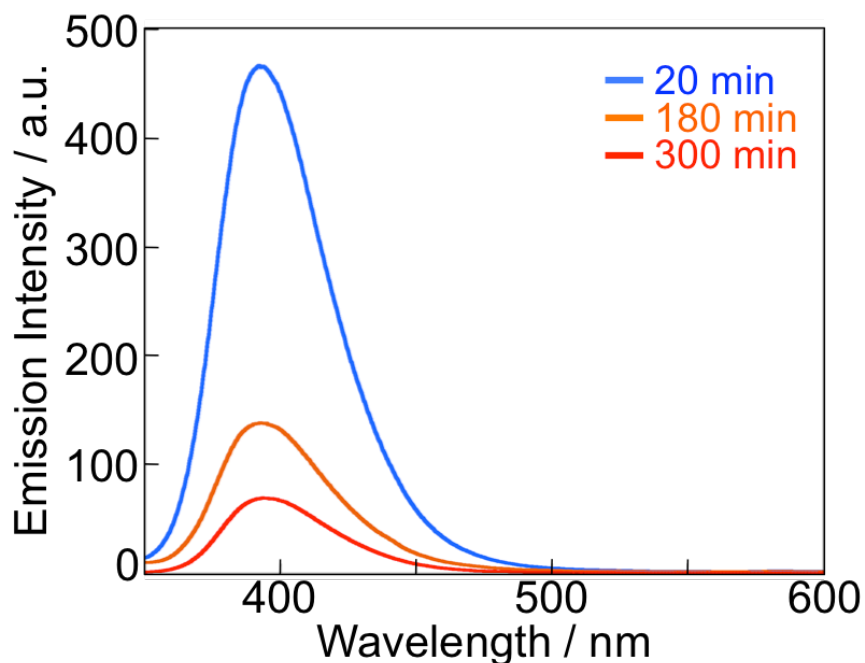


Figure 2-8. Emission spectra of PMMA thin films containing EuS-NpDDT-20min (blue), EuS-NpDDT-3h (orange), and EuS-NpDDT-5h (red). The emission spectra were measured by excitation at 330 nm at room temperature.

Table 2-3. Photophysical properties of NpDDT in chloroform and PMMA thin films with EuS nanocrystals, EuS-NpDDT-20min and EuS-NpDDT-3h.

sample	matrix	emission wavelength / nm	emission quantum yield / %
NpDDT	chloroform	403	16
EuS-NpDDT-20min	PMMA	392	11
EuS-NpDDT-3h	PMMA	392	6

The emission quantum yields were measured by excitation at 330 nm at room temperature. PMMA film thickness using surface profiler was found to be 10 nm.

2.4 Conclusions

The author has successfully observed the aggregation growth of EuS nanocrystals using luminescent NpDDT linkers. The novel luminescent NpDDT linker is an effective material for the formation and observation of EuS nano-assemblies.

The formation of EuS nano-assemblies using NpDDT linkers was confirmed with TEM observations and UV-vis absorption measurements. The author observed that the peak position and angle of Faraday rotation were dependent on the ligand replacement time of oleylamine to NpDDT on the surface of EuS nanocrystals and the subsequent formation of EuS nano-assemblies. These results mean that the control over the formation process is important for amplifying the magneto-optical properties of EuS nano-assemblies. The emission quantum yields of naphthalene units in NpDDT were found to be dependent on the aggregation size of EuS nano-assemblies.

The quenching mechanism in the emission process of naphthalene molecules on semiconductor nano-assemblies has not been reported thus far. Based on this work, the author can observe and control the formation of nano-assemblies using the novel luminescent NpDDT linker.

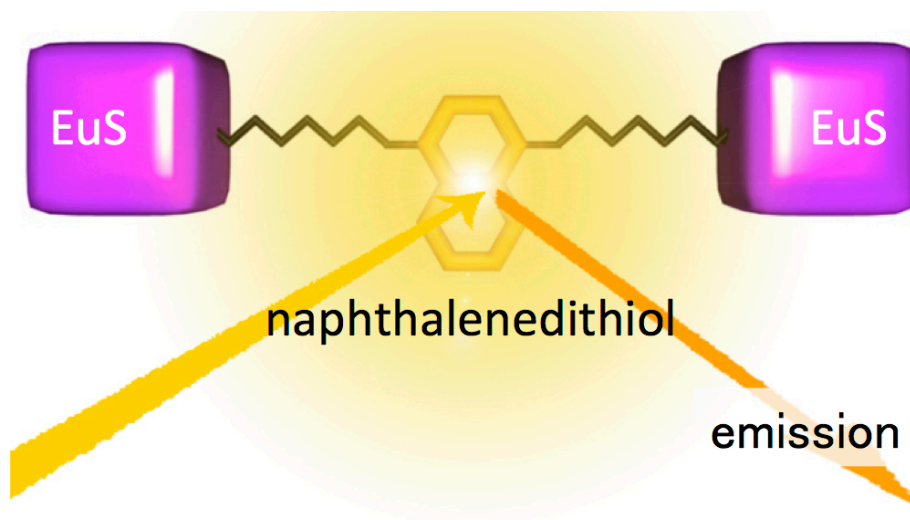


Figure 2-9. Illustration of the observation of the aggregation growth of EuS nanocrystals using luminescent NpDDT linker.

2.5 References

- 1 M. Bruchez, M. Moronne, P. Gin, S. Weiss, and A. P. Alivisatos, *Science* **1998**, *281*, 2013-2016.
- 2 N. L. Pickett and P. O'Brien, *The Chemical Record* **2001**, *1*, 467-479.
- 3 T. Trindade, P. O'Brien, and N. L. Pickett, *Chemistry of Materials* **2001**, *13*, 3843-3858.
- 4 N. Tessler, V. Medvedev, M. Kazes, S. Kan, and U. Banin, *Science* **2002**, *295*, 1506-1508.
- 5 S. Coe, W.-K. Woo, M. Bawendi, and V. Bulovic, *Nature* **2002**, *420*, 800-803.
- 6 W. U. Huynh, J. J. Dittmer, and A. P. Alivisatos, *Science* **2002**, *295*, 2425-2427.
- 7 V. I. Klimov, A. A. Mikhailovsky, S. Xu, A. Malko, J. A. Hollingsworth, C. A. Leatherdale, H.-J. Eisler, and M. G. Bawendi, *Science* **2000**, *290*, 314-317.
- 8 Y.-w. Jun, Y.-y. Jung, and J. Cheon, *Journal of the American Chemical Society* **2002**, *124*, 615-619.
- 9 N. S. Norberg, K. R. Kittilstved, J. E. Amonette, R. K. Kukkadapu, D. A. Schwartz, and D. R. Gamelin, *Journal of the American Chemical Society* **2004**, *126*, 9387-9398.
- 10 S. C. Erwin, L. Zu, M. I. Haftel, A. L. Efros, T. A. Kennedy, and D. J. Norris, *Nature* **2005**, *436*, 91-94.
- 11 P. Wachter, *CRC Critical Reviews in Solid State Sciences* **1972**, *3*, 189-241.
- 12 P. Wachter. in *Handbook on the Physics and Chemistry of Rare Earths* Vol. 2

- (eds Karl A. Gschneidner, Jr. and Eyring LeRoy) 507-574 (Elsevier, 1979).
- 13 T. Kasuya, *Journal of Magnetism and Magnetic Materials* **1999**, *195*, 141-147.
- 14 J. C. Suits, B. E. Argyle, and M. J. Freiser, *Journal of Applied Physics* **1966**, *37*, 1391-1397.
- 15 T. Kataoka, Y. Tsukahara, Y. Hasegawa, and Y. Wada, *Chemical Communications* **2005**, 6038-6040.
- 16 M. D. Regulacio, K. Bussmann, B. Lewis, and S. L. Stoll, *Journal of the American Chemical Society* **2006**, *128*, 11173-11179.
- 17 Y. Hasegawa, T. Adachi, A. Tanaka, M. Afzaal, P. O'Brien, T. Doi, Y. Hinatsu, K. Fujita, K. Tanaka, and T. Kawai, *Journal of the American Chemical Society* **2008**, *130*, 5710-5715.
- 18 Y. Hasegawa, *Chemistry Letters* **2013**, *42*, 2-7.
- 19 S. A. Maier, P. G. Kik, H. A. Atwater, S. Meltzer, E. Harel, B. E. Koel, and A. A. G. Requicha, *Nat Mater* **2003**, *2*, 229-232.
- 20 E. V. Shevchenko, M. Ringler, A. Schwemer, D. V. Talapin, T. A. Klar, A. L. Rogach, J. Feldmann, and A. P. Alivisatos, *Journal of the American Chemical Society* **2008**, *130*, 3274-3275.
- 21 V. Lesnyak, A. Wolf, A. Dubavik, L. Borchardt, S. V. Voitekhovich, N. Gaponik, S. Kaskel, and A. Eychmuller, *Journal of the American Chemical Society* **2011**, *133*, 13413-13420.
- 22 S. A. Maier, P. G. Kik, H. A. Atwater, S. Meltzer, E. Harel, B. E. Koel, and A. A. G. Requicha, *Nature Materials* **2003**, *2*, 229-232.

- 23 A. Tanaka, H. Kamikubo, Y. Doi, Y. Hinatsu, M. Kataoka, T. Kawai, and Y. Hasegawa, *Chemistry of Materials* **2010**, *22*, 1776-1781.
- 24 A. Tanaka, H. Kamikubo, M. Kataoka, Y. Hasegawa, and T. Kawai, *Langmuir* **2010**, *27*, 104-108.
- 25 P. Charoonniyomporn, T. Thongpanchang, S. Witayakran, Y. Thebtaranonth, K. E. S. Phillips, and T. J. Katz, *Tetrahedron Letters* **2004**, *45*, 457-459.
- 26 H. Tu, S. Yang, V. Chikan, and D. F. Kelley, *The Journal of Physical Chemistry B* **2004**, *108*, 4701-4710.
- 27 R. Koole, P. Liljeroth, C. de Mello Donegá, D. Vanmaekelbergh, and A. Meijerink, *Journal of the American Chemical Society* **2006**, *128*, 10436-10441.

Chapter 3

Enhanced Magneto-optical Properties of Semiconductor EuS Nanocrystals Assisted by Surface Plasmon Resonance of Gold Nanoparticles

3.1 Introduction

Modern optical telecommunication systems are playing an ever-increasing role in our information-intensive society^[1]. In recent years, intense worldwide effort has been focused on researching optical telecommunication devices such as lasers, optical fibers, and photonic devices^[2-8]. In particular, the optical isolator is a key device that allows the transmission of light in only one direction, which is essential for high-speed and highly accurate optical information technology. The performance of an optical isolator is based on the optical Faraday effect. The optical Faraday effect causes rotation

of the plane of polarized light, and the magnitude of this rotation is linearly proportional to the component of magnetic field in the direction of propagation. Various types of magneto-optical materials showing the Faraday effect have been reported over the past few decades^[9-19]. In particular, the preparation of semiconductor materials with magnetic dopants has been investigated for the development of optical isolators. In addition, stochastic control of a number of magnetic dopants in II–VI or III–V systems has also been investigated^[20-22]. Currently, fiber-optic communication systems in the visible region are focused on wavelength division multiplex (WDM) technology for telecommunications and optical sensors for medical equipment^[23-25]. Previous semiconductor CdTe:Hg nanocrystals showed a large Faraday effect in the visible region (150 degree cm⁻¹ at 633 nm, 0.1 T)^[26,27]; however, concerns about the toxicity of these materials hampered their application. Optical glass containing paramagnetic Tb(III) ions, currently used in the visible region, has a low Faraday effect efficiency (7 degree cm⁻¹ at 633 nm, 0.1 T)^[28,29]. Thus, effective new materials with a high Faraday effect efficiency in the visible region are crucially required for future photonic science and engineering development.

A promising and important material for use in optical isolators is EuS, a magnetic semiconductor with favorable magnetic and optical properties^[30-35]. EuS is characterized by degenerate $4f$ orbitals of Eu(II) ions existing between the conduction band ($5d$ orbitals of Eu(II)) and the valence band ($3p$ orbitals of S²⁻); the $4f$ – $5d$ electronic transition and spin configuration leads to the generation of a strong magneto-optical (Faraday) effect, which makes this a promising active material for

future optical isolators^[36-55]. In particular, EuS nanocrystals are distinctly characterized by their ferromagnetic properties and strong Faraday effect in the blue-light region^[56].

In this chapter, the author proposes a new optical isolator composed of the intrinsic magnetic semiconductor EuS nanocrystals, which are intrinsic magnetic semiconductor, and brilliant gold nanoparticles. That the brilliance of gold is caused by localized surface plasmon resonance (LSPR), an electromagnetic excitation existing on the surface of a gold, is well known (Figure 3-1). These electromagnetic field is confined to the near vicinity of the interface that leads to unique and unusual photophysical enhancement^[57]. This LSPR-based photophysical enhancement has recently been focused on in the areas of photophysics, materials chemistry, biological science, and advanced photonics, for enhancing luminescence and photo-catalytic properties^[58-61]. Artemyev and co-workers revealed that excitation of the LSPR band of gold nanoparticles promotes efficient luminescence of neighboring CdSe nanoparticles^[58]. Small magneto-optical enhancements of Bi:YIG and iron oxide crystals covered with gold layer or thin-film have also reported, preliminarily^[62-66]. However, direct evidence of amplification of the Faraday effect assisted by LSPR is not clear currently. To analyze and estimate magneto-optical signal amplification by LSPR, precise control of gold particle size and the distance between gold and magnetic materials at the nanoscale would be required.

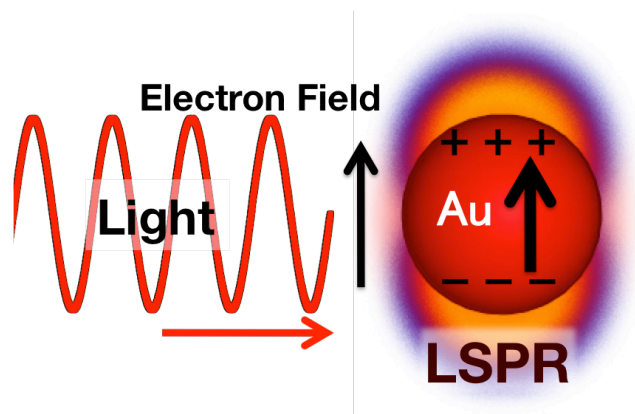


Figure 3-1. Illustration of the LSPR excited on the Au nanoparticle.

Here, the author reports on the successful and remarkable magneto-optical property of a new isolator material based on molecular synthetic technology, that is, EuS nanocrystals directly linked with gold nanocrystals (EuS-Au nanosystems, Figure 3-2). The distance between the EuS and Au nanocrystals is controlled accurately using organic molecules, namely, 1,2-ethanedithiol (EDT), 1,6-hexanedithiol (HDT), 1,10-decanedithiol (DDT), 1,4-bisethanethionaphthalene (NpEDT), or 1,4-bisdecane-thionaphthalene (NpDDT). The Faraday effect is estimated using polymer thin films containing the EuS-Au nanosystem (matrix: polymethylmethacrylate (PMMA)). Efficient Faraday rotation results from a specific spin configuration of the EuS-Au nanosystem under photo-irradiation. The characteristic spin configuration was also investigated using photon-assisted electron spin resonance (ESR). The study and development of LSPR-assisted magneto-optical enhancement of EuS is expected to open up a new field of photophysics and photonic science. A practical and scientific method of photo-signal amplification using EuS-Au nanosystems controlled based on the interparticle distance is described in this chapter.

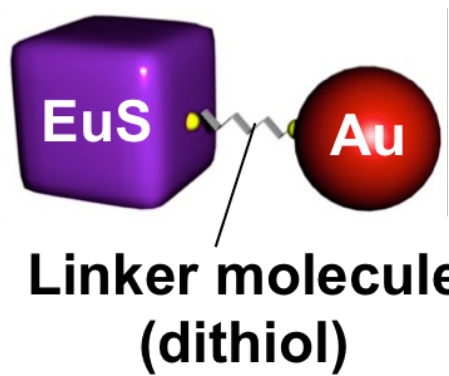


Figure 3-2. Illustration of the EuS-Au nanosystems linked with linker molecule.

3.2 Experiments

3.2.1 Materials

Europium(III) chloride hexahydrate ($\text{EuCl}_3 \cdot 6\text{H}_2\text{O}$) and sodium *N,N*-diethyldithiocarbamate trihydrate ($\text{Na}(\text{S}_2\text{CNET}_2) \cdot 3\text{H}_2\text{O}$) were purchased from Kanto Chemical Co. Inc. Tetrachloroaurate(III) tetrahydrate ($\text{HAuCl}_4 \cdot 4\text{H}_2\text{O}$), tetraphenylphosphonium bromide (BrPPh_4), triphenylphosphine (PPh_3), 1,6-hexanedithiol (HDT), and chloroform were purchased from Wako Pure Chemical Industry, Ltd. Oleylamine (OA), 1,2-ethanedithiol (EDT), 1,10-decanedithiol (DDT), 1,4-dihydroxynaphthalene, and *p*-toluenesulfonic acid were obtained from Tokyo Chemical Industry Co., Ltd. All other chemicals and solvents were reagent grade and were used without further purification.

3.2.2 Apparatus

FT-IR measurements performed at room temperature using a JASCO FT/IR-350 spectrometer. ^1H NMR data were measured by a JEOL AL-300 (300 MHz). ^1H NMR chemical shifts were determined by using TMS as an internal standard. Elemental analyses were performed on a J-Science Lab JM 10 Micro Corder and an Exeter Analytical CE440. XRD patterns were characterized by a RIGAKU X-ray diffractometer RINT 2200 using Cu K α radiation source ($\lambda = 0.15418$ nm). High-resolution images of the EuS-Au nanosystems were obtained with TEM, the JEOL 2010 FASTEM (200 kV), and high-resolution TEM (HR-TEM), the JEM-ARM1300.

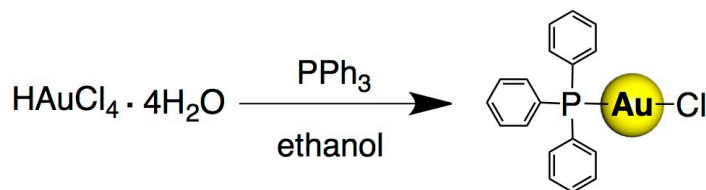
UV-vis absorption spectra were measured on a JASCO V-570 spectrophotometer at room temperature. The thicknesses of the PMMA thin film containing the EuS-Au nanosystem were obtained by using a surface profiler (KLA Tencor ALPHA-STEP IQ). Electron spin resonance (ESR) spectra of EuS-Au nanosystems were measured using a JEOL JES-TE200 ESR spectrometer.

3.2.3 Syntheses

Preparation of Cube-Shaped EuS nanocrystals:

EuS nanocrystals were used as same as described in Chapter 2. They were synthesized by the thermal reduction of the single source precursor, $(\text{PPh}_4)[\text{Eu}(\text{S}_2\text{CNET}_2)_4]$, in oleylamine under N_2 atmosphere at 180°C for 20 min and then at 300°C for 6 h. Prepared EuS nanocrystals was formed monodisperse nanocrystals with cubic shape, and the crystal size of EuS nanocrystals was found to be approximately 18.5 nm evaluated by the TEM observations.

Synthesis of Chloro(triphenylphosphine) Gold(I) ($[\text{PPh}_3\text{AuCl}]$):



Scheme 3-1. Reaction scheme of $[\text{PPh}_3\text{AuCl}]$.

A solution of HAuCl_4 (10.0 g, 24.3 mmol) in ethanol (150 mL) was added, with stirring, to PPh_3 (12.7 g, 48.6 mmol) dissolved in ethanol (100 mL) heated under reflux for several hours, and cooled to room temperature. The resulting precipitate was separated by filtration and washed 2 times with ethanol. Recrystallization from hexane gave white crystals of $[\text{PPh}_3\text{AuCl}]$. ^1H NMR (300 MHz, CDCl_3 , 25°C , TMS): $\delta = 7.50$ ppm (m, 15H, Ar-H); IR (KBr): $\tilde{\nu} = 1407 \text{ cm}^{-1}$ (P-Phenyl); elemental analysis calcd (%) for $\text{C}_{18}\text{H}_{15}\text{AuCl}$: C 43.70, H 3.06, N 0; found: C 43.58, H 3.02, N 0.

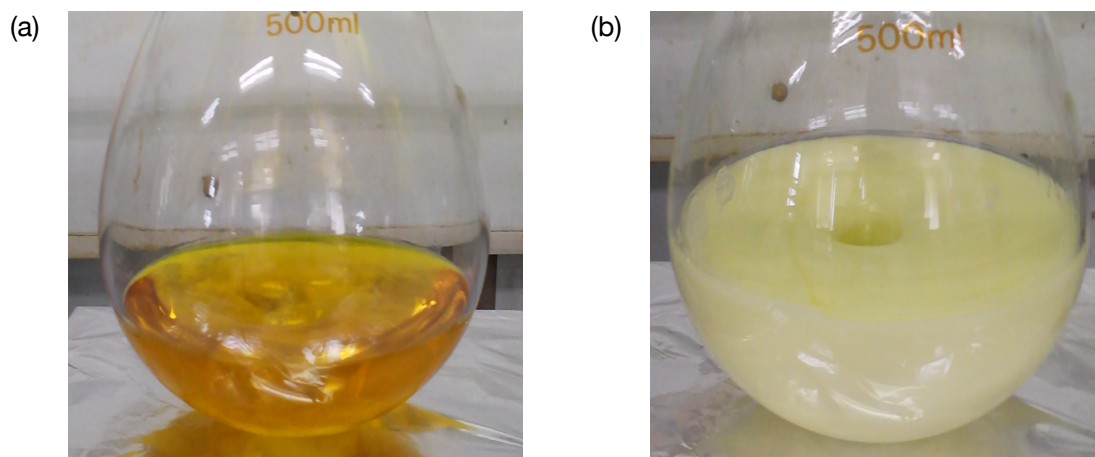
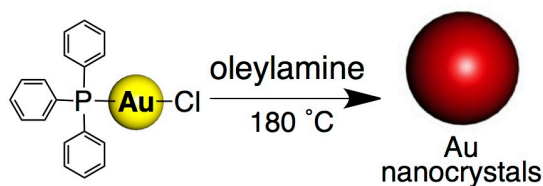


Figure 3-3. Photographs of the synthesis of $[PPh_3AuCl]$ (a) before and (b) after reaction.

Synthesis of Au Nanoparticles:



Scheme 3-2. Reaction scheme of Au nanoparticles.

Under N_2 atmosphere $[PPh_3AuCl]$ (0.50 g, 1.01 mmol) was dissolved into oleylamine (30 mL, 91.2 mmol), and the mixture was heated at $180^\circ C$ and stirred for 10, 30 or 60 min to synthesize for the Au nanoparticles with different crystal sizes. After the solution was cooled to room temperature, the red liquid was centrifuged at 4000 rpm for 10 min. The precipitation was added to chloroform (20 mL) and centrifuged at 4000 rpm for 15 min, and the clear red liquid of oleylamine capped Au nanoparticles was obtained.

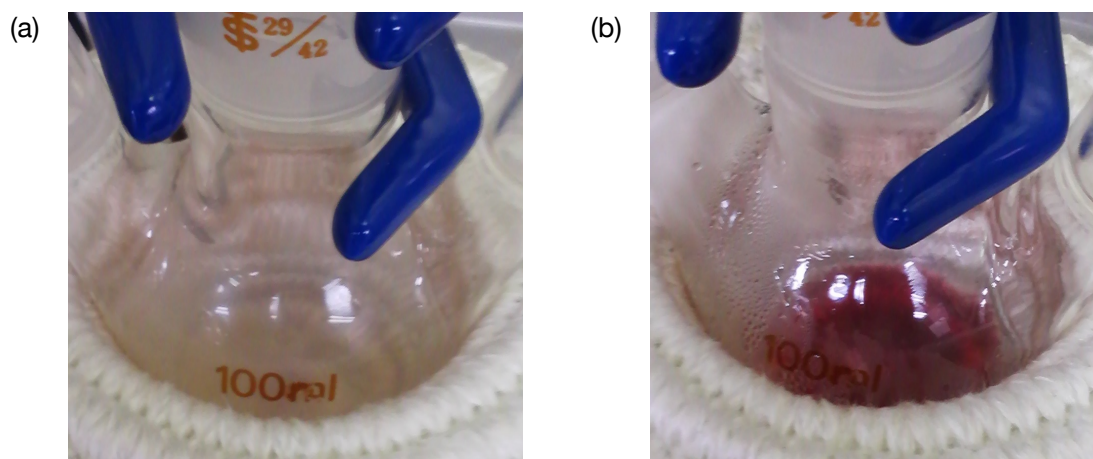
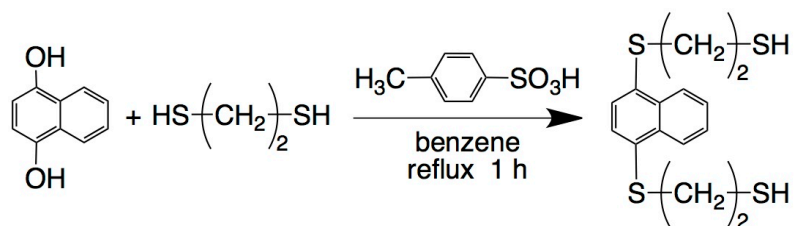


Figure 3-4. Photographs of the synthesis of Au nanoparticles (a) before and (b) after reaction.

Synthesis of 1,4-bisethanethionaphthalene (NpEDT):



Scheme 3-3. Reaction scheme of NpEDT.

1,4-bisethanethionaphthalene (NpEDT) was prepared by previously reported^[67]. Under N₂ atmosphere, 1,4-dihydroxynaphthalene (0.16 g, 1.0 mmol), *p*-toluenesulfonic acid (0.095 g, 0.5 mmol) and 1,2-ethanedithiol (EDT, 1.0 mL, 12 mmol) were dissolved into benzene (10 mL), and the mixture was refluxed at 80°C for 1 h. After aqueous workup, the product was purified by column chromatography on silica gel using ethyl acetate as an eluent. The collected product was crystallized from a mixture of ethyl acetate and hexane to give NpEDT as a white solid. ¹H NMR (300 MHz, CDCl₃, 25°C, TMS): δ = 8.4-8.5 (m, 2H, CH), 7.5-7.6 (m, 2H, CH), 7.5 (s, 2H, CH), 3.1-3.2 (m, 4H,

CH₂), 2.6-2.7 (m, 4H, CH₂), 1.7 (t, 2H, SH) ppm; IR (KBr): $\tilde{\nu} = 2930, 2850 \text{ cm}^{-1}$ (C-Hst), 2540 cm^{-1} (S-Hst), 1550 cm^{-1} (arC-C), 1490 cm^{-1} (C-H δ ip).

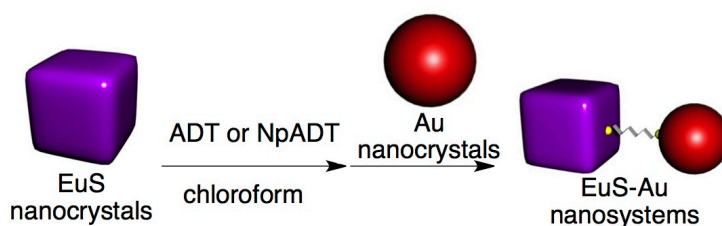
Synthesis of 1,4-bisalkanethionaphthalene (NpDDT):

1,4-bisdecanethionaphthalene (NpDDT) was used as same as described in Chapter 2.

Ligand Exchange Reactions:

Dithiol capped EuS nanocrystals were obtained by adding 0.08 g of EuS nanocrystals dissolved in chloroform (20 mL) to a solution of 0.01-0.03 mole equivalents of dithiol ligand (1,2-ethanedithiol (EDT), 1,6-hexanedithiol (HDT), 1,10-decanedithiol (DDT), 1,4-bisethanethionaphthalene (NpEDT), or 1,4-bisdecanethionaphthalene (NpDDT)) in chloroform. After the reaction solvent was stirred for 5 h at room temperature, the resulting solution was centrifuged at 4000 rpm for 10 min. The precipitation was added to 20 mL of chloroform, and the liquid of dithiol capped EuS nanocrystals (EuS-EDT, -HDT, -DDT, -NpEDT, or -NpDDT) was obtained.

Synthesis of EuS-Au Nanosystems:



Scheme 3-4. Reaction scheme of EuS-Au nanosystems.

The EuS-Au nanosystems were formed by adding the solution of Au nanoparticles in chloroform to the solution of alkanedithiol capped EuS nanocrystals in chloroform, and then the mixture was stirred for 5 h at room temperature. The solution was added to 1-dodecanethiol (1 mL), which keeps EuS nanocrystals from aggregation of themselves, and stirred for 1 h. The resulting solution of EuS-dithiol-Au nanosystems (dithiol: EDT, HDT, DDT, NpEDT, or NpDDT) in chloroform was obtained.

Synthesis of EuS-Au Nanosystems Consisted of Different Au Nanoparticles:

Au nanoparticles with different grain size were prepared by reaction time changing for 10, 30, and 60 min, and their particle sizes were estimated to be 8, 18.5, and 73 nm by TEM measurements, respectively. EuS-DDT-Au nanosystems were prepared by same method.

3.2.4 Preparation of Polymer Thin Films

The obtained EuS-Au nanosystems (2 mg) were added to a chloroform solution (8 mL) of PMMA (2.0 g) and dispersed well under ultrasonic treatment, giving the colloidal suspension. The PMMA thin films were prepared on a glass substrate from the colloidal suspension via a casting method for the Faraday rotation measurements. The Faraday effect measurements were performed using a measurement system for Faraday and Kerr effects (JASCO, Model K-250). A Xe lamp was used as the light source. The external magnetic field was 15,000 Oe.

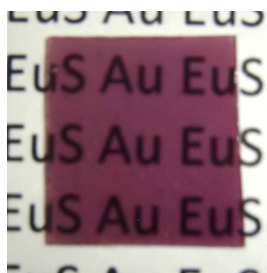


Figure 3-5. Photographs of the prepared PMMA thin film containing EuS-Au nanosystems.

3.3 Results and Discussion

3.3.1 Synthesis of Au Nanoparticles

In the typical method, monodisperse Au nanoparticles was synthesized via thermal reaction of the chloro(triphenylphosphine) gold(I) complex (PPh_3AuCl) as a single source precursor in oleylamine at 180°C for 30 min in N_2 atmosphere. The prepared powder was separated by centrifugation and washed with toluene. After washing, a red Au powder was obtained. XRD confirmed the formation of crystalline Au nanoparticles (Figure 3-10). The diffraction peaks at $2\theta = 38.3, 44.4, 64.4, 77.6,$ and 81.6 degree were assigned to the (111), (200), (220), (311), and (222) planes, respectively, of face-centered-cubic (fcc) Au (ICDD 4-0784, $Fm\bar{3}m$). The intensity ratios of the diffraction patterns agreed with those of bulk Au. The author evaluated full width at half maximum (FWHM) of the $2\theta = 38.3$ degree peak, which corresponded to Bragg diffraction from the Au (111) plane. The crystal grain size of Au nanoparticles calculated from the XRD pattern using the Scherer equation was 16.4 nm.

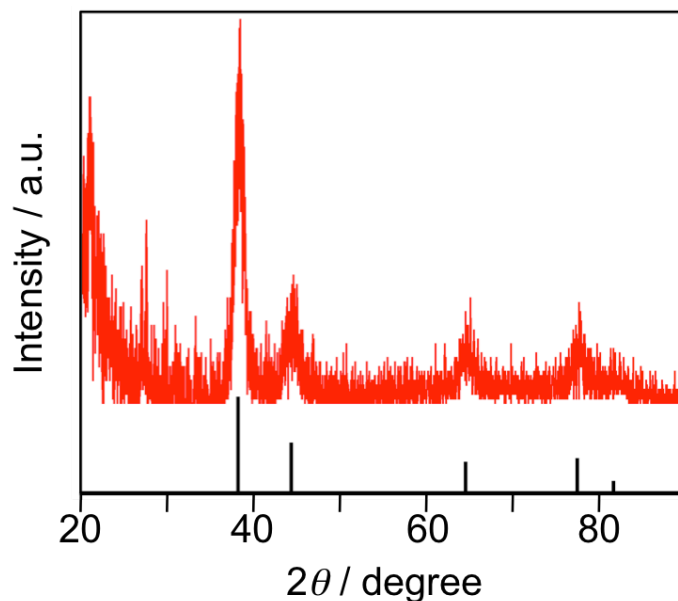


Figure 3-6. XRD pattern of Au nanoparticles. Black line in XRD pattern is based on the ICDD (4-0784, *Fm3m*) for Au crystals.

TEM images and size distribution histograms of Au nanoparticles are shown in Figure 3-7. TEM observations showed that all Au nanoparticles had typically spherical shapes, and their average particle sizes for reaction times of 10, 30, and 60 min were 8, 18, and 73 nm, respectively. Thus, spherical Au nanoparticles of different particle sizes (8, 18, and 73 nm) were synthesized successfully.

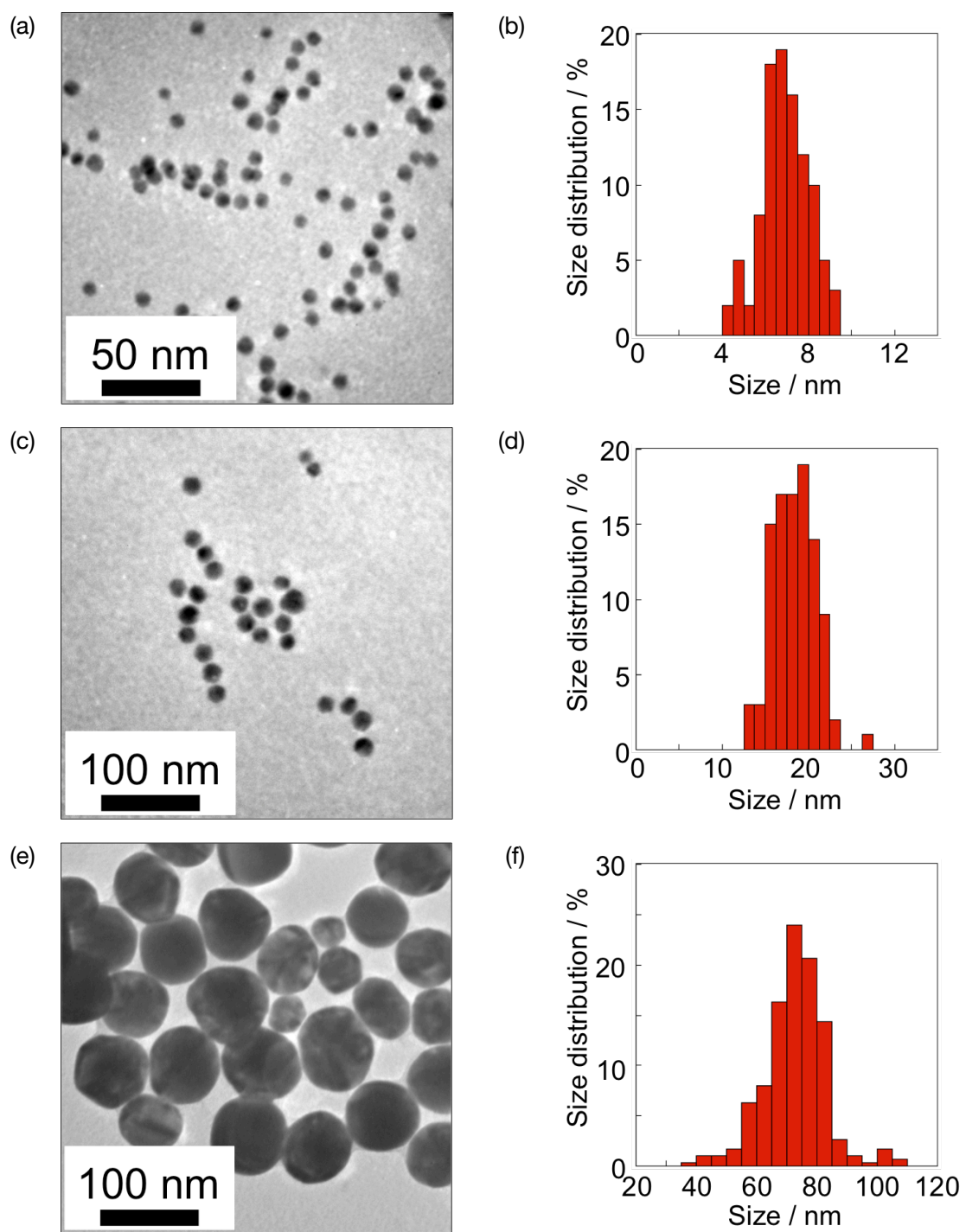


Figure 3-7. (a, c, e) TEM images and (b, d, f) size distribution histogram of sphere-shaped Au nanoparticles with different particle size, 8, 18, and 73 nm, respectively.

3.3.2 Preparation of EuS-Au Nanosystems

The prepared EuS nanocrystals were attached to Au nanocrystals using a self-assembly technique. First, as a pretreatment, the surfaces of the EuS nanocrystals were covered with alkanedithiols, namely, 1,2-ethanedithiol (EDT), 1,6-hexanedithiol (HDT), 1,10-decanedithiol (DDT), 1,4-bisethanethionaphthalene (NpEDT), or 1,4-bisdecanethionaphthalene (NpDDT), as linker molecules. To confirm the presence of dithiols on the EuS surface, the author carried out IR measurements (Figure 3-9). Characteristic IR absorption bands of dithiol-capped EuS nanocrystals (EuS-NpDDT) after centrifugation process were observed at 2670 cm^{-1} (S-H st) and 1470 cm^{-1} (Ar). IR band shapes of EuS-NpDDT at 1470 cm^{-1} and 2670 cm^{-1} are much different from those of NpDDT molecules. These different shapes and wavenumber shifts might have been caused by stacking of naphthalene units on the EuS surface. The author considered that NpDDT was attached onto the EuS surface.

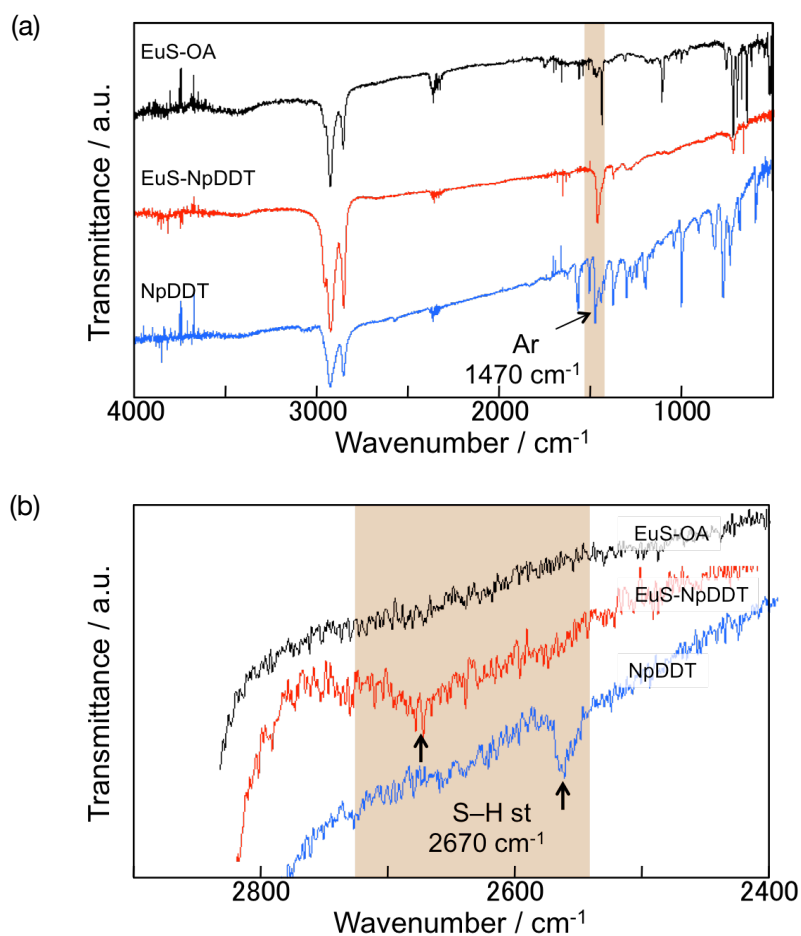


Figure 3-9. IR spectra of oleylamine-capped EuS nanocrystals (EuS-OA, black), dithiol-capped EuS nanocrystals (EuS-NpDDT, red) and NpDDT (blue). (b) The magnification of IR spectra between 2400 and 3000 cm⁻¹. The IR spectra show the existence of the naphthalene unit (1470 cm⁻¹, Ar) and thiol unit (2670 cm⁻¹, S-H st).

After pretreatment with linker-molecules, the surface-modified EuS nanocrystals were attached to Au nanocrystals in a chloroform solution. High-resolution TEM (HR-TEM) images of the prepared EuS-Au nanosystems are shown in Figure 3-10. The author observed cubic EuS nanocrystals attached to spherical Au nanocrystals with clear lattice fringes. In the HR-TEM image, the crystallinity was clear and well-resolved, and lattice planes of EuS (0.21 nm (220)) and Au (0.24 nm (111)) were observed.

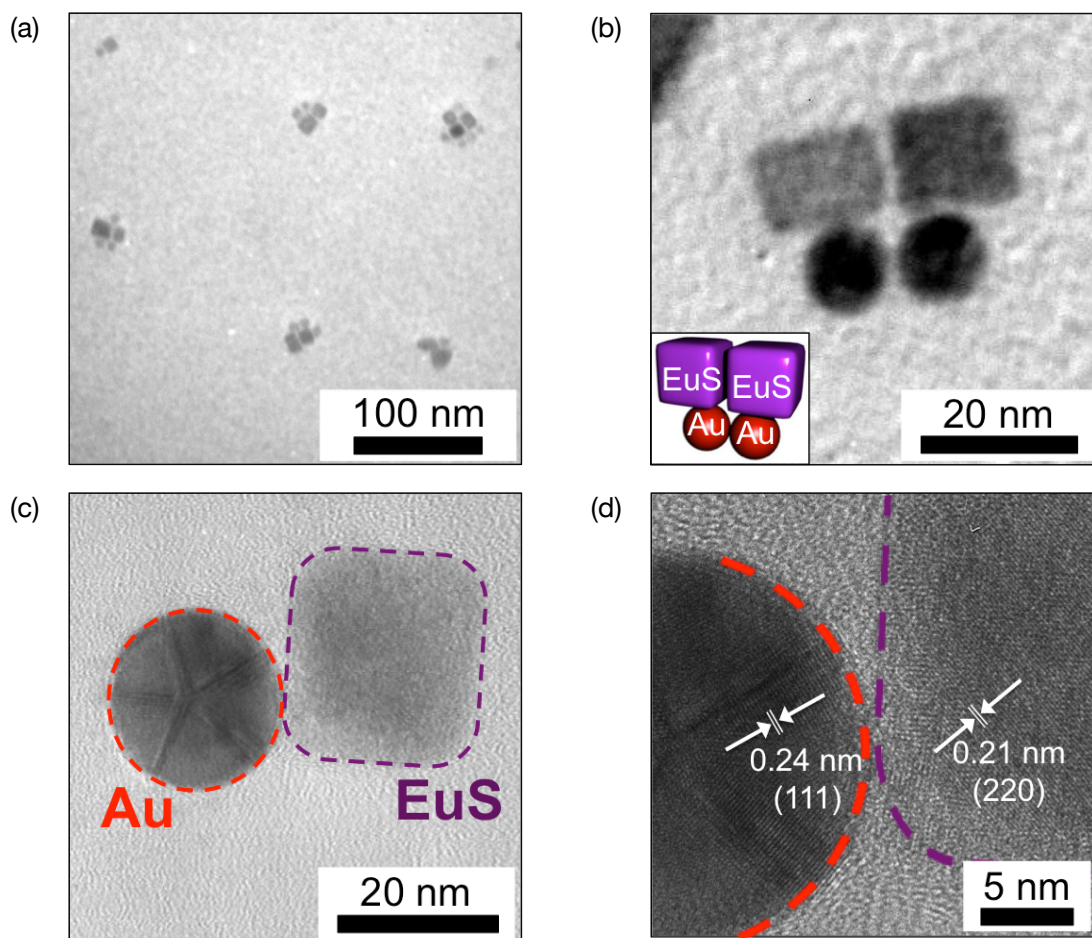


Figure 3-10. (a and b) TEM images of EuS–Au nanosystems. (c and d) High-resolution TEM images of EuS–Au nanosystems.

The average distances between EuS and Au in EuS-EDT-Au (linker: EDT), EuS-HDT-Au (linker: HDT), EuS-DDT-Au (linker: DDT), EuS-NpEDT-Au (linker: NpEDT), and EuS-NpDDT-Au (linker: NpDDT) estimated from TEM observations were 0.97, 1.54, 1.91, 1.81, and 3.52 nm, respectively (Figure 3-11). Thus, the author successfully prepared EuS-Au nanosystems with various distances between the EuS and Au nanocrystals (Figure 3-12).

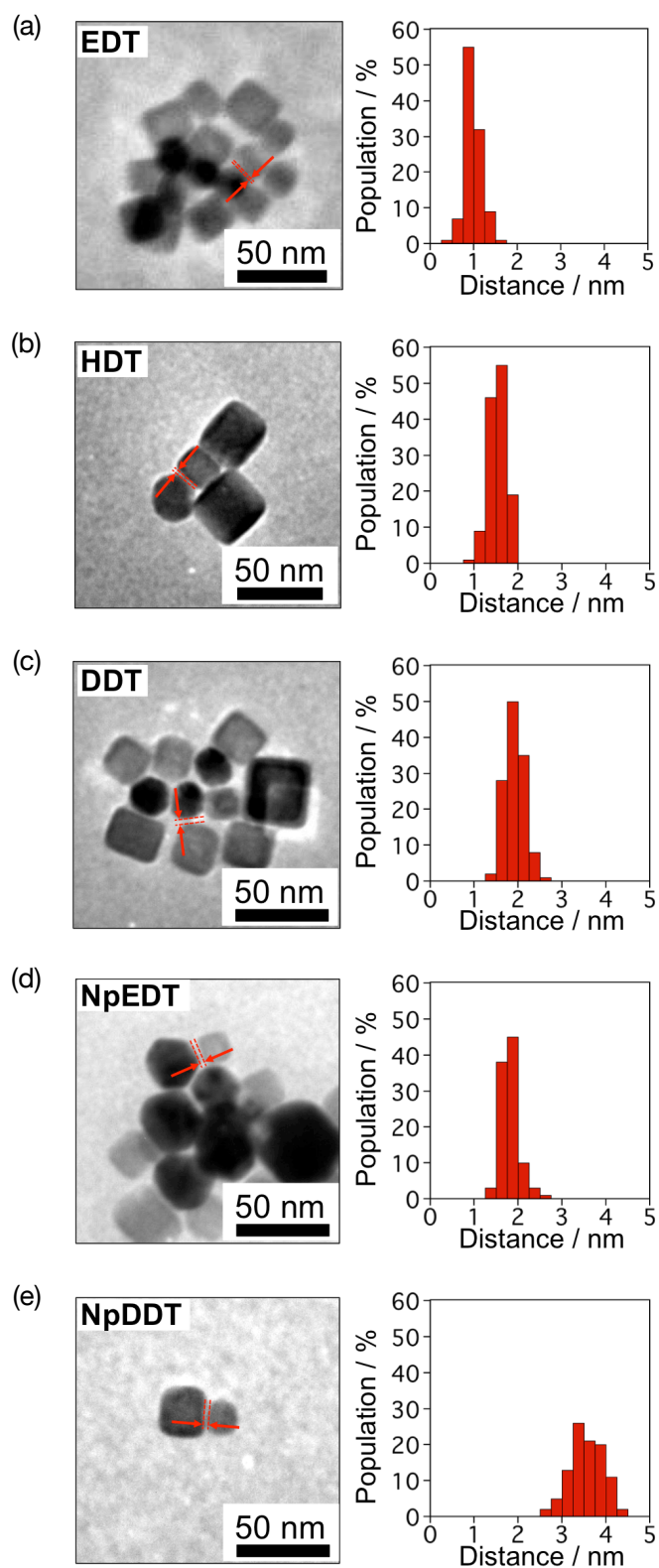


Figure 3-11. TEM images (left) and interparticle gap distribution histogram (right) of EuS-Au nanosystems linked by (a) EDT, (b) HDT, (c) DDT, (d) NpEDT and (e) NpDDT.

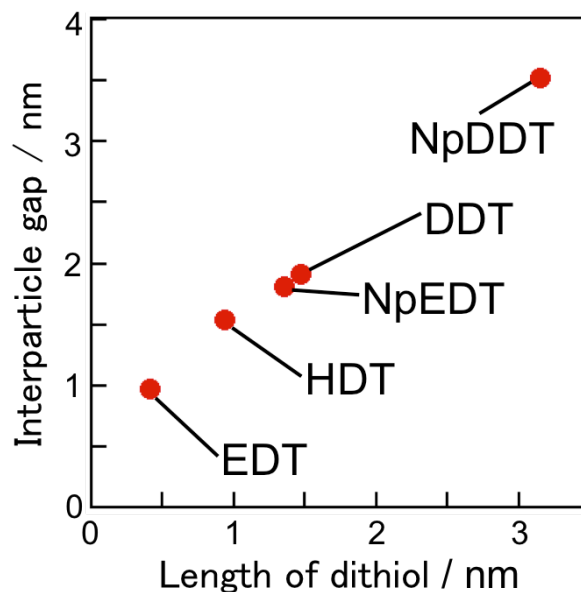


Figure 3-12. The relationship between interparticle gap measured from TEM images and length of dithiol used for formation of EuS-Au nanosystems.

To evaluate the optical properties of EuS-Au nanosystems, polymer thin films containing the EuS-Au nanosystems were prepared by casting EuS-Au nanosystems with polymethylmethacrylate (PMMA) in chloroform. The thickness of the PMMA thin film containing the EuS-Au nanosystem, as obtained using a surface profiler, was 10 μm . The absorption spectra of the PMMA thin films containing EuS-Au nanosystems are shown in Figure 3-13. The broad absorption band at 513 nm was assigned to the $4f-5d$ transition in the EuS nanocrystals. In addition, the author also found a specific absorption band at around 700 nm, which is much different from the wavelength of the LSPR band of the prepared Au nanocrystals. Such a red shift of the LSPR band is observed in dielectronic surroundings^[68-70]. The specific absorption band at 700 nm might have been caused by the LSPR band of the Au linked to large dielectric EuS nanocrystals. Moreover, the distance between EuS and Au was dependent on the length

of the dithiols. The dependence of the characteristic red shifts of LSPR and distance on the thiol moiety suggests that the Au nanoparticles were directly linked with the dithiol-covered EuS nanocrystals.

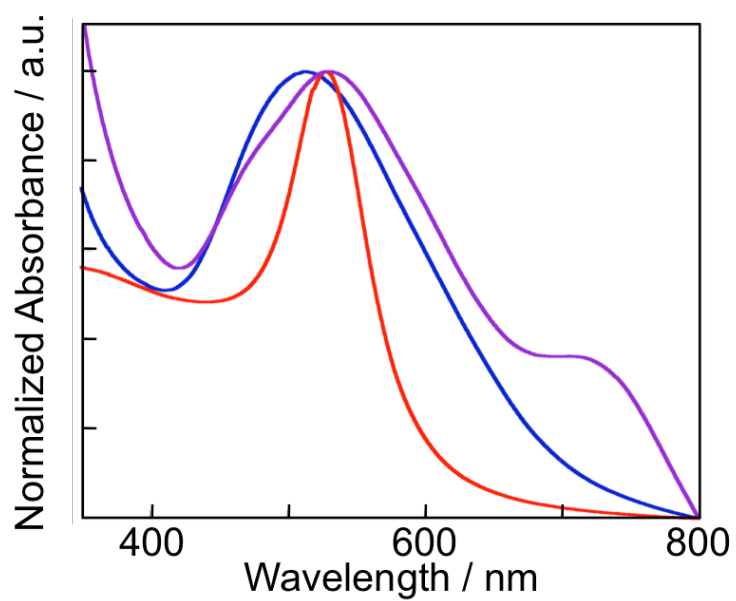


Figure 3-13. UV-Vis absorption spectra of EuS nanocrystals (blue) and EuS–Au nanosystems (red).

3.3.3 Magneto-optical Properties

The wavelength dependence of the Faraday rotation angle was measured for the PMMA thin films containing the EuS-Au nanosystems. The Faraday rotation spectrum at room temperature under an external magnetic field of 15,000 Oe showed clear positive and negative peaks, which could have contributed to the $4f-5d$ transition in the EuS nanocrystals. Verdet constants were normalized by the photon-absorption ability of the EuS-Au nanosystems, as well as EuS nano-assemblies described in Chapter 2, and the normalized Verdet constants (V_{abs}) are expressed as the following Equation (3-1).

$$V_{\text{abs}} = \theta/HA \quad (3-1)$$

Before accounting for the influence of linker molecules, the author confirmed that the V_{abs} of polymer thin films with mixtures of EuS and Au nanocrystals (non-linked particles) was very similar to that of polymer thin films with EuS nanocrystals (Figure 3-14).

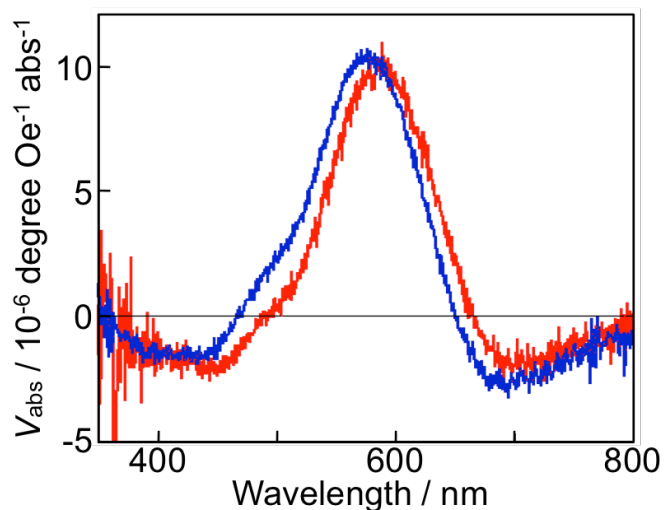


Figure 3-14. The calculated V_{abs} of polymer thin films containing EuS nanocrystals (red) and mixtures of EuS&Au nanocrystals (blue) under an external magnetic field of 15000 Oe.

The calculated V_{abs} of the EuS-Au nanosystems are shown in Figures 3-15, 3-16 and 3-17, and Table 3-1. First, the author observed that the Faraday rotation angle was dependent on the interparticle distance between the EuS and Au nanocrystals (Figure 3-15). Remarkable enhancement of the Faraday rotation angle of the polymer thin film with the EuS-DDT-Au nanosystems was observed, although the EuS-Au nanosystems with shorter interparticle distances (EuS-EDT-Au and EuS-HDT-Au nanosystems) yielded a smaller Faraday rotation angle than the EuS-DDT-Au nanosystems. Generally, the electric field associated with LSPR is affected by the interparticle distance between gold and functional materials such as semiconductors, luminescent dyes, and photochromic molecules. A small interparticle distance promotes quenching of the excited state of functional materials, resulting in decreased luminescent and photocatalytic efficiency. In contrast, the LSPR electric field does not affect materials with long interparticle distances^[68,71-74]. The author observed that the

V_{abs} of EuS-NpDDT-Au nanosystems decreased as the distance between EuS and Au increased (Table 3-1 and Figure 3-16). Therefore, the author considers that amplification of the Faraday rotation angle is also dependent on the interparticle distance.

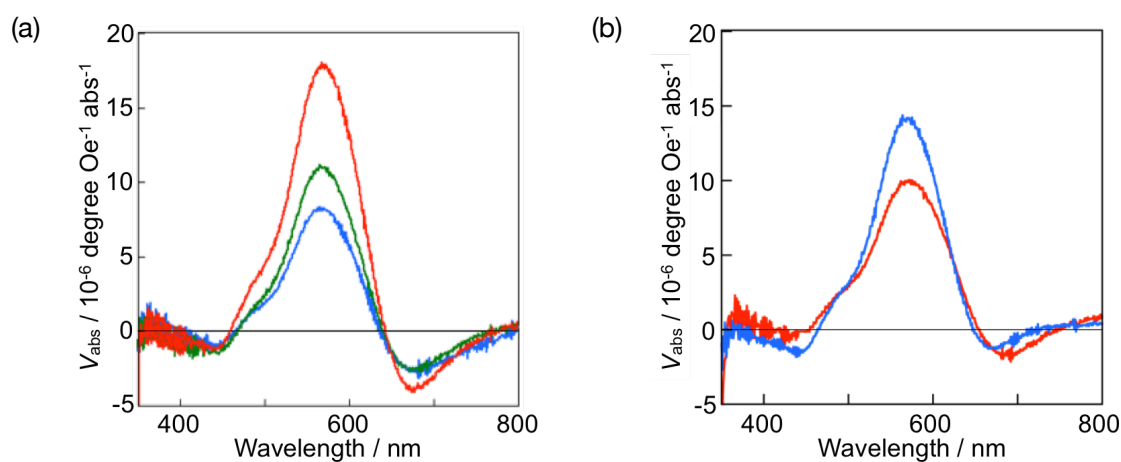


Figure 3-15. The calculated V_{abs} of polymer thin films containing EuS–Au nanosystems linked with (a) alkanedithiol (EDT (blue), HDT (green), and DDT (red)) and (b) naphthalenedithiol (NpEDT (blue) and NpDDT (red)) under an external magnetic field of 15000 Oe.

Table 3-1. Molecular length (d) and magneto-optical properties of EuS nanocrystals and EuS–Au nanosystems linked with EDT, HDT, DDT, NpEDT and NpDDT.

Sample	Molecular length d / nm	V_{abs} Peak position $\lambda_{\text{max}} / \text{nm}$	$V_{\text{abs, peak}}$ $/10^{-6} \text{ degree Oe}^{-1} \text{ abs}^{-1}$
EuS	–	563	14.8
EuS-EDT-Au	0.407	565	8.29
EuS-HDT-Au	0.937	565	11.1
EuS-DDT-Au	1.469	567	18.1
EuS-NpEDT-Au	1.356	567	14.4
EuS-NpDDT-Au	3.155	572	10.0

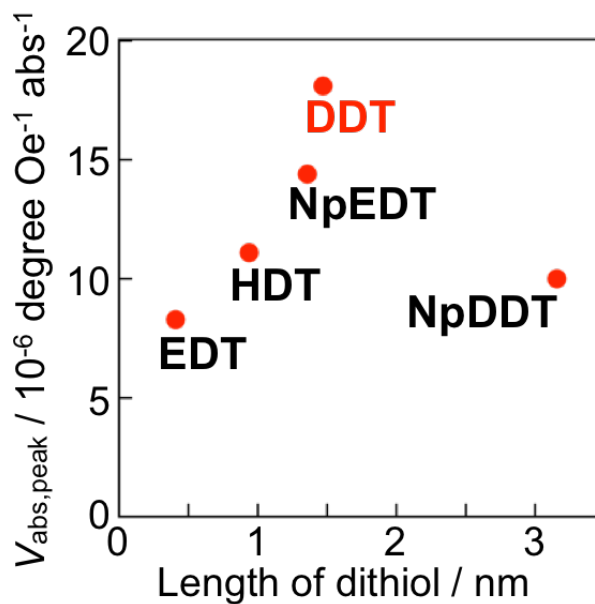


Figure 3-16. The relationship between calculated $V_{\text{abs, peak}}$ constants and molecular length of linker dithiols (EDT, HDT, DDT, NpEDT and NpDDT) of EuS–Au nanosystems.

Amplification of the Faraday effect of EuS-Au nanosystems is also dependent on Au particle size (Figure 3-17, Table 3-2, and their TEM images are shown in Figure 3-18). Au nanoparticles with a diameter of 18.5 nm yield greater amplification of the Faraday effect compared to those with diameters of 8 nm and 73 nm. For the size dependence of plasmon absorption, El-Sayed reported that the plasmon bandwidth of gold nanoparticles increases as the intrinsic size region decreases (mean diameter smaller than 25 nm) and increases as the extrinsic size region increases (mean diameter longer than 25 nm)^[75]. The broadening of the plasmon band is caused by transformation of the excitation energy into adsorbate levels located above the Fermi level. Therefore, effective LSPR is achieved using gold nanoparticles with a smaller plasmon band and particle diameter of around 25 nm. The author proposes that the observed amplification of Faraday effect of the EuS-DDT-Au nanosystems composed of 18.5 nm Au nanoparticles might have been caused by LSPR on Au nanoparticles with a smaller plasmon bandwidth.

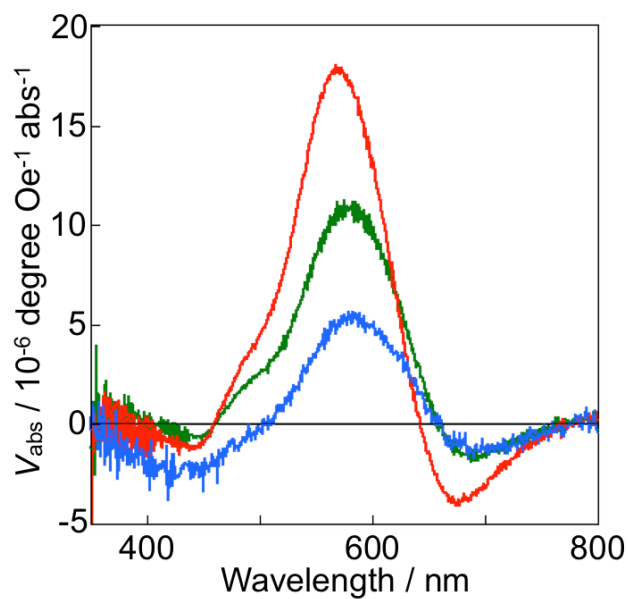


Figure 3-17. The calculated V_{abs} of polymer thin films containing EuS-DDT-Au nanosystems consisted of same EuS nanocrystals (particle size: 18.5 nm), but different particle size of Au nanoparticles, 8 nm (green), 18.5 nm (red), and 73 nm (blue).

Table 3-2. Particle size of Au nanoparticles in EuS-Au nanosystems and magneto-optical properties of EuS nanocrystals and EuS-Au nanosystems linked with EDT, HDT, DDT, NpEDT and NpDDT.

Sample	Particle size of Au / nm	V_{abs} Peak position λ_{max} / nm	$V_{\text{abs, peak}}$ / 10^{-6} degree Oe^{-1} abs^{-1}
EuS	–	563	14.8
EuS-DDT-Au	8	575	11.2
	18	567	18.1
	73	579	5.63

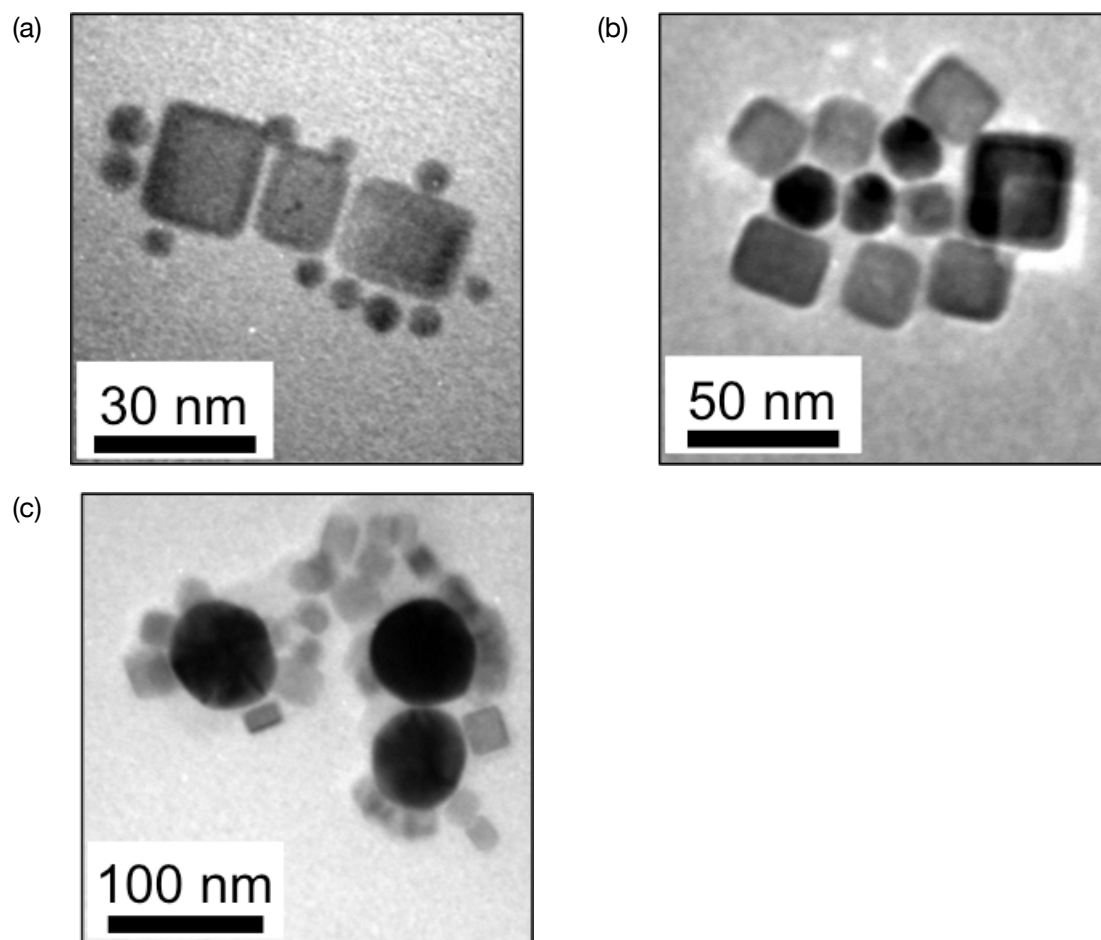


Figure 3-18. TEM images of EuS- DDT-Au nanosystems consisted of different particle size of Au nanoparticles: (a) 8, (b) 18, and (c) 73 nm.

3.3.3 Estimation of Spin Configuration under Photo-irradiation

To estimate the spin configuration of the EuS-Au nanosystems in the excited state, the author performed ESR measurements in the dark and under irradiation with a halogen lamp (150 W, $\lambda = 520$ nm; FWHM = 10 nm using a bandpass filter). The dark ESR spectra are shown in Figure 3-19. The signals at around 350 and 870 mT were caused by the characteristic spin configuration of Eu(II). The observed ESR signal from the EuS-Au nanosystems is larger than that from the corresponding EuS nanocrystals. The enhancement of the ESR signal in EuS-Au nanosystems might have been caused by specific $4f-5d$ spin-interactions on the EuS surface attached to the Au nanoparticles. Figure 3-19b shows the difference between the ESR spectra under dark and light conditions. For the EuS-DDT-Au nanosystem, large and small enhancements of the peaks at 350 mT and 870 mT, respectively, were observed. In contrast, for the EuS nanocrystals, only a small enhancement of the Eu(II) signal at 350 mT was observed. Signal enhancement of the EuS-Au nanosystem is linked directly to an increase in the magnetic spin polarization under irradiation. Recently, Hasegawa and co-workers reported that enhanced spin polarization in EuS nanoscale aggregates leads to an increase in the Faraday rotation signal^[56]. The author considers that large spin polarization in EuS nanocrystals leads to strong magneto-optical properties. The spin polarization of EuS nanocrystals in the electronic transition state can be estimated from the ESR spectra obtained under irradiation^[76]. An increase in the ESR signal due to irradiation may be one of the most important indicators of an enhanced Faraday effect in gold-assisted EuS, as observed in this chapter.

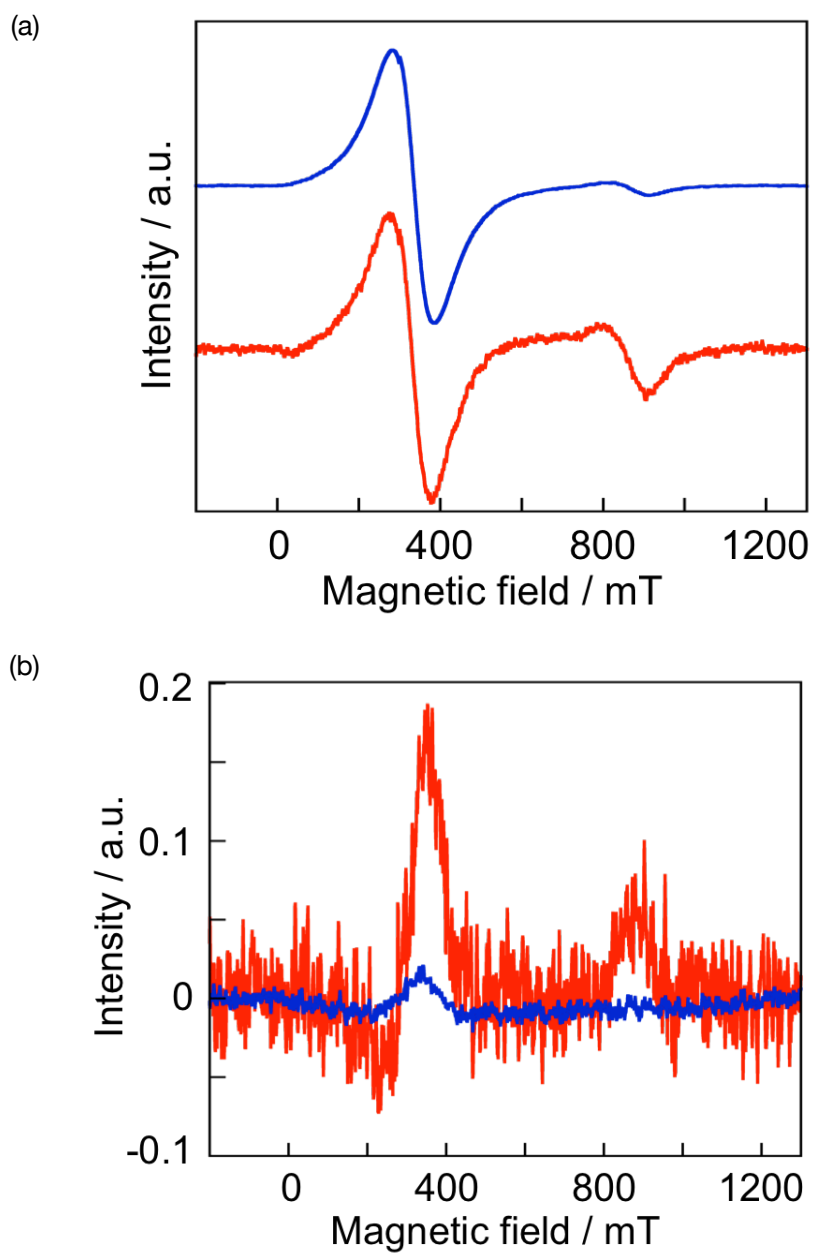


Figure 3-19. (a) ESR spectra of EuS nanocrystals (blue) and EuS-DDT-Au nanosystems (red). (b) The difference between the ESR spectra under dark and light condition with a halogen lamp (150 W, $\lambda = 520$ nm; FWHM = 10 nm using a band-pass filter) of EuS nanocrystals (blue) and EuS-DDT-Au nanosystems (red). The microwave frequency was 9.39 GHz, and the incident microwave power was 2.0 mW at room temperature.

3.4 Conclusions

Gold materials have attracted the attention of many researchers because of their brilliance resulting from LSPR. For the first time, this study suggests that brilliant gold can accelerate optical telecommunication systems. Here, the author successfully prepared cubic EuS nanocrystals attached to spherical Au nanoparticles to produce EuS-Au nanosystems. The magneto-optical properties of a EuS-Au nanosystem are dependent on the interparticle distance between EuS and Au, as well as the Au nanoparticle size. The enhanced spin-polarization of the EuS-Au nanosystems excited at the LSPR band of the Au nanoparticles was confirmed by photo-assisted ESR spectroscopy. New EuS-Au nanosystems amplify Faraday rotation under irradiation in the plasmon band of the gold parts. By controlling of irradiation in the plasmon band, the author fine tuned the Faraday rotation angle of EuS-Au nanosystems. The photo-switching system for the Faraday rotation angle could be employed in high-speed photonic routers for future photo information technology. Based on this work, the EuS-Au nanosystem is anticipated to open up new fields of innovative photo-information science and technology.

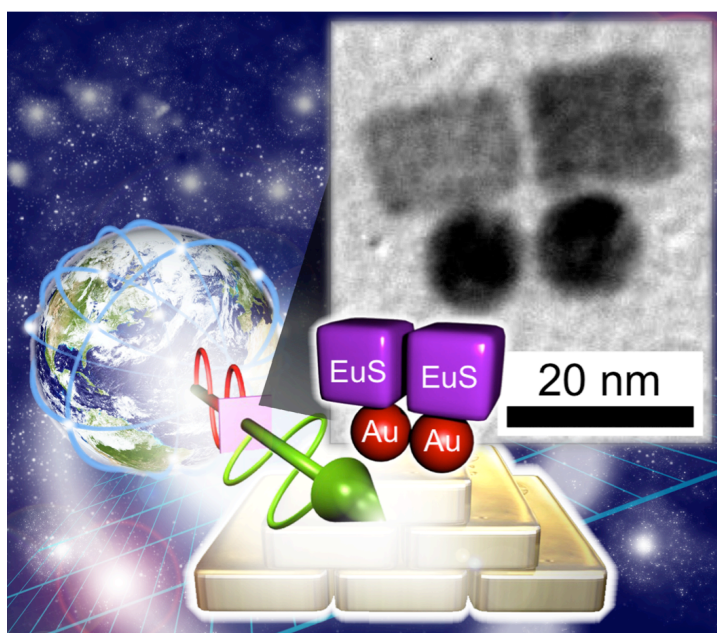


Figure 3-20. TEM image of EuS-Au nanosystems and illustration of the magneto-optical enhancement of EuS assisted by LSPR of Au nanocrystals.

3.5 References

- 1 N. Stafford, *Nature* **2010**, *467*, S19-S21.
- 2 S. Nakamura, *Science* **1998**, *281*, 956-961.
- 3 J. C. Knight, J. Broeng, T. A. Birks, and P. S. J. Russel, *Science* **1998**, *282*, 1476-1478.
- 4 T. W. Ebbesen, H. J. Lezec, H. F. Ghaemi, T. Thio, and P. A. Wolff, *Nature* **1998**, *391*, 667-669.
- 5 S. J. Pearton, J. C. Zolper, R. J. Shul, and F. Ren, *Journal of Applied Physics* **1999**, *86*, 1-78.
- 6 M. S. Gudiksen, L. J. Lauhon, J. Wang, D. C. Smith, and C. M. Lieber, *Nature* **2002**, *415*, 617-620.
- 7 P. Russell, *Science* **2003**, *299*, 358-362.
- 8 W. L. Barnes, A. Dereux, and T. W. Ebbesen, *Nature* **2003**, *424*, 824-830.
- 9 J. A. Gaj, J. Ginter, and R. R. Gałazka, *Physica Status Solidi B* **1978**, *89*, 655-662.
- 10 Y. Wang, N. Herron, K. Moller, and T. Bein, *Solid State Communications* **1991**, *77*, 33-38.
- 11 H. Ohno, A. Shen, F. Matsukura, A. Oiwa, A. Endo, S. Katsumoto, and Y. Iye, *Applied Physics Letters* **1996**, *69*, 363-365.
- 12 J. M. Kikkawa and D. D. Awschalom, *Nature* **1999**, *397*, 139-141.
- 13 T. Jungwirth, W. A. Atkinson, B. H. Lee, and A. H. MacDonald, *Physical*

- Review B* **1999**, *59*, 9818-9821.
- 14 D. J. Norris, N. Yao, F. T. Charnock, and T. A. Kennedy, *Nano Letters* **2000**, *1*, 3-7.
 - 15 K. Ando, H. Saito, Z. W. Jin, T. Fukumura, M. Kawasaki, Y. Matsumoto, and H. Koinuma, *Applied Physics Letters* **2001**, *78*, 2700-2702.
 - 16 Y.-w. Jun, Y.-y. Jung, and J. Cheon, *Journal of the American Chemical Society* **2002**, *124*, 615-619.
 - 17 H. Kato, T. Matsushita, A. Takayama, M. Egawa, K. Nishimura, and M. Inoue, *Journal of Applied Physics* **2003**, *93*, 3906-3911.
 - 18 N. S. Norberg, K. R. Kittilstved, J. E. Amonette, R. K. Kukkadapu, D. A. Schwartz, and D. R. Gamelin, *Journal of the American Chemical Society* **2004**, *126*, 9387-9398.
 - 19 S. C. Erwin, L. Zu, M. I. Haftel, A. L. Efros, T. A. Kennedy, and D. J. Norris, *Nature* **2005**, *436*, 91-94.
 - 20 H. Akinaga, S. Miyanishi, K. Tanaka, W. Van Roy, and K. Onodera, *Applied Physics Letters* **2000**, *76*, 97-99.
 - 21 K. Ando, H. Saito, Z. Jin, T. Fukumura, M. Kawasaki, Y. Matsumoto, and H. Koinuma, *Journal of Applied Physics* **2001**, *89*, 7284-7286.
 - 22 M. Inoue, R. Fujikawa, A. Baryshev, A. Khanikaev, P. B. Lim, H. Uchida, O. Aktsipetrov, A. Fedyanin, T. Murzina, and A. Granovsky, *Journal of Physics D: Applied Physics* **2006**, *39*, R151.
 - 23 J. Kido and Y. Okamoto, *Chemical Reviews* **2002**, *102*, 2357-2368.

- 24 J.-C. G. Bünzli, S. Comby, A.-S. Chauvin, and C. D. B. Vandevyver, *Journal of Rare Earths* **2007**, *25*, 257-274.
- 25 S. V. Eliseeva and J.-C. G. Bunzli, *Chemical Society Reviews* **2010**, *39*, 189-227.
- 26 C. Buss, R. Pankoke, P. Leisching, J. Cibert, R. Frey, and C. Flytzanis, *Physical Review Letters* **1997**, *78*, 4123-4126.
- 27 A. M. Shuvaev, G. V. Astakhov, A. Pimenov, C. Brüne, H. Buhmann, and L. W. Molenkamp, *Physical Review Letters* **2011**, *106*, 107404.
- 28 S. Ganschow, D. Klimm, P. Reiche, and R. Uecker, *Crystal Research and Technology* **1999**, *34*, 615-619.
- 29 V. I. Chani, A. Yoshikawa, H. Machida, and T. Fukuda, *Materials Science and Engineering B* **2000**, *75*, 53-60.
- 30 P. Wachter, *CRC Critical Reviews in Solid State Sciences* **1972**, *3*, 189-241.
- 31 P. Wachter. in *Handbook on the Physics and Chemistry of Rare Earths* Vol. 2 (eds Karl A. Gschneidner, Jr. and Eyring LeRoy) 507-574 (Elsevier, 1979).
- 32 D. Görlitz and J. Kötzler, *European Physical Journal B - Condensed Matter and Complex Systems* **1998**, *5*, 37-43.
- 33 T. Kasuya, *Journal of Magnetism and Magnetic Materials* **1999**, *195*, 141-147.
- 34 U. K. Sakalle, P. K. Jha, and S. P. Sanyal, *Bulletin of Materials Science* **2000**, *23*, 233-235.
- 35 J. Kunes, W. Ku, and W. E. Pickett, *Journal of the Physical Society of Japan* **2005**, *74*, 1408-1411.

- 36 J. C. Suits, B. E. Argyle, and M. J. Freiser, *Journal of Applied Physics* **1966**, *37*, 1391-1397.
- 37 Y. Hasegawa, S. Thongchant, Y. Wada, H. Tanaka, T. Kawai, T. Sakata, H. Mori, and S. Yanagida, *Angewandte Chemie International Edition* **2002**, *41*, 2073-2075.
- 38 S. Thongchant, Y. Hasegawa, Y. Wada, and S. Yanagida, *Journal of Physical Chemistry B* **2003**, *107*, 2193-2196.
- 39 F. Zhao, H. L. Sun, S. Gao, and G. Su, *Journal of Materials Chemistry* **2005**, *15*, 4209-4214.
- 40 T. Mirkovic, M. A. Hines, P. S. Nair, and G. D. Scholes, *Chemistry of Materials* **2005**, *17*, 3451-3456.
- 41 T. Kataoka, Y. Tsukahara, Y. Hasegawa, and Y. Wada, *Chemical Communications* **2005**, 6038-6040.
- 42 Y. Hasegawa, M. Afzaal, P. O'Brien, Y. Wada, and S. Yanagida, *Chemical Communications* **2005**, 242-243.
- 43 M. D. Regulacio, K. Bussmann, B. Lewis, and S. L. Stoll, *Journal of the American Chemical Society* **2006**, *128*, 11173-11179.
- 44 F. Zhao, H.-L. Sun, G. Su, and S. Gao, *Small* **2006**, *2*, 244-248.
- 45 M. L. Redígolo, D. S. Koktysh, S. J. Rosenthal, and J. H. Dickerson, *Physica Status Solidi C* **2007**, *4*, 406-408.
- 46 Y. Hasegawa, T. Adachi, A. Tanaka, M. Afzaal, P. O'Brien, T. Doi, Y. Hinatsu, K. Fujita, K. Tanaka, and T. Kawai, *Journal of the American Chemical Society*

- 2008**, *130*, 5710-5715.
- 47 A. S. Pereira, P. Rauwel, M. S. Reis, N. J. Oliveira Silva, A. Barros-Timmons, and T. Trindade, *Journal of Materials Chemistry* **2008**, *18*, 4572-4578.
- 48 M. D. Regulacio, S. Kar, E. Zuniga, G. Wang, N. R. Dollahon, G. T. Yee, and S. L. Stoll, *Chemistry of Materials* **2008**, *20*, 3368-3376.
- 49 V. M. Huxter, T. Mirkovic, P. S. Nair, and G. D. Scholes, *Advanced Materials* **2008**, *20*, 2439-2443.
- 50 R. S. Selinsky, D. J. Keavney, M. J. Bierman, and S. Jin, *Applied Physics Letters* **2009**, *95*, 202501-202503.
- 51 S. Kar, W. L. Boncher, D. Olszewski, N. Dollahon, R. Ash, and S. L. Stoll, *Journal of the American Chemical Society* **2010**, *132*, 13960-13962.
- 52 R. S. Selinsky, J. H. Han, E. A. Morales Pérez, I. A. Guzei, and S. Jin, *Journal of the American Chemical Society* **2010**, *132*, 15997-16005.
- 53 W. He and J. H. Dickerson, *Applied Physics Letters* **2011**, *98*, 081914.
- 54 S. Kar, N. R. Dollahon, and S. L. Stoll, *Journal of Solid State Chemistry* **2011**, *184*, 1324-1327.
- 55 Y. Hasegawa, *Chemistry Letters* **2013**, *42*, 2-7.
- 56 Y. Hasegawa, M. Kumagai, A. Kawashima, T. Nakanishi, K. Fujita, K. Tanaka, and K. Fushimi, *Journal of Physical Chemistry C* **2012**, *116*, 19590-19596.
- 57 A. V. Zayats, I. I. Smolyaninov, and A. A. Maradudin, *Physics Reports* **2005**, *408*, 131-314.
- 58 O. Kulakovich, N. Strekal, A. Yaroshevich, S. Maskevich, S. Gaponenko, I.

- Nabiev, U. Woggon, and M. Artemyev, *Nano Letters* **2002**, *2*, 1449-1452.
- 59 E. Katz and I. Willner, *Angewandte Chemie International Edition* **2004**, *43*, 6042-6108.
- 60 J. Lee, A. O. Govorov, J. Dulka, and N. A. Kotov, *Nano Letters* **2004**, *4*, 2323-2330.
- 61 Y. Tian and T. Tatsuma, *Journal of the American Chemical Society* **2005**, *127*, 7632-7637.
- 62 Y. Li, Q. Zhang, A. V. Nurmikko, and S. Sun, *Nano Letters* **2005**, *5*, 1689-1692.
- 63 R. Fujikawa, A. V. Baryshev, J. Kim, H. Uchida, and M. Inoue, *Journal of Applied Physics* **2008**, *103*, 07D301-303.
- 64 S. Ozaki, H. Kura, H. Maki, and T. Sato, *Journal of Applied Physics* **2009**, *106*, 123530-123533.
- 65 P. K. Jain, Y. Xiao, R. Walsworth, and A. E. Cohen, *Nano Letters* **2009**, *9*, 1644-1650.
- 66 L. Wang, C. s. Clavero, Z. Huba, K. J. Carroll, E. E. Carpenter, D. Gu, and R. A. Lukaszew, *Nano Letters* **2011**, *11*, 1237-1240.
- 67 P. Charoonniyomporn, T. Thongpanchang, S. Witayakran, Y. Thebtaranonth, K. E. S. Phillips, and T. J. Katz, *Tetrahedron Letters* **2004**, *45*, 457-459.
- 68 B. N. J. Persson, *Surface Science* **1993**, *281*, 153-162.
- 69 J. R. Lakowicz, *Analytical Biochemistry* **2005**, *337*, 171-194.
- 70 V. Lesnyak, A. Wolf, A. Dubavik, L. Borchardt, S. V. Voitekhovich, N. Gaponik, S. Kaskel, and A. Eychmuller, *Journal of the American Chemical*

- Society* **2011**, *133*, 13413-13420.
- 71 S. L. McCall, P. M. Platzman, and P. A. Wolff, *Physics Letters A* **1980**, *77*, 381-383.
- 72 G. W. Ford and W. H. Weber, *Physics Reports* **1984**, *113*, 195-287.
- 73 J. R. Lakowicz, *Analytical Biochemistry* **2001**, *298*, 1-24.
- 74 T. L. Jennings, M. P. Singh, and G. F. Strouse, *Journal of the American Chemical Society* **2006**, *128*, 5462-5467.
- 75 S. Link and M. A. El-Sayed, *Journal of Physical Chemistry B* **1999**, *103*, 4212-4217.
- 76 Y. Hasegawa, Y. Wada, and S. Yanagida, *Journal of Alloys and Compounds* **2006**, *408-412*, 207-211.

Chapter 4

Photo-switchable Faraday Effect in EuS-Au Nanosystems

4.1 Introduction

In Chapter 3, the author prepared EuS nanocrystals attached to Au nanoparticles using dithiol joint molecules (EuS-Au nanosystems). Au nanoparticles are known to exhibit localized surface plasmon resonance (LSPR), which leads to unique and unusual photophysical enhancements such as enhanced luminescence and photo-catalytic properties^[1-5]. In addition, the author observed enhancement of the Faraday rotation angle and an increase in the effective signals on the electron spin resonance (ESR) under irradiation with visible light. The enhanced Faraday effects of EuS-Au nanosystems under visible light irradiation are expected to open up new optical devices that use optical switching materials for fiber-optic communication systems.

In this chapter, the photo-switching Faraday effects of EuS-Au nanosystems are demonstrated (Figure 4-1). EuS nanocrystals and Au nanoparticles were synthesized

via thermal reduction of the following single-source precursors; tetraphenylphosphonium tetrakis(diethyldithiocarbamate) europium(III) ((PPh₄)[Eu(S₂CEt₂)₄]) and chloro(triphenylphosphine) gold(I) (PPh₃AuCl), respectively. The EuS-Au nanosystems were prepared via ligand exchange reaction of 1,10-decanedithiol. The prepared EuS-Au nanosystems were characterized using TEM and XRD. The Faraday effects of toluene solution containing EuS-Au nanosystems were estimated by performing magnetic circular dichroism (MCD) measurements using a system with an attached visible light irradiation system (> 440 nm). The photo-switchable Faraday effects of EuS-Au nanosystems, which might have applications in optical devices, were demonstrated.

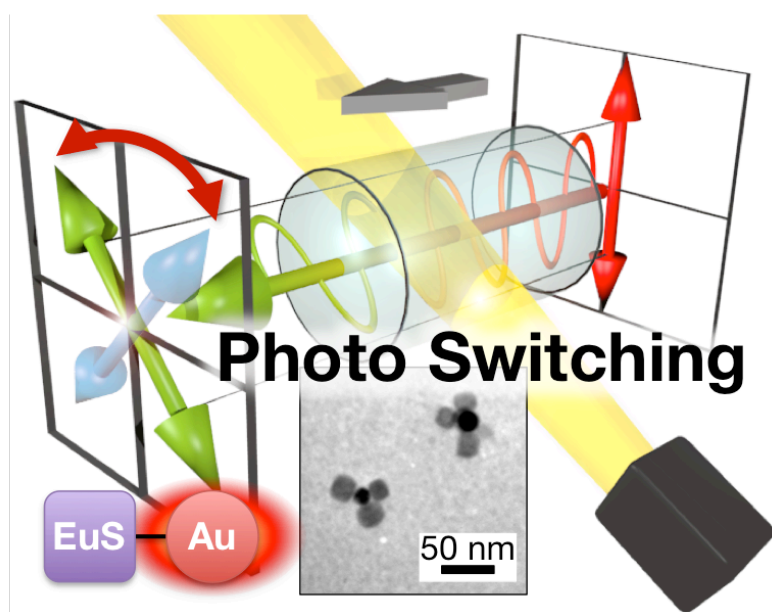


Figure 4-1. Illustration of photo-switch and TEM image of EuS-Au nanosystems.

4.2 Experiments

4.2.1 Materials

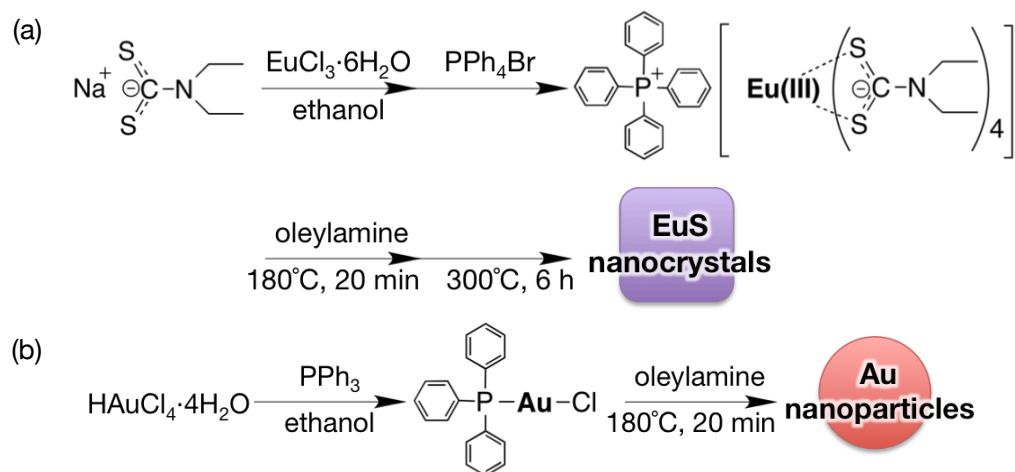
Europium(III) chloride hexahydrate ($\text{EuCl}_3 \cdot 6\text{H}_2\text{O}$), sodium *N,N*-diethyl-dithiocarbamate trihydrate ($\text{Na}(\text{S}_2\text{CNET}_2) \cdot 3\text{H}_2\text{O}$) and 1-dodecanethiol were purchased from Kanto Chemical Co. Inc. Tetrachloroaurate(III) tetrahydrate ($\text{HAuCl}_4 \cdot 4\text{H}_2\text{O}$), tetraphenylphosphonium bromide (BrPPh_4) and triphenylphosphine (PPh_3) were purchased from Wako Pure Chemical Industry, Ltd. Oleylamine and 1,10-decanedithiol (DDT) were obtained from Tokyo Chemical Industry Co., Ltd. All other chemicals and solvents were reagent grade and were used without further purification.

4.2.2 Apparatus

Infrared spectra were recorded on a JASCO FT/IR-350 spectrometer. ^1H NMR data were measured by a JEOL AL-300 (300 MHz). ^1H NMR chemical shifts were determined by using tetramethylsilane (TMS) as an internal standard. Elemental analyses were performed with a Yanaco CHN corder MT-6. XRD patterns were characterized by a Rigaku SmartLab X-ray diffractometer. High-resolution images of the EuS-Au nanosystems were obtained with TEM, JEOL 2010 FASTEM (200 kV). UV-vis absorption spectra were measured on a JASCO V-570 spectrophotometer at room temperature.

4.2.3 Syntheses

Syntheses of EuS and Au Nanocrystals:



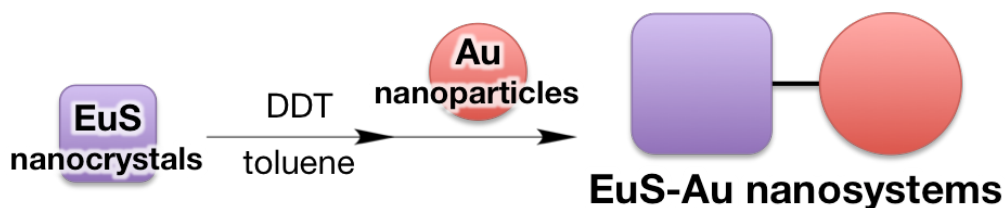
Scheme 4-1. Reaction schemes of (a) cube-shaped EuS nanocrystals and (b) sphere-shaped Au nanoparticles.

Single source precursors, tetraphenylphosphonium tetrakis(diethyldithio-carbamate)europium(III) complex ((PPh₄)[Eu(S₂CNEt₂)₄]) and chloro(triphenylphosphine) gold(I) complex (PPh₃AuCl), were synthesized as Chapter 2 and 3. Monodisperse EuS nanocrystals and Au nanoparticles were synthesized by the thermal reaction of the (PPh₄)[Eu(S₂CNEt₂)₄] and PPh₃AuCl in oleylamine at 300°C for 6 h and 180°C for 30 min, respectively, under a N₂ atmosphere. The precipitation was added to solvent (toluene (EuS) and THF (Au), 10 mL) and centrifuged at 4000 rpm for 15 min, and oleylamine capped EuS nanocrystals and Au nanoparticles were obtained, respectively.

Ligand Exchange Reaction:

Prepared EuS nanocrystals suspended in toluene solution (20 mL) with EuS nanocrystals (0.08 g) was added into toluene (5 mL) with DDT (0.1 mL). After 5 min, the toluene solution including EuS-DDT was added into excess amount of 1-dodecanethiol, and the liquid of dithiol capped EuS nanocrystals (EuS-DDT) was obtained.

Synthesis of EuS-Au Nanosystems:



Scheme 4-2. Reaction scheme of EuS-Au nanosystems.

The EuS-Au nanosystems were formed by adding the solution of Au nanoparticles (0.05 g) in THF (20 mL) to the solution of EuS-DDT in toluene. The mixture was stirred for 30 min at room temperature. The solution was added to 1-dodecanethiol (1 mL) and stirred for 1 h. The resulting solution of EuS-Au nanosystems in toluene was obtained.

4.2.4 MCD measurements

MCD measurements were performed using a JASCO J-1500 spectrodichromometer equipped with a JASCO permanent magnet (0.47 T). For MCD

measurements under light irradiation, a metal halide lamp (> 440 nm, Moritex, MHF100L II) was employed as the excitation light source. The schematic view of experimental setup is shown in Figure 4-2.

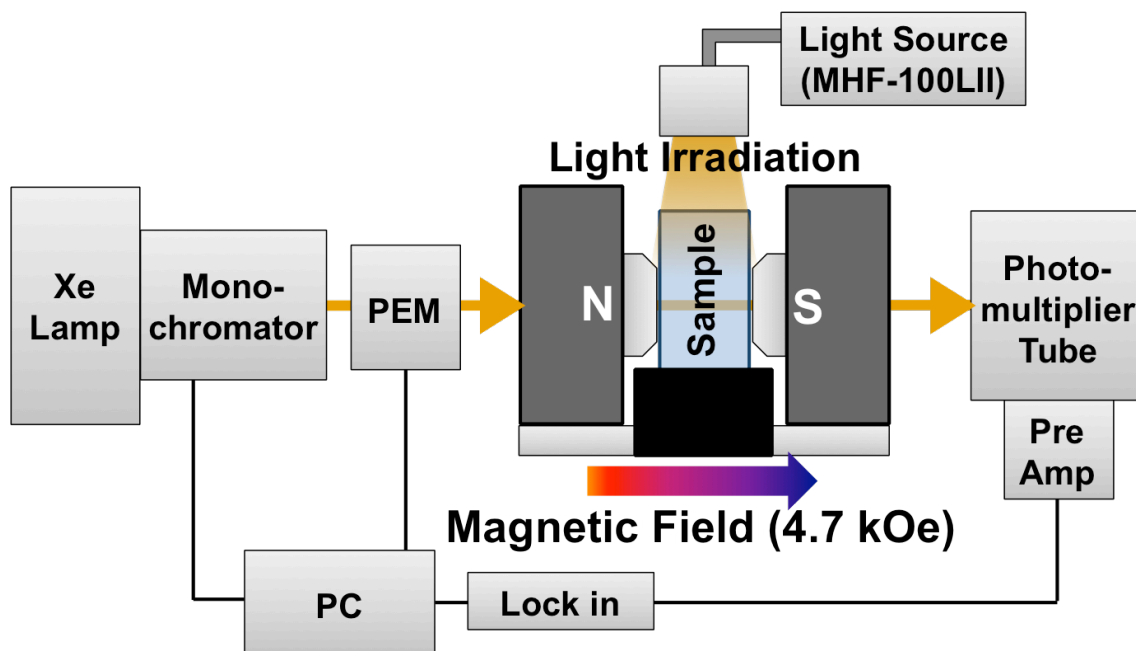


Figure 4-2. Schematic view of experimental setup for MCD measurements under light irradiation.

4.3 Results and Discussion

4.3.1 Preparation of EuS-Au Nanosystems

Monodisperse EuS nanocrystals and Au nanoparticles were respectively synthesized by the thermal reaction of Eu(III) dithiocarbamate complex ((PPh₄)[Eu(S₂CNEt₂)₄]) and Au(I) triphenyl complex (PPh₃AuCl) as single source precursors in oleylamine (as same as Chapter 3). The prepared EuS nanocrystals were connected with Au nanoparticles using dithiol joint molecules (DDT), resulting in the formation of EuS-Au nanosystems. The XRD patterns of the EuS nanocrystals, Au nanoparticles, and EuS-Au nanosystems are shown in Figure 4-3. The diffraction peaks at $2\theta = 25.8, 29.9, 42.8, 50.6, 53.1, 62.2, 68.5,$ and 70.5 degree were assigned to the (111), (200), (220), (311), (222), (400), (331), and (420) planes, respectively, of NaCl type EuS (ICDD 26-1419). The diffraction peaks at $2\theta = 38.2, 44.4, 64.7,$ and 78.5 degree were assigned to the (111), (200), (220), and (311) planes, respectively, of face-centered-cubic (fcc) type Au (ICDD 4-0784). The author evaluated FWHM of the $2\theta = 25.8$ and 38.2 degree peaks, which correspond to Bragg diffraction from the EuS (200) and Au (111) planes, respectively. The FWHM of EuS and Au nanocrystals in the EuS-Au nanosystems were 0.49 and 0.50 degree, respectively, although the FWHM of the previous EuS and Au nanocrystals were found to be 0.58 and 0.67 degree, respectively. Smaller EuS-Au nanosystems might be removed by centrifugation for purification of EuS-Au nanosystems. The EuS and Au crystallite sizes calculated from XRD data using the Scherer equation were 16.6 and 16.8 nm, respectively.

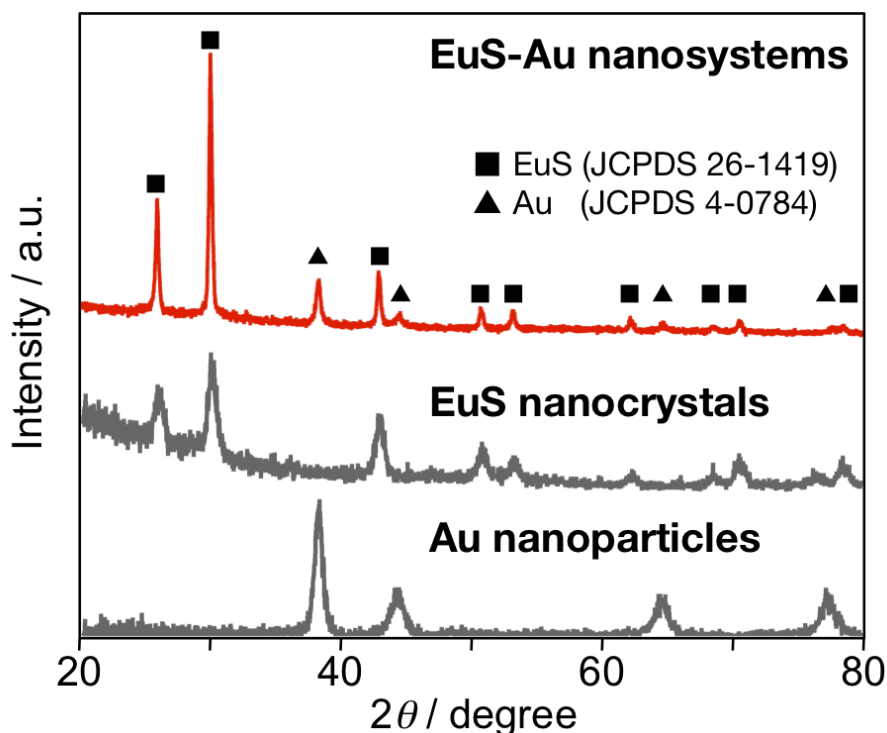


Figure 4-3. XRD patterns of EuS-Au nanosystems, EuS nanocrystals, and Au nanoparticles. Square and circle in XRD pattern are based on the JCPDS data for EuS and Au crystals, respectively.

The author observed cubic EuS nanocrystals and spherical Au nanoparticles using TEM (Figure 4-4a and b). The author estimated the average crystal grain sizes of EuS and Au nanocrystals to be 19.5 and 18.5 nm, respectively, from TEM images. The TEM image of the EuS-Au nanosystem is shown in Figure 4-4c. The image indicates the formation of EuS-Au nanosystems composed of cubic EuS nanocrystals and spherical Au nanoparticles. The spherical Au nanoparticles (black circles) were surrounded with cubic EuS nanocrystals. The sizes of the EuS nanocrystals (approximately 19.5 nm) and the Au nanoparticles (approximately 18.5 nm) were similar to values estimated by performing XRD measurements.

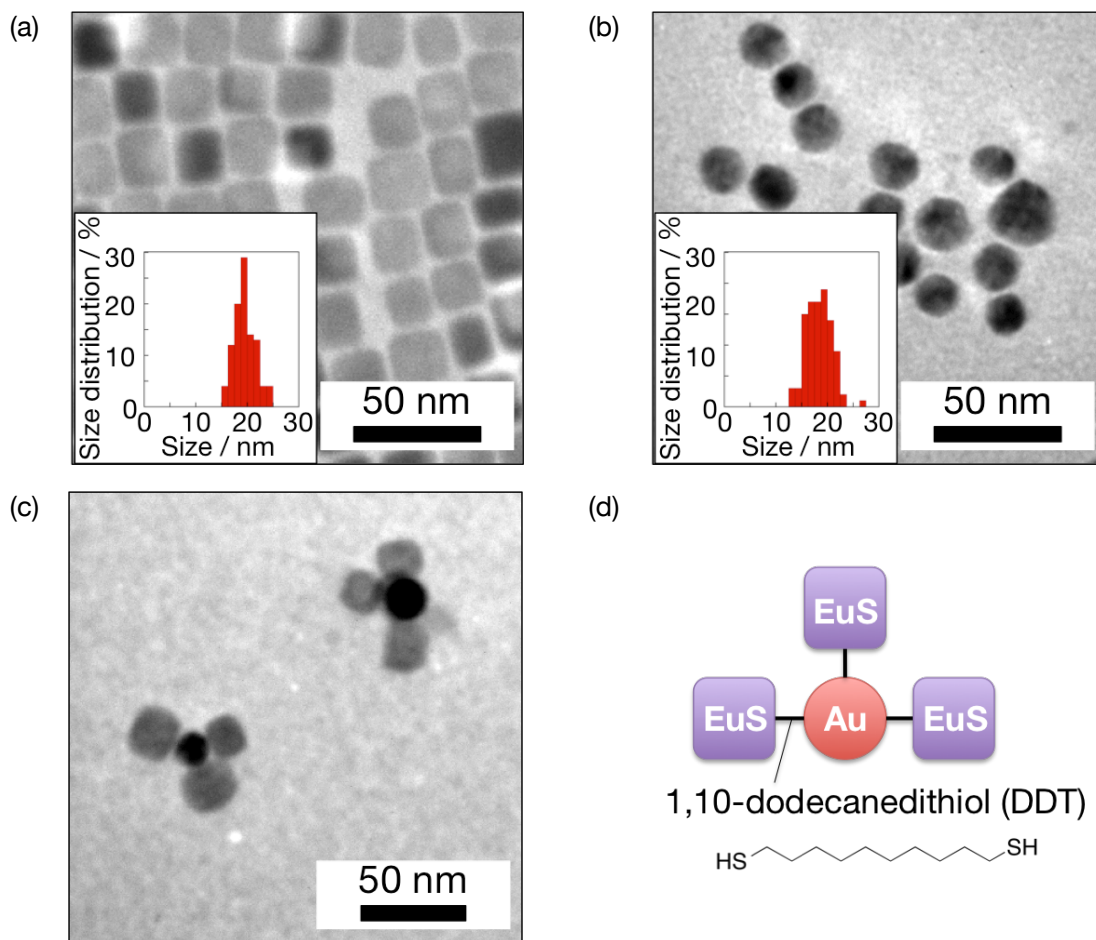


Figure 4-4. TEM images of (a) EuS nanocrystals, (b) Au nanoparticles, and (c) EuS-Au nanosystems. (d) Illustration of the EuS-Au nanosystems linked with 1,10-dodecanedithiol (DDT). Inset of Figure 4-4a and b show the size distributions of EuS and Au nanocrystals, respectively.

4.3.2 Photophysical Properties of EuS-Au Nanosystems

The prepared EuS-Au nanosystems were dispersed homogeneously in toluene. The absorption spectra of the toluene solution containing the EuS nanocrystals and the EuS-Au nanosystems, and that of the THF solution containing the Au nanoparticles are shown in Figure 4-5a and b, respectively. The broad absorption band at 510 nm was assigned to the $4f-5d$ transition in the EuS nanocrystals. Broadening of absorbance of the EuS-Au nanosystems was observed at around 600 nm, although the LSPR band of only Au nanoparticles is shown at around 535 nm (Figure 4-5b). The broad absorbance band of EuS-Au nanosystems might have been caused by the dielectric surroundings of the Au nanoparticles^[6-8]. The red shift of the LSPR band implies that the Au nanoparticles were directly linked to EuS nanocrystals in a highly dielectric environment. Thus, the author successfully synthesized DDT-linked EuS-Au nanosystems. Additionally, the EuS nanocrystals can potentially be affected by the LSPR of Au nanoparticles between 530 and 800 nm.

Under visible light irradiation, the author observed a drastic change in the absorption band of the EuS-Au nanosystems (Figure 4-5b). The absorption intensity changed under visible light and dark at around 600 nm, and this change was repeatable and reversible. In contrast, a drastic change in the absorption band of the toluene solution containing EuS nanocrystals was not observed. The drastic change in the absorption band change of the EuS-Au nanosystems at around 600 nm might be ascribed to LSPR enhancement and a decrease in the ground state density of EuS-Au nanosystems under irradiation.

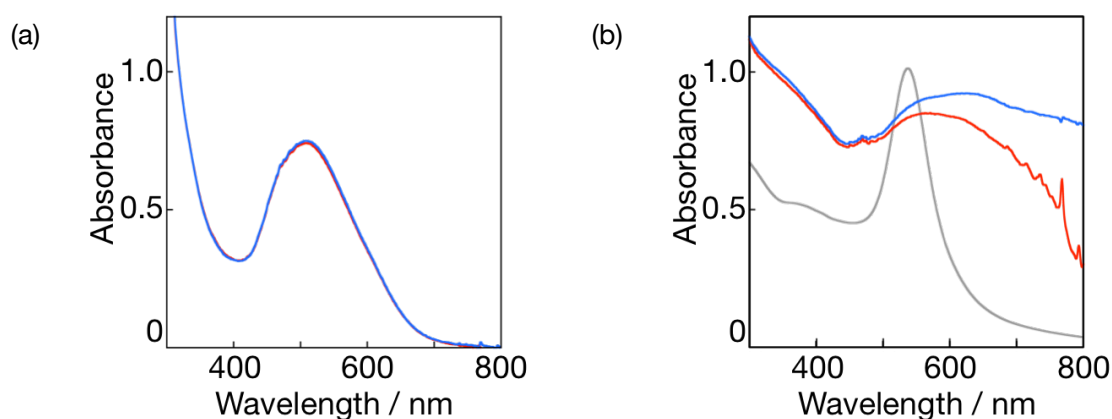


Figure 4-5. UV-Vis absorption spectra of toluene solution containing (a) EuS nanocrystals and (b) EuS-Au nanosystems under dark (blue line) and light irradiation (red line) with an external magnetic field of 0.47 T. Gray line in Figure 4-5b is UV-Vis absorption spectrum of THF solution containing Au nanoparticles.

The MCD spectra of EuS nanocrystals and EuS-Au nanosystems under irradiation and in dark are shown in Figure 4-6a and b. To estimate the ratio between MCD spectra under dark and light irradiation, the author considered that the MCD spectra should be normalized by the peak values of the dark condition. The EuS-Au nanosystems exhibited positive and negative rotation signals, as did the EuS nanocrystals. This indicates that the aforementioned signals can possibly be ascribed to the excited state degeneracy of Eu ions, which is assigned to the $4f-5d$ transition in the EuS nanocrystals. The rotation wavelengths of the EuS-Au nanosystems (positive and negative rotation signal at around 670 and 550 nm, respectively) are longer than those of EuS (610 and 510 nm). Additionally, the ratio of negative to positive rotation angles of the EuS-Au nanosystems (1.04) is about twice as large as that of the EuS nanocrystals (0.56). These results indicate that the Au nanoparticles affect the excited and ground states of EuS nanocrystals, resulting in a changed MCD spectrum^[9].

Under irradiation, effective changes in the MCD spectrum of the EuS-Au nanosystems in toluene solution were observed at around 670 and 550 nm (maximum positive and negative rotation wavelength), whereas the MCD spectrum of the EuS nanocrystals in toluene solution showed a slight change at around 610 nm.

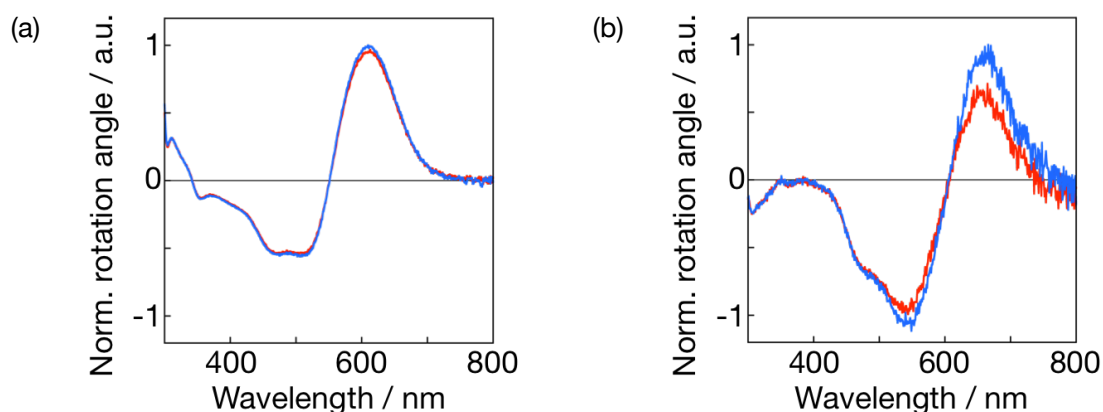


Figure 4-6. MCD spectra of toluene solution containing (a) EuS nanocrystals and (b) EuS-Au nanosystems under dark (blue line) and light irradiation (red line) with an external magnetic field of 0.47 T.

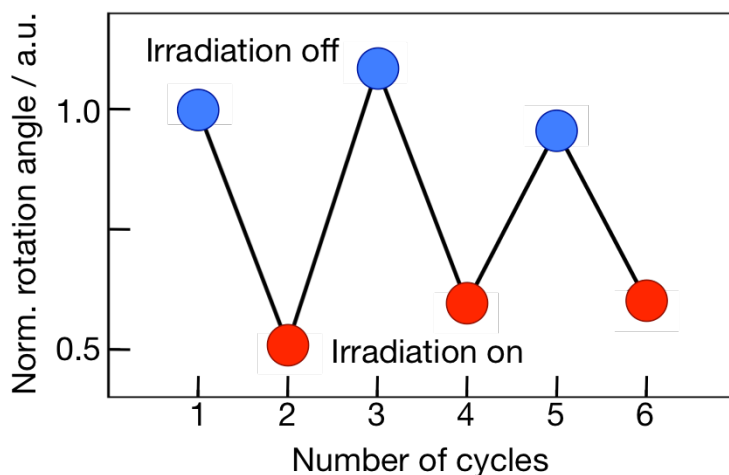


Figure 4-7. The reversible changes in MCD spectra of EuS-Au nanosystems at 670 nm with the alternative irradiation cycles of visible light (> 440 nm) and dark.

The effective reversible changes in the MCD spectra at 670 nm under the alternative irradiation cycles of visible light (> 440 nm) and dark are shown in Figure 4-7 as well. From these alternative irradiation experiments, reversible change in the rotation angles of the EuS-Au nanosystems may not have been caused by aggregation or decomposition of the EuS-Au nanosystems. In addition, the author estimated the rate of decrease in the rotation angle of the EuS-Au nanosystems using Equation (4-1).

$$\Delta\theta = (\theta_{\text{dark}}/A_{\text{dark}} - \theta_{\text{light}}/A_{\text{light}})/(\theta_{\text{dark}}/A_{\text{dark}}) \quad (4-1)$$

where θ and A are the rotation angle of the MCD spectra and absorbance at maximum positive rotation wavelength (670 nm), respectively. To estimate Faraday rotation without any effect on the absorption band, the author calculated the rate of decrease using equation (1). The rate of decrease ($\Delta\theta$) of the EuS-Au nanosystems was found to be 38.0%, although the relationship between the rates of decrease in absorbance and MCD intensity might be linear^[9]. This result indicates that the rate of decrease of the rotation angle of the EuS-Au nanosystems at 670 nm is larger than rate of decrease in absorbance. The author considered that the effective change in the MCD spectra of EuS-Au nanosystems would be dominated not only by a drastic change in absorption band due to the enhanced LSPR of Au nanoparticles but also by specific interactions between EuS and Au in the nanosystem under irradiation. There are mainly two specific interactions between EuS nanocrystals and Au nanoparticles, the mixing of electronic state between EuS and Au nanocrystals and the influence of LSPR on EuS nanocrystals.

In particular, the LSPR of Au nanoparticles might induce a change in absorption of the EuS nanocrystals. Although it is difficult to determine the exact origin of the phenomenon, LSPR is one of the origins inducing the weak MCD intensity^[9].

4.4 Conclusions

In this chapter, novel photo-switching Faraday effects in the EuS-Au nanosystems were successfully observed. The drastic change in the absorption band may be related to the enhanced LSPR of Au and specific interactions between Au and EuS in the nanosystems under irradiation. The photo-switchable EuS-Au nanosystems with Faraday effects are expected to be used as novel photo-switching materials in advanced fiber-optic communication systems.

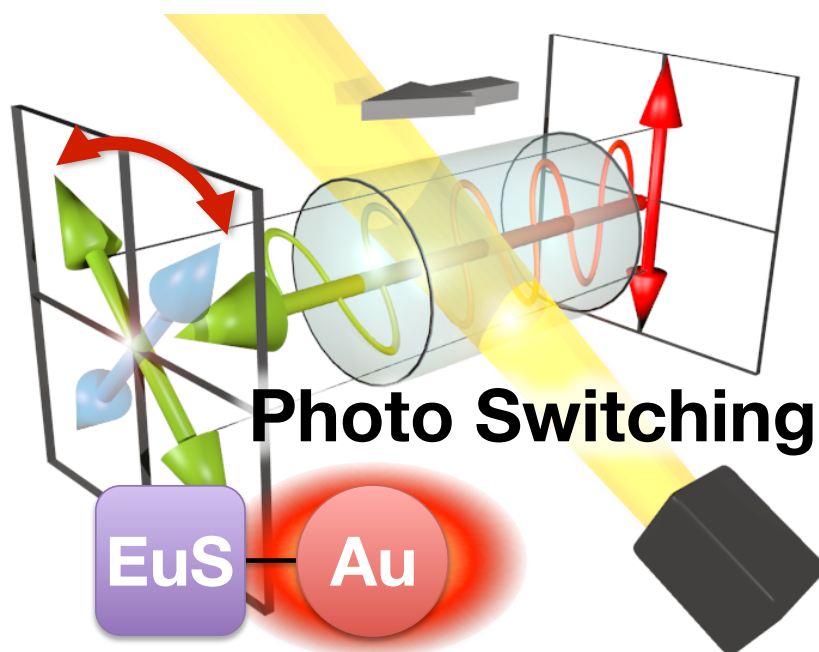


Figure 4-8. Illustration of photo-switching Faraday effects in EuS-Au nanosystems.

4.5 References

- 1 O. Kulakovich, N. Strekal, A. Yaroshevich, S. Maskevich, S. Gaponenko, I. Nabiev, U. Woggon, and M. Artemyev, *Nano Letters* **2002**, *2*, 1449-1452.
- 2 E. Katz and I. Willner, *Angewandte Chemie International Edition* **2004**, *43*, 6042-6108.
- 3 J. Lee, A. O. Govorov, J. Dulka, and N. A. Kotov, *Nano Letters* **2004**, *4*, 2323-2330.
- 4 Y. Tian and T. Tatsuma, *Journal of the American Chemical Society* **2005**, *127*, 7632-7637.
- 5 A. V. Zayats, I. I. Smolyaninov, and A. A. Maradudin, *Physics Reports* **2005**, *408*, 131-314.
- 6 B. N. J. Persson, *Surface Science* **1993**, *281*, 153-162.
- 7 J. R. Lakowicz, *Analytical Biochemistry* **2005**, *337*, 171-194.
- 8 V. Lesnyak, A. Wolf, A. Dubavik, L. Borchardt, S. V. Voitekhovich, N. Gaponik, S. Kaskel, and A. Eychmuller, *Journal of the American Chemical Society* **2011**, *133*, 13413-13420.
- 9 J. Larrabee, G. Schenk, N. Mitić, and M. Riley, *European Biophysics Journal* **2015**, *44*, 393-415.

Chapter 5

Terbium Oxide, Fluoride, and Oxyfluoride Nanocrystals with Magneto-optical Properties

5.1 Introduction

Optical isolators for high-speed and highly accurate optical information technology are promising devices that allow transmission of light in only one direction^[1-3]. The optical communication performance of an optical isolator is based on the Faraday effect; the rotation of the plane of polarized light is linearly proportional to the component of magnetic field in the direction of propagation. Practical application of optical isolators has led to considerable attention being focused on the preparation and properties of magnetic semiconductor nanomaterials. Currently, various types of structured magnetic materials have been prepared^[4]. The preparation of II–VI or III–V semiconductor nanoparticles with magnetic dopants has been studied as well^[5-9]. Wang

and co-workers reported on the $Zn_{0.93}Mn_{0.07}S$ cluster, a dilute magnetic semiconductor^[5]. Rajamanickam and co-workers reported the synthesis and magneto-optical properties of (Li, Mn) co-doped ZnO nanoparticles^[9]. EuX ($X = O, S, Se$ and Te) nanocrystals have been also studied intensively due to their $4f-5d$ electronic transitions and spin configuration, which lead to strong Faraday effects in visible region^[10-15].

In this chapter, the Faraday effects of terbium (Tb) nanocrystals are discussed. The effective number of Bohr magnetons of Tb(III) ions is 9.72, higher than those of other paramagnetic metal ions (Eu(II): $\mu_{\text{eff}} = 7.94 \mu_B$, Mn(II): $\mu_{\text{eff}} = 5.92 \mu_B$, and Fe(II): $\mu_{\text{eff}} = 4.90 \mu_B$). This leads to enhanced Faraday effects and the development of optical isolators in the visible region. Watarai and co-workers reported the Faraday effect for lanthanide(III) chloride ($Ln(III)Cl_3$) in aqueous solution in the visible region between 410 and 640 nm^[16]. Zou and co-workers reported the preparation and magneto-optical properties of terbium-doped borate glass^[17]. Li and co-workers reported on high-terbium-content apatite crystals, $Tb_5Si_2BO_{13}$ and $Tb_{4.66}Si_3O_{13}$, which show strong Faraday effects upon an increase in the concentration of Tb(III) ions^[18]. Various types of Tb inorganic glass materials have been studied as well^[19,20].

Recently, Nakanishi and co-workers reported that nonanuclear Tb(III) clusters with lanthanide–oxygen lattice structures show strong Faraday rotation under magnetic fields^[21]. The enhanced Faraday effect is based on the specific magnetic exchange interaction between Tb ions in the Tb-O lattice structures, and these interactions depend on the geometric, electronic, and spin structures. Preparation of novel nano-materials composed of Tb lattice structures, TbX nanocrystals, is expected to open up a frontier

between inorganic nanomaterials and photonic science. Here, the author reports on TbX nanocrystals, terbium oxides (Tb_2O_3), terbium fluorides (TbF_3), and terbium oxyfluorides (TbOF). The Tb_2O_3 , TbF_3 , and TbOF nanocrystals were synthesized by the thermal decomposition of the following single-source precursors; tris(acetylacetonato)-dimethanolterbium(III) ($[Tb(acac)_3(CH_3OH)_2]$), tris(acetylacetonato)bis(triphenylphosphineoxide)terbium(III) ($[Tb(acac)_3(tppo)_2]$), tris(hexafluoro-acetylacetonato)-dimethanolterbium(III) ($[Tb(hfa)_3(CH_3OH)_2]$) and tris(hexafluoroacetylacetonato)bis(triphenylphosphineoxide)terbium(III) ($[Tb(hfa)_3(tppo)_2]$), respectively. Decomposition temperatures of Tb(III) complexes for preparation of TbX nanocrystals were estimated by using thermogravimetric (TG) analysis. The prepared TbX nanocrystals were characterized by using XRD, TEM, EDS, X-ray photoelectron spectroscopy (XPS), and ESR. Polymer thin films containing the TbX nanocrystals (matrix: PMMA) were evaluated for estimating the Faraday effect under a magnetic field (15000 Oe). The author successfully observed high transparency and remarkable Faraday rotation of the polymer thin films with TbOF and TbF_3 nanocrystals. In this chapter, the syntheses and magneto-optical properties of TbX nanocrystals are demonstrated.

5.2 Experiments

5.2.1 Materials

Terbium(III) acetate tetrahydrate ($\text{Tb}(\text{CH}_3\text{CO}_2)_3 \cdot 4\text{H}_2\text{O}$) was purchased from Wako Pure Chemical Industry, Ltd. Acetylacetone (acac, $\text{CH}_3\text{C}(\text{O})\text{CH}_2\text{C}(\text{O})\text{CH}_3$), hexafluoroacetylacetone (hfa, $\text{CF}_3\text{C}(\text{O})\text{CH}_2\text{C}(\text{O})\text{CF}_3$), triphenylphosphine oxide (tppo, Ph_3PO) and oleylamine were obtained from Tokyo Chemical Industry Co., Ltd. All other chemicals and solvents were reagent grade and were used without further purification.

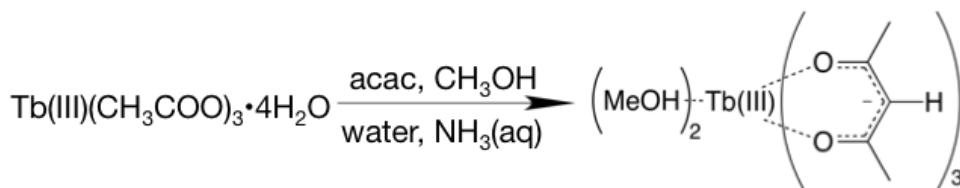
5.2.2 Apparatus

FT-IR measurements performed at room temperature using a ThermoNicolet Avatar 320 FTIR spectrometer. Mass spectra were measured using a JEOL JMS-T100LP. Elemental analyses were performed on a J-Science Lab JM 10 Micro Corder and an Exeter Analytical CE440. TG-DTA were measured using Seiko Instruments Inc. EXSTAR 6000 (TG-DTA 6300) at heating rate of 1°C min^{-1} . XRD patterns were characterized by a Rigaku SmartLab X-ray diffractometer using Cu Ka radiation source ($\lambda = 0.15418 \text{ nm}$). X-ray photoelectron spectroscopy (XPS) were performed with a JPS-9200 using unmonochromatized Al Ka X-ray. High-resolution images of TbX nanocrystals were obtained with a TEM, JEOL 2010 FASTEM (200 kV). UV-vis absorption spectra were measured on a JASCO V-570 spectrophotometer at room temperature.

5.2.3 Syntheses

Synthesis of *tris(acetylacetonato)dimethanolterbium(III)*

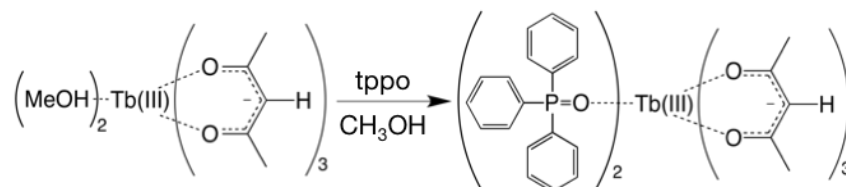
([Tb(acac)₃(CH₃OH)₂):



Scheme 5-1. Reaction scheme of [Tb(acac)₃(CH₃OH)₂].

Terbium(III) acetate tetrahydrate (2.61 g, 7.4 mmol) was dissolved in distilled water (40 mL) by stirring. Acetylacetonone (1.94 mL, 23 mmol) was added dropwise to the above solution. The pH value of this solution was adjusted at pH 7 by adding NH₃ aqueous solution. The mixture produced a white precipitate after stirring for 3 h. The resulting precipitate was separated by filtration and washed 2 times with distilled water. Reprecipitation from methanol gave a white precipitate of [Tb(acac)₃(CH₃OH)₂]. IR (ATR): $\tilde{\nu} = 1650$ (C=O), 1390 (–CH₃), 1020 (–CH₃), 920 (C–CH₃) cm^{–1}; ESI-MS: *m/z*: calcd for C₁₂H₂₂O₆Tb [M–(acac)]⁺: 421.07; found: 421.10; elemental analysis calcd (%) for C₁₇H₂₉O₈Tb: C 39.24, H 5.62 N 0.00; found: C 39.03, H 5.44, N 0.00.

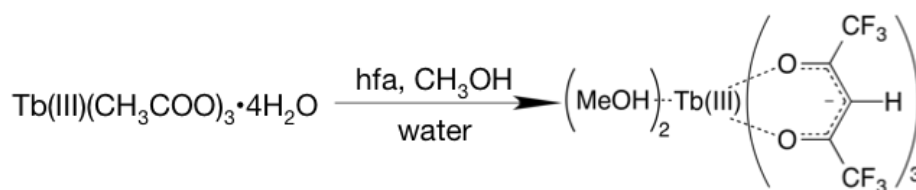
Synthesis of *tris*(acetylacetonato)*bis*(triphenylphosphine oxide)terbium(III) ([Tb(acac)₃(tppo)₂):



Scheme 5-2. Reaction scheme of [Tb(acac)₃(tppo)₂].

Methanol solution (40 mL) containing [Tb(acac)₃(CH₃OH)₂] (0.52 g, 1.0 mmol) and triphenylphosphine oxide (tppo) (0.56 g, 2.0 mmol) was refluxed under stirring for 3 h. The reaction mixture was concentrated using a rotary evaporator. Reprecipitation by addition of excess hexane produced crude crystals, which were washed in toluene several times. Recrystallization from hot methanol gave green translucent crystals of [Tb(acac)₃(tppo)₂]. IR (ATR): $\tilde{\nu}$ = 1650 (C=O), 1125 (P=O), 920 (C-CH₃) cm⁻¹; elemental analysis calcd (%) for C₅₁H₅₁O₈P₂Tb: C 60.48, H 5.08, N 0.00; found: C 60.52, H 4.86, N 0.00.

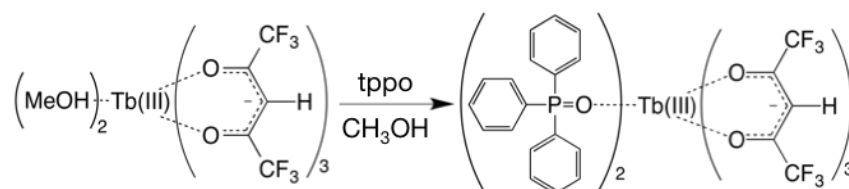
Synthesis of *tris*(hexafluoroacetylacetonato)*dimethanol*terbium(III) ([Tb(hfa)₃(CH₃OH)₂):



Scheme 5-3. Reaction scheme of [Tb(hfa)₃(CH₃OH)₂].

Terbium(III) acetate tetrahydrate (5.00 g, 12 mmol) was dissolved in distilled water (40 mL) by stirring. Hexafluoroacetylacetone (7.78 g, 37 mmol) was added dropwise to the above solution. The mixture produced a white green precipitate after stirring for 3 h. The resulting precipitate was separated by filtration and washed 2 times with distilled water. Reprecipitation from methanol gave a white precipitate of $[\text{Tb}(\text{hfa})_3(\text{CH}_3\text{OH})_2]$. IR (ATR): $\tilde{\nu} = 1650$ (C=O), 1255–1141 (C–F) cm^{-1} ; ESI-MS: m/z : calcd for $\text{C}_{12}\text{H}_{10}\text{F}_{12}\text{O}_6\text{Tb}$ $[\text{M}-(\text{hfa})]^+$: 636.95; found: 637.01; elemental analysis calcd (%) for $\text{C}_{17}\text{H}_{11}\text{F}_{18}\text{O}_8\text{Tb}$: C 24.19, H 1.31, N 0.00; found: C 23.91, H 1.36, N 0.00.

Synthesis of *tris*(hexafluoroacetylacetonato)bis(triphenylphosphine oxide)terbium(III) ($[\text{Tb}(\text{hfa})_3(\text{tppo})_2]$):



Scheme 5-4. Reaction scheme of $[\text{Tb}(\text{hfa})_3(\text{tppo})_2]$.

Methanol solution (40 mL) containing $[\text{Tb}(\text{hfa})_3(\text{CH}_3\text{OH})_2]$ (0.84 g, 1.0 mmol) and triphenylphosphine oxide (tppo) (0.56 g, 2.0 mmol) was refluxed under stirring for 3 h. The reaction mixture was concentrated using a rotary evaporator. Reprecipitation by addition of excess hexane produced crude crystals, which were washed in toluene several times. Recrystallization from hot methanol gave green

translucent crystals of $[\text{Tb}(\text{hfa})_3(\text{tppo})_2]$. IR (ATR): $\tilde{\nu} = 1650$ (C=O), 1255–1150 (C–F), 1125 (P=O) cm^{-1} ; elemental analysis calcd (%) for $\text{C}_{51}\text{H}_{33}\text{F}_{18}\text{O}_8\text{P}_2\text{Tb}$: C 45.83, H 2.49, N 0.00; found: C 45.66, H 2.55, N 0.00.

Synthesis of TbX nanocrystals:



Scheme 5-5. Reaction scheme of TbX nanocrystals.

Under N_2 atmosphere, precursor Tb(III) complex ($[\text{Tb}(\text{acac})_3(\text{CH}_3\text{OH})_2]$, $[\text{Tb}(\text{acac})_3(\text{tppo})_2]$, $[\text{Tb}(\text{hfa})_3(\text{CH}_3\text{OH})_2]$ or $[\text{Tb}(\text{hfa})_3(\text{tppo})_2]$, 0.5 mmol) was dissolved into oleylamine (15 mL, 46 mmol), and the mixture was heated at 300°C for 3 h while stirring. Then, the resulting liquid was centrifuged at 4000 rpm for 10 min. The precipitate was added to *n*-hexane (10 mL) and ethanol (20 mL), and centrifuged at 4000 rpm for 10 min. The solvent was decanted, and this washing treatment was carried out for four times. The white powder were separated and redispersed by *n*-hexane (20 mL).

5.2.4 Preparation of Polymer Thin Films

The obtained TbX nanocrystals (2 mg) were added to a solution of polymethylmethacrylate (PMMA) (2.0 g) in chloroform (8 mL) and dispersed well

under ultrasonic treatment, giving a colloidal suspension. The PMMA thin films were prepared on a glass substrate from the colloidal suspension by means of a casting method for the Faraday rotation measurements.

The Faraday rotation measurements were performed using a measurement system for Faraday and Kerr effects (JASCO, Model K-250). A Xe lamp was used as the light source. The external magnetic field was 15000 Oe.

5.3 Results and Discussion

5.3.1 Preparation of TbX Nanocrystals

Single source Tb(III) complexes, $[\text{Tb}(\text{acac})_3(\text{CH}_3\text{OH})_2]$, $[\text{Tb}(\text{acac})_3(\text{tppo})_2]$, $[\text{Tb}(\text{hfa})_3(\text{CH}_3\text{OH})_2]$, and $[\text{Tb}(\text{hfa})_3(\text{tppo})_2]$, were synthesized by the reacting terbium acetate with β -diketone, methanol, and tppo ligands. Their chemical structures were identified using IR spectra and elemental analysis. The TG profiles of the Tb(III) complexes are shown in Figure 5-1. $[\text{Tb}(\text{acac})_3(\text{CH}_3\text{OH})_2]$ and $[\text{Tb}(\text{hfa})_3(\text{CH}_3\text{OH})_2]$ decomposed at around 100°C, resulting in the elimination of coordinated methanol molecules. The percentage weight-losses were 14% and 7%, respectively. The mass of $[\text{Tb}(\text{acac})_3(\text{CH}_3\text{OH})_2]$ decreased gradually with increasing temperature between 100°C and 500°C. In contrast, $[\text{Tb}(\text{hfa})_3(\text{CH}_3\text{OH})_2]$ decomposed at about 150°C. The decomposition temperatures of $[\text{Tb}(\text{acac})_3(\text{tppo})_2]$ and $[\text{Tb}(\text{hfa})_3(\text{tppo})_2]$ were found to be 235°C and 276°C, respectively. The characteristic weight-loss of $[\text{Tb}(\text{hfa})_3(\text{tppo})_2]$ at around 300°C, found to be 95%, might have been caused by sublimation of the Tb complex.

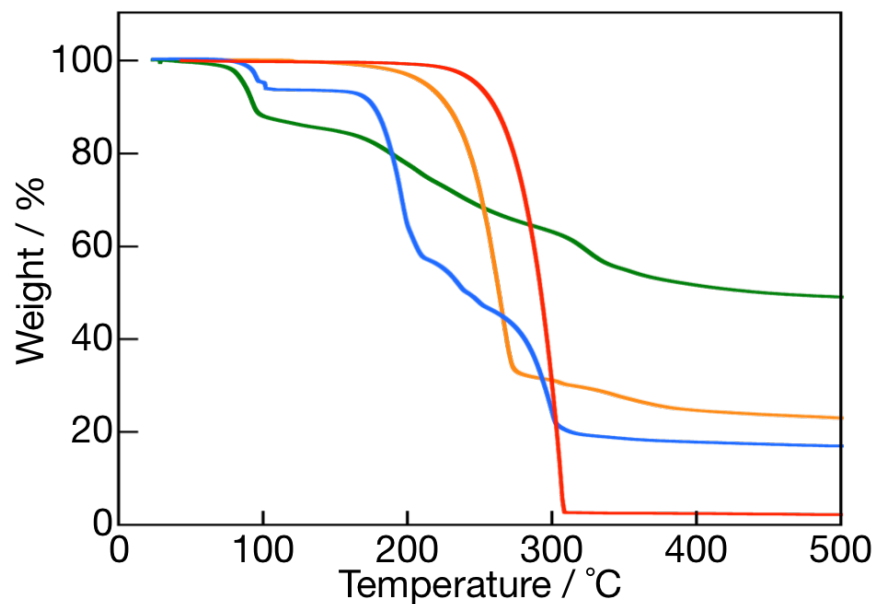


Figure 5-1. Thermogravimetric profiles of $[\text{Tb}(\text{acac})_3(\text{CH}_3\text{OH})_2]$ (green), $[\text{Tb}(\text{acac})_3(\text{tppo})_2]$ (yellow), $[\text{Tb}(\text{hfa})_3(\text{CH}_3\text{OH})_2]$ (blue) and $[\text{Tb}(\text{hfa})_3(\text{tppo})_2]$ (red).

TbX nanocrystals (TbX1, 2, 3 and 4) were prepared via the thermal reaction of single source precursor Tb(III) complexes, $[\text{Tb}(\text{acac})_3(\text{CH}_3\text{OH})_2]$, $[\text{Tb}(\text{acac})_3(\text{tppo})_2]$, $[\text{Tb}(\text{hfa})_3(\text{CH}_3\text{OH})_2]$, and $[\text{Tb}(\text{hfa})_3(\text{tppo})_2]$, respectively, at 300 °C for 3 h. To estimate the effect of decomposition temperature, the author synthesized TbX nanoparticles using same conditions at 280 °C. The prepared powders were separated by centrifugation and washed four times with *n*-hexane and ethanol. After washing, a white TbX nanocrystals powder coated with oleylamine molecules was obtained. The amount of oleylamine was estimated using TG-DTA (Figure 5-2). The author could not observe an effective weight loss in the TbX nanoparticles until 550 °C. According to these results, TbX nanoparticles were modified by small amounts of oleylamine, and oleylamine might have no influence on the Faraday effects of TbX nanoparticles.

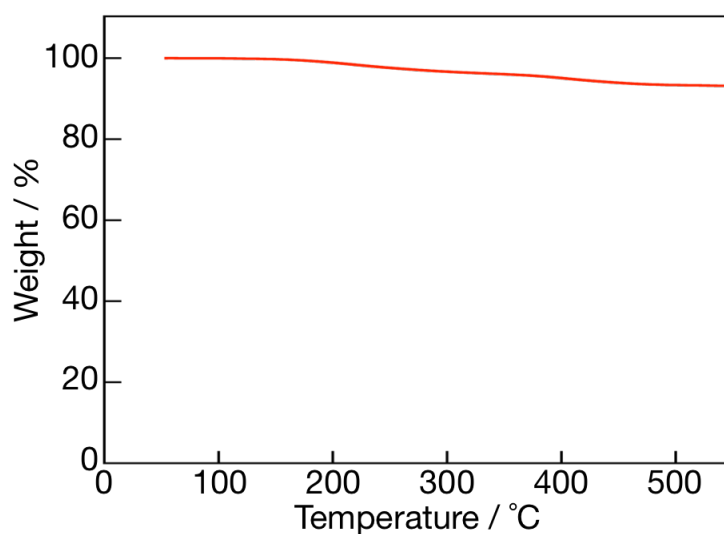


Figure 5-2. Thermogravimetric profiles of TbX3 nanoparticles.

The powder XRD patterns of TbX1, 2, 3, and 4 are shown in Figure 5-3. The diffraction peaks of TbX1 and 2 at $2\theta = 20.2, 28.1, 32.5, 48.1,$ and 57.0 degree were similar to the (211), (222), (400), (440), and (622) planes, respectively, of the cubic phase of Tb_2O_3 (ICDD 01-076-0156, $I2_13$). The calculated lattice constant of TbX1 and 2 was 10.84 \AA (lattice constant of $Tb_2O_3 = 10.72 \text{ \AA}$). The broadening and small shifts of the XRD signals might be ascribed to the amorphous phase of Tb-O lattices including impurities. The diffraction peaks of TbX3 at $2\theta = 28.0, 32.0, 45.7, 46.1, 54.8,$ and 66.8 degree were assigned to the (012), (104), (018), (110), (116), and (208) planes, respectively, of trigonal TbOF (ICDD 01-085-0851, $R-3m$). In the case of decomposition at 280°C , the resultant TbX nanoparticles contained residual products. Accordingly, 300°C might be suitable for the decomposition of Tb complexes. In contrast, the diffraction peaks of TbX4 were different from those of Tb_2O_3 , TbOF, and orthorhombic TbF_3 (ICDD 01-084-0179, $Pnma$) crystals. These peaks at $2\theta = 25.1, 25.8,$

28.8, 36.5, 45.7, 47.0, 53.1, and 55.0 degree agreed well with those of the (002), (110), (111), (112), (300), (113), (302), and (221) planes, respectively, of hexagonal SmF_3 (ICDD 01-072-1439, $P6_322$). The calculated lattice constants of TbX4 were $a = 7.19 \text{ \AA}$ and $c = 7.24 \text{ \AA}$ (lattice constants of SmF_3 , $a = 6.99 \text{ \AA}$ and $c = 7.16 \text{ \AA}$). Thermal decomposition of $[\text{Tb}(\text{hfa})_3(\text{tppo})_2]$ in oleylamine at 300°C might lead to formation of the hexagonal structure of TbF_3 lattice with slightly increased lattice constants. EDS and XPS confirmed the presence of fluorine atoms in the TbX3 and 4 nanocrystals (Figures 5-4 and 5-5). The elementary Tb/F ratios of TbX3 and 4 were estimated using EDS spectra. The Tb/F ratios of TbX3 and 4 were 1.11 and 0.75, respectively. These results were higher than the stoichiometric ratio, 1.0 (TbOF) and 0.33 (TbF_3), respectively. The author considered that TbX3 and 4 might be formed partly from Tb_2O_3 crystals. The FWHM of the $2\theta = 48.1$, 32.0 , and 28.8 degree peaks, which correspond to Bragg diffraction from Tb_2O_3 (440), TbOF (012) and TbF_3 (111) planes, respectively. The TbX1, 2, 3 and 4 crystallite sizes calculated using the Scherrer equation from the XRD data using the Scherrer equation were 6.3, 6.5, 11.0, and 10.3 nm, respectively.

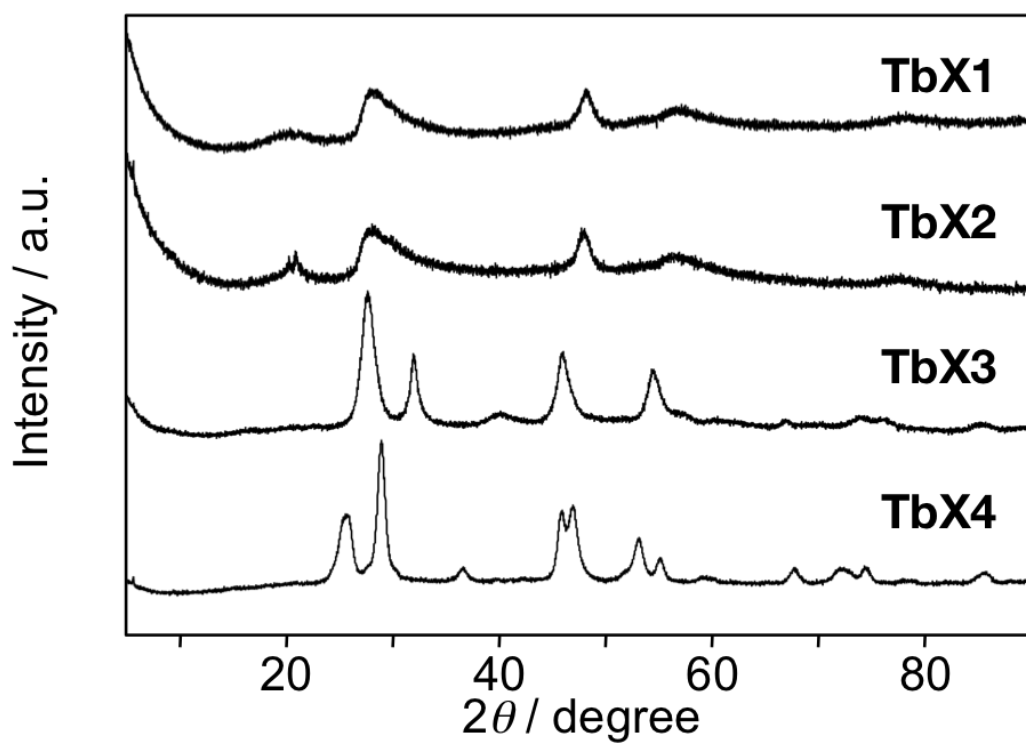


Figure 5-3. XRD patterns of TbX1, 2, 3 and 4 nanocrystals.

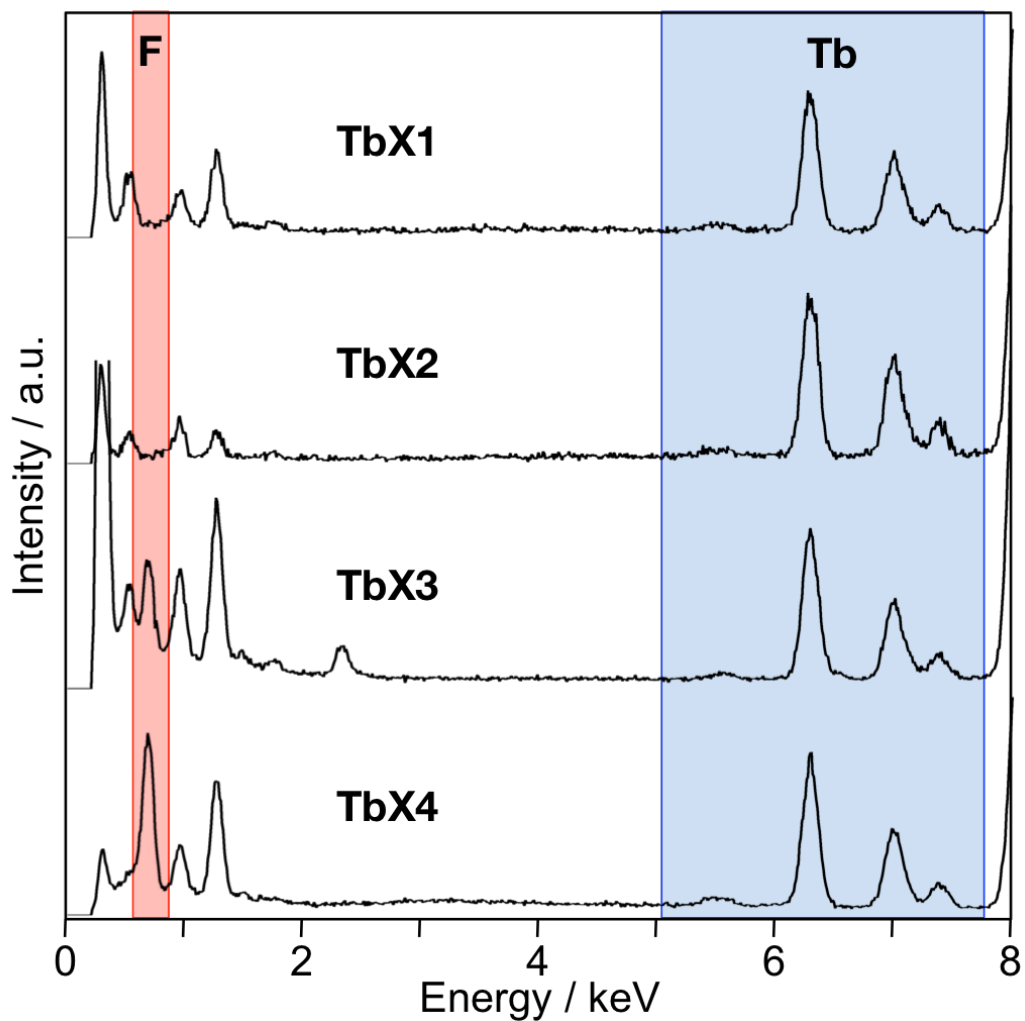


Figure 5-4. The energy dispersive X-ray analysis (EDX) spectra of TbX1, 2, 3 and 4 nanocrystals. The EDX spectra confirmed the presence of Tb of all TbX nanocrystals (blue region). On the other hand, the absence (TbX1 and 2) and presence (TbX3 and 4) of fluorine were observed (red region).

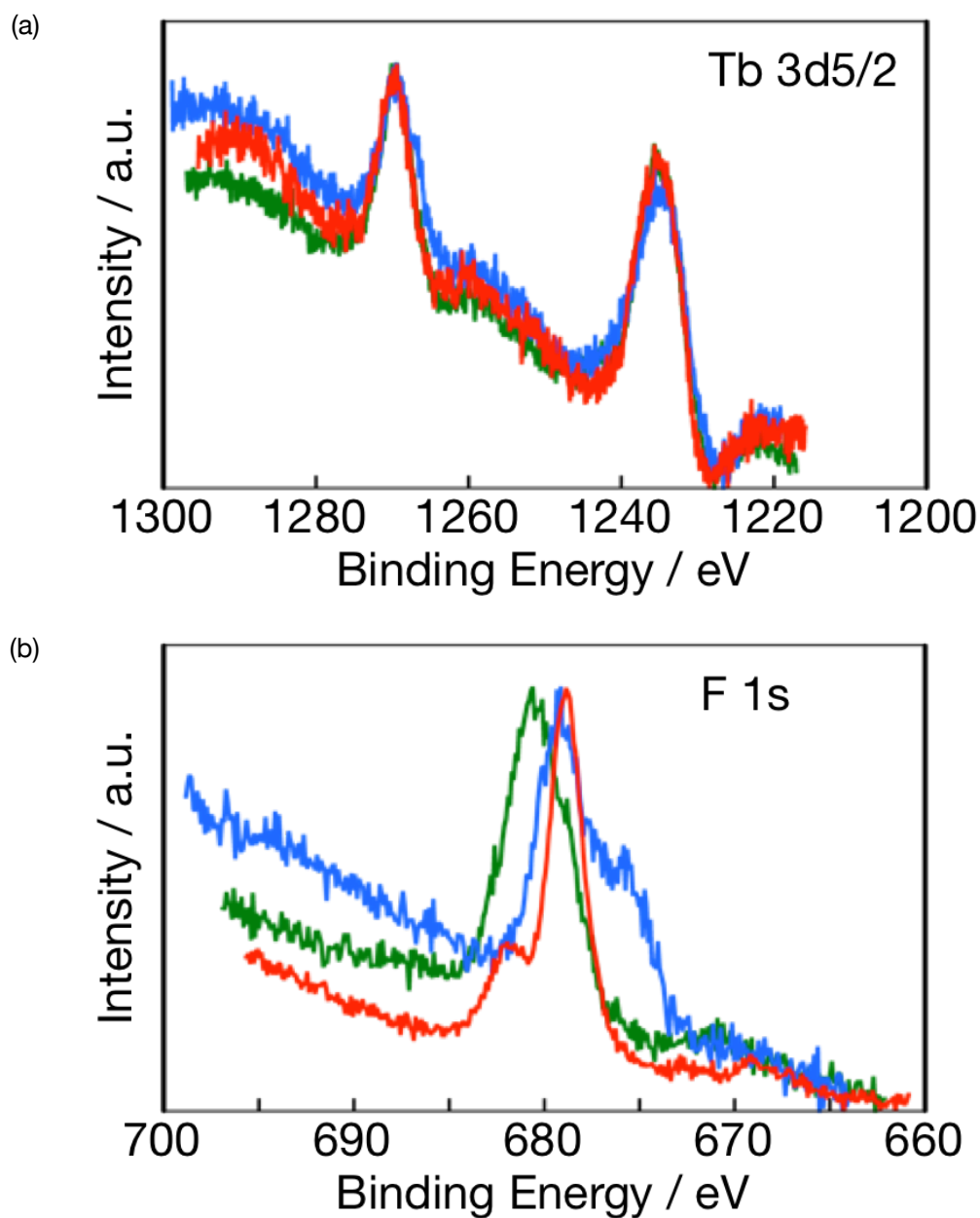


Figure 5-5. X-ray photoelectron spectra of [Tb(hfa)₃(tppo)₂] (green), TbX3 (blue) and TbX4 nanocrystals (red). In order to correct the charge shift, all samples were coated with evaporated gold, and charge shift corrections were made on all samples by assuming a Au 4f_{7/2} signal of 83.0 eV. The author compared electron state of terbium and fluorine between TbX3, TbX4 nanocrystals and [Tb(hfa)₃(tppo)₂] as a precursor complex by using XPS. In the result, electron state of Tb 3d_{5/2} shows same binding energy in all samples. In contrast, electron state of F 1s shows difference binding energy between complex (680.7 eV) and nanocrystal (679.0 eV) due to stabilization of crystallization.

TEM images of TbX1, 2, 3, and 4 are shown in Figure 5-6. The TEM images of TbX1 and 2 show cloud-liked aggregations without clear particle shapes. The TEM images of TbX3 and 4 show spherical TbX nanocrystals of various sizes. The average particle sizes of TbX3 and 4 were 7.1 and 8.8 nm, respectively. Previously, the formation of LnOF and LnF₃ nanocrystals (Ln = Ce, Nd, Sm, Gd, Ho, and Yb) from lanthanide trifluoroacetates has been reported^[22,23]. The introduction of fluorine atoms in Tb compounds might be caused by the elimination of fluorine anions from the trifluoromethyl groups of the organic ligands. The author successfully synthesized Tb₂O₃, TbOF, and TbF₃ nanocrystals using single source precursors, [Tb(acac)₃(CH₃OH)₂], [Tb(acac)₃(tppo)₂], [Tb(hfa)₃(CH₃OH)₂] and [Tb(hfa)₃(tppo)₂], respectively.

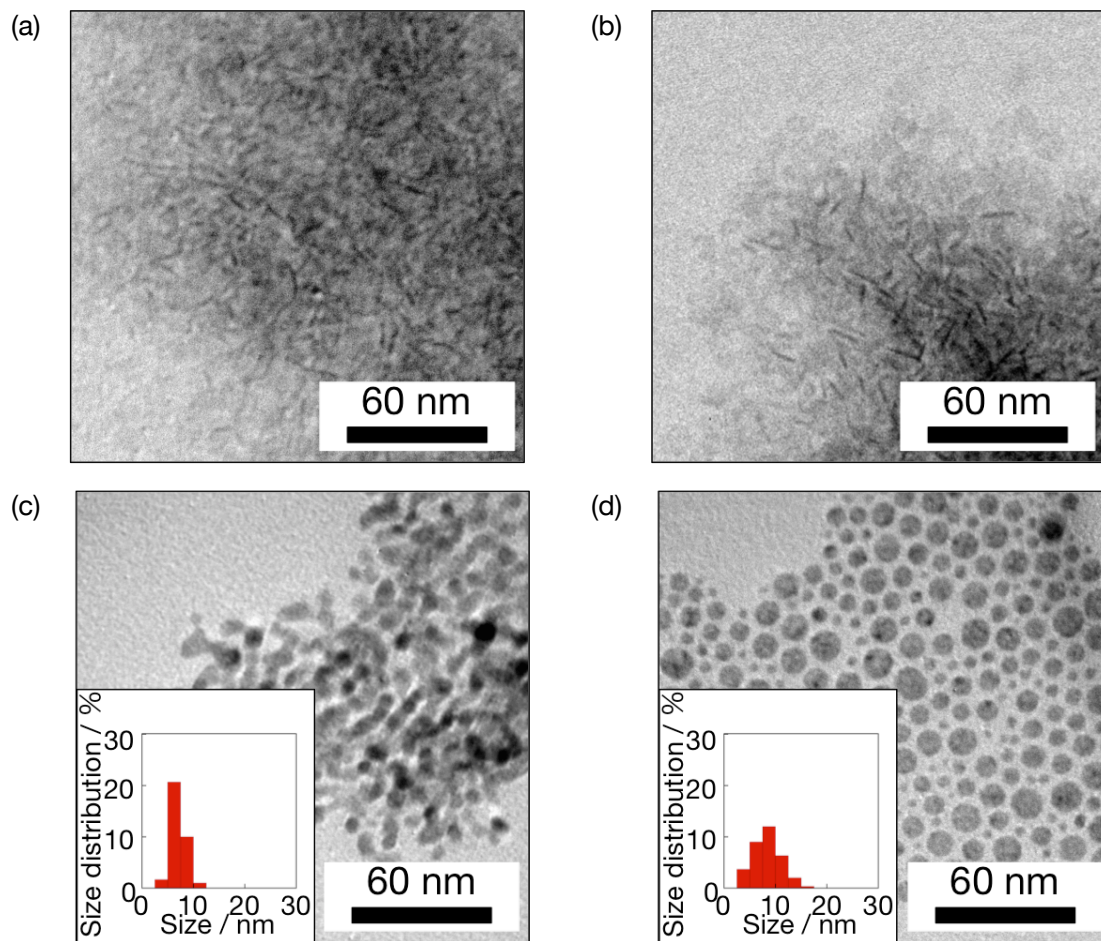


Figure 5-6. TEM images of (a) TbX1, (b) TbX2, (c) TbX3 and (d) TbX4 nanocrystals. Insets in Figure 5-6c and d show size distribution histogram of TbX3 and TbX4 nanocrystals, respectively.

5.3.2 Absorption and magneto-optical properties of TbX nanocrystals

The TbX nanocrystals were dispersed homogeneously in *n*-hexane. The absorption spectra of TbX3 and 4 nanocrystals in *n*-hexane are shown in Figure 5-7. Intense absorption between 230 and 330 nm was observed in the solutions of both TbX3 and TbX4. These peaks are due to $4f^8 \rightarrow 4f^75d$ transitions, with their exact positions being dependent on the crystal field of the lattice^[24,25]. In addition, a weak broad band between 400 and 600 nm would be indicative of the presence of Tb(IV) ions.

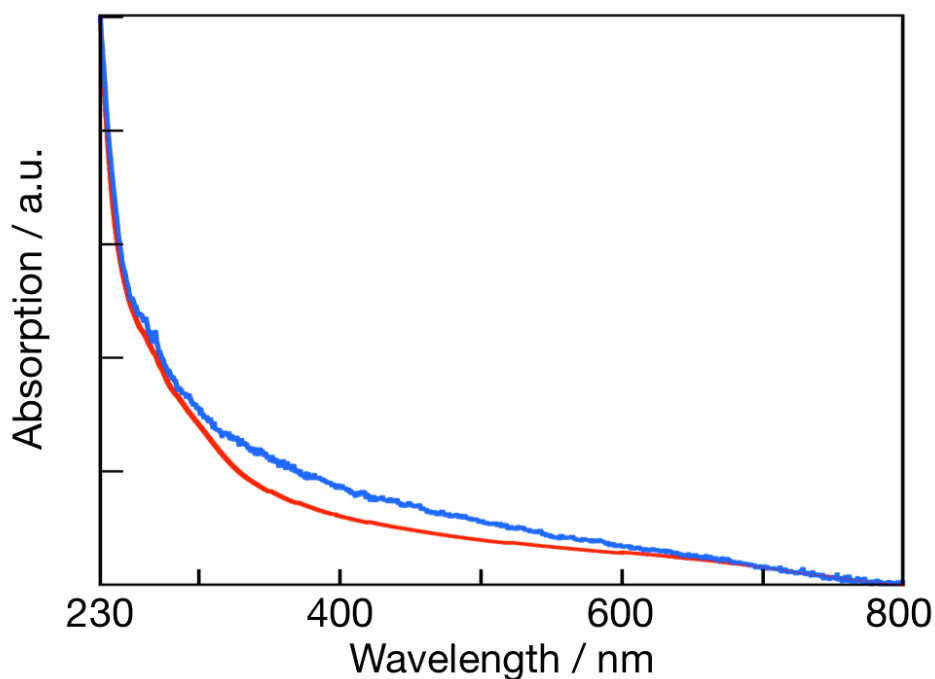


Figure 5-7. UV-Vis absorption spectra of the *n*-hexane solution containing TbX3 (blue) and TbX4 (red).

To evaluate the magneto-optical properties of TbX (TbX1, TbX2, TbX3 and TbX4) nanocrystals, PMMA thin films containing TbX nanocrystals were prepared. The TbX nanoparticles and PMMA were well dispersed in chloroform under ultrasonic treatment, and the prepared PMMA thin films with TbX nanoparticles showed high transparency in the visible region (Figure 5-8).

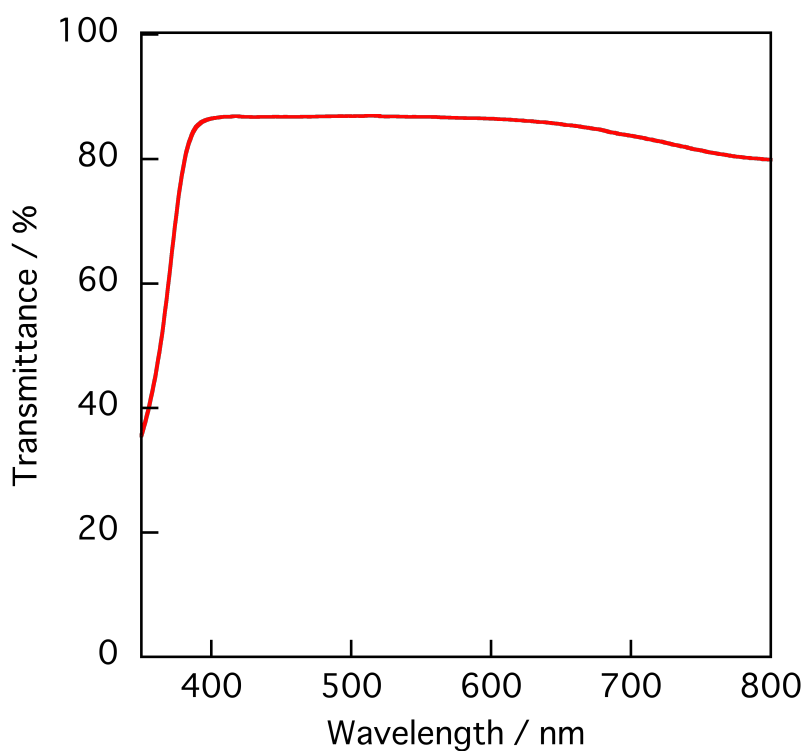


Figure 5-8. Transmittance spectrum of PMMA thin films containing TbX3 nanoparticles. It shows no characteristic peak in visible region. This result means that large aggregation doesn't exist in the PMMA thin films.

The thickness of the PMMA thin films containing TbX1, 2, 3, and 4 nanocrystals were 330, 360, 460 and 270 μm , respectively. The wavelength dependence of the Faraday rotation angle was measured for the PMMA thin films containing the TbX nanocrystals. The Faraday rotation spectrum at room temperature under an external magnetic field of 15,000 Oe showed clear negative peaks. The Verdet constant, which indicates the strength of Faraday rotation, was calculated by using Equation (5-1), in which θ , H , and l denote the Faraday rotation angle, external magnetic field, and thickness of the thin film, respectively.

$$V = \theta/Hl \quad (5-1)$$

Here, the author normalized the Verdet constant in proportion to the Tb ion concentrations, which were estimated by ICP-AES, thus defining the Verdet constant normalized by Tb ion concentrations (V_c) as follows.

$$V_c = \theta/HlC \quad (5-2)$$

where C is the Tb ion concentration in the PMMA thin films containing TbX nanocrystals. The calculated V_c constants are shown in Figure 5-9 and Table 5-1. The V_c values of TbX1 (-0.24×10^{-4} degree Oe $^{-1}$ cm $^{-1}$ mol $^{-1}$ L), TbX2 (-0.33×10^{-4} degree Oe $^{-1}$ cm $^{-1}$ mol $^{-1}$ L), TbX3 (-4.83×10^{-4} degree Oe $^{-1}$ cm $^{-1}$ mol $^{-1}$ L), and TbX4 (-1.65×10^{-4} degree Oe $^{-1}$ cm $^{-1}$ mol $^{-1}$ L) at 445 nm are much higher than those of the corresponding

mono-nuclear Tb(III) complex, [Tb(hfa)₃(tppo)₂] ($V_c = -0.02 \times 10^{-4}$ degree Oe⁻¹ cm⁻¹ mol⁻¹ L). The enhancement of the Faraday effects of TbX1, 2, 3, and 4 might have been caused by the enhancement of magnetic exchange interaction between Tb atoms in Tb-O or Tb-F lattice structures. The author considered that the values of V_c to depend on the distance between Tb atoms (Figure 5-10). The distance between Tb atoms in trigonal TbOF (3.84 Å measured using CIF of LaOF crystals, Identifier 9009071, *R-3m*) is shorter than that in hexagonal TbF₃ (4.04 Å measured using CIF of SmF₃ crystals, Identifier 1010986, *P6₃22*). Thus, the author considered that TbX3 (TbOF) shows a higher maximum V_c than TbX4 (TbF₃).

The Verdet constant can be also divided into three parts, Faraday A-, B-, and C-terms^[26,27], in particular, the Faraday rotation angle of a lanthanide(III) ion that has a degenerate ground state is theoretically represented by the Faraday C-term given by Equation (5-3), in which g , χ , and J are the Landé splitting factor, magnetic susceptibility, and the total angular momentum quantum number, respectively^[16,28].

$$\theta \propto g\chi/(2J + 1) \quad (5-3)$$

Of the lanthanide(III) ions Gd(III) shows the highest value of $g\chi/(2J + 1)$. The author considered that the enhanced Faraday rotations of TbX3 and 4 might be affected by the presence of small amount of Tb(IV) ions in the TbX3 and 4 nanocrystals.

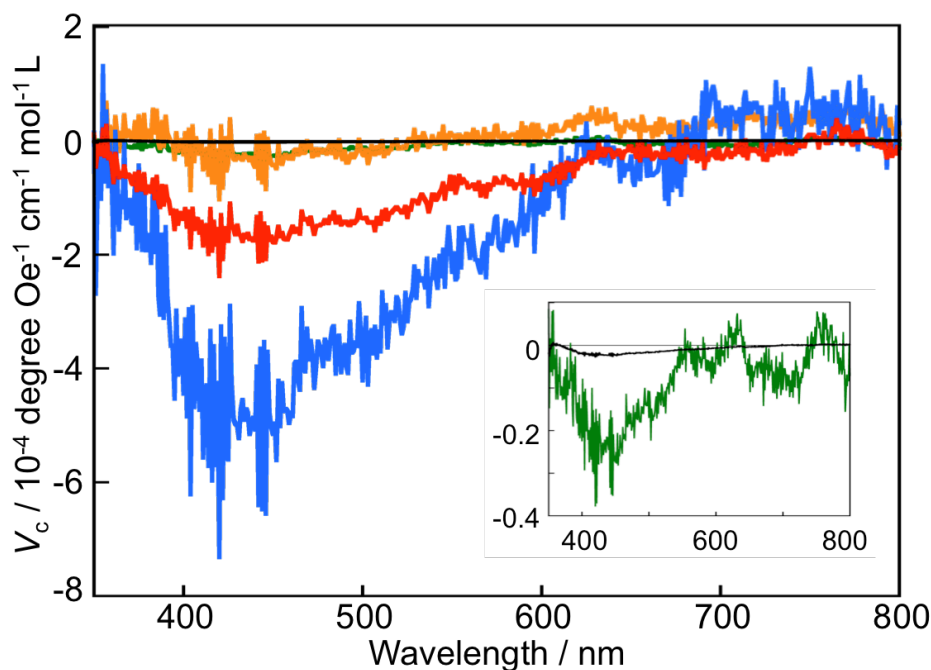


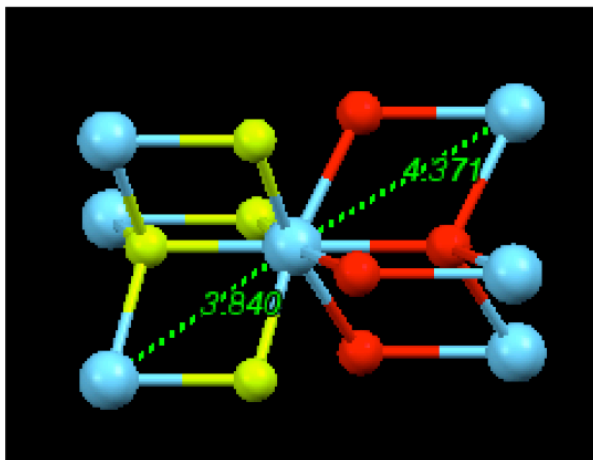
Figure 5-9. The calculated V_c constants of the PMMA thin films containing $[\text{Tb}(\text{hfa})_3(\text{tppo})_2]$ (black), TbX1 (green), 2 (yellow), 3 (blue) and 4 (red) under an external magnetic field of 15000 Oe. Inset shows the magnified V_c constants of the PMMA thin films containing $[\text{Tb}(\text{hfa})_3(\text{tppo})_2]$ (black) and TbX1 (green).

Table 5-1. Particle sizes, peak positions and normalized Verdet constants of $[\text{Tb}(\text{hfa})_3(\text{tppo})_2]$, Tb1, 2, 3 and 4 nanocrystals.

sample	compound	Particle size ^{b)} / nm	V_c peak	$V_c^c)$
			position ^{c)} λ_{max} / nm	/ 10^{-4} degree Oe ⁻¹ cm ⁻¹ mol ⁻¹ L
$[\text{Tb}(\text{hfa})_3(\text{tppo})_2]$	Tb complex ^{a)}	-	445	-0.02
TbX1	Tb_2O_3	6.3	445	-0.24
TbX2	Tb_2O_3	6.5	445	-0.33
TbX3	TbOF	11.0	445	-4.83
TbX4	TbF_3	10.3	445	-1.65

a) The X-ray single crystal structure of $[\text{Ln}(\text{hfa})_3(\text{tppo})_2]$ is shown in reference^[29]. b) Calculated by Scherer equation from the XRD data. c) The thickness of the PMMA thin film containing TbX1, 2, 3 and 4 nanocrystals were 330, 360, 460 and 270 μm . The external magnetic field: 15000 Oe.

(a) LaOF (9009071, $R\bar{3}m$)



(b) SmF₃ (1010986, $P6_322$)

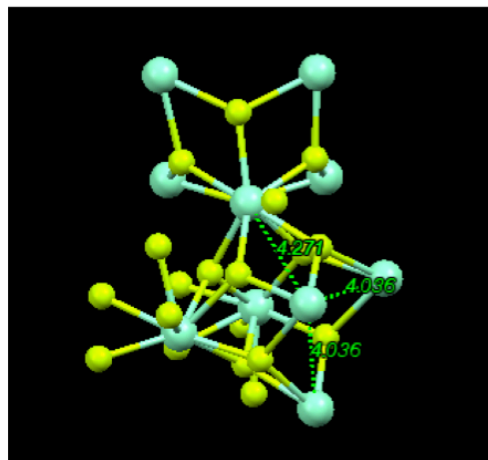


Figure 5-10. Lattice images based on the CIF data of (a) LaOF (9009071, $R\bar{3}m$) and (b) SmF₃ (1010986, $P6_322$). The blue, yellow, and red spheres in Figure are Lanthanide (La or Sm), fluorine (F), and oxygen atoms.

5.4 Conclusions

The author successfully synthesized TbX (Tb₂O₃, TbOF, and TbF₃) nanocrystals via thermal decomposition of single-source Tb(III) complexes [Tb(acac)₃(CH₃OH)₂], [Tb(acac)₃(tppo)₂], [Tb(hfa)₃(CH₃OH)₂], and [Tb(hfa)₃(tppo)₂]. In particular, Tb(III) complexes with fluorine atoms, [Tb(hfa)₃(CH₃OH)₂] and [Tb(hfa)₃(tppo)₂] provided TbOF and TbF₃ nanocrystals, respectively, for the first time. These methods using Tb(hfa)₃ derivatives are superior to those reported previously for LnOF and LnF₃ (Ln = Ce, Nd, Sm, Gd, Ho, and Yb) due to simple and safe preparation procedure involved. The prepared TbX₃ (TbOF) and TbX₄ (TbF₃) nanocrystals show effective Faraday rotation under a magnetic field. One of the reasons for the higher maximum V_c of TbX₃ (TbOF) is that the distance between Tb atoms in trigonal TbOF is smaller than the corresponding distance in hexagonal TbF₃. Moreover, the author is now trying to observe the evidence of Tb(IV) in TbX₃ and 4 using magnetic measurements. These TbX nanocrystals are expected to open up a new frontier field involving inorganic chemistry, photophysical chemistry, material science, and optical device engineering and technology.

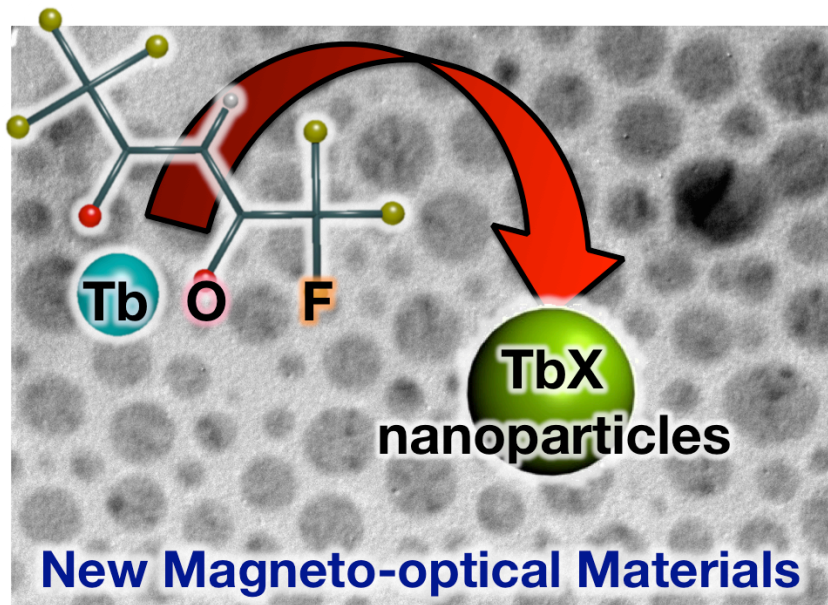


Figure 5-11. Illustration of the formation of TbX nanoparticles.

5.5 References

- 1 I. N. Duling, III, *Electronics Letters* **1991**, 27, 544-545.
- 2 N. Stafford, *Nature* **2010**, 467, S19-S21.
- 3 L. Bi, J. Hu, P. Jiang, D. H. Kim, G. F. Dionne, L. C. Kimerling, and C. A. Ross, *Nature Photonics* **2011**, 5, 758-762.
- 4 Y.-w. Jun, Y.-y. Jung, and J. Cheon, *Journal of the American Chemical Society* **2002**, 124, 615-619.
- 5 Y. Wang, N. Herron, K. Moller, and T. Bein, *Solid State Communications* **1991**, 77, 33-38.
- 6 D. J. Norris, N. Yao, F. T. Charnock, and T. A. Kennedy, *Nano Letters* **2000**, 1, 3-7.
- 7 N. S. Norberg, K. R. Kittilstved, J. E. Amonette, R. K. Kukkadapu, D. A. Schwartz, and D. R. Gamelin, *Journal of the American Chemical Society* **2004**, 126, 9387-9398.
- 8 S. C. Erwin, L. Zu, M. I. Haftel, A. L. Efros, T. A. Kennedy, and D. J. Norris, *Nature* **2005**, 436, 91-94.
- 9 N. Rajamanickam, R. N. Mariammal, S. Rajashabala, and K. Ramachandran, *Journal of Alloys and Compounds* **2014**, 614, 151-164.
- 10 P. Wachter, *CRC Critical Reviews in Solid State Sciences* **1972**, 3, 189-241.
- 11 T. Kasuya, *Journal of Magnetism and Magnetic Materials* **1999**, 195, 141-147.
- 12 T. Kataoka, Y. Tsukahara, Y. Hasegawa, and Y. Wada, *Chemical*

- Communications* **2005**, 6038-6040.
- 13 Y. Hasegawa, T. Adachi, A. Tanaka, M. Afzaal, P. O'Brien, T. Doi, Y. Hinatsu, K. Fujita, K. Tanaka, and T. Kawai, *Journal of the American Chemical Society* **2008**, *130*, 5710-5715.
- 14 T. Nakanishi, M. Maeda, A. Kawashima, S. Kamiya, K. Fushimi, K. Fujita, K. Tanaka, and Y. Hasegawa, *Journal of Alloys and Compounds* **2013**, *562*, 123-127.
- 15 Y. Hasegawa, M. Maeda, T. Nakanishi, Y. Doi, Y. Hinatsu, K. Fujita, K. Tanaka, H. Koizumi, and K. Fushimi, *Journal of the American Chemical Society* **2013**, *135*, 2659-2666.
- 16 K. Miyamoto, K. Isai, M. Suwa, and H. Watarai, *Journal of the American Chemical Society* **2009**, *131*, 6328-6329.
- 17 W. Li, K. Zou, M. Lu, B. Peng, and W. Zhao, *International Journal of Applied Ceramic Technology* **2010**, *7*, 369-374.
- 18 P. Chen and R. K. Li, *Journal of Alloys and Compounds* **2015**, *622*, 859-864.
- 19 J. Liu, F. Guo, B. Zhao, N. Zhuang, Y. Chen, Z. Gao, and J. Chen, *Journal of Crystal Growth* **2008**, *310*, 2613-2616.
- 20 V. Vasyliiev, P. Molina, M. Nakamura, E. G. Villora, and K. Shimamura, *Optical Materials* **2011**, *33*, 1710-1714.
- 21 T. Nakanishi, Y. Suzuki, Y. Doi, T. Seki, H. Koizumi, K. Fushimi, K. Fujita, Y. Hinatsu, H. Ito, K. Tanaka, and Y. Hasegawa, *Inorganic Chemistry* **2014**, *53*, 7635-7641.

- 22 Y.-W. Zhang, X. Sun, R. Si, L.-P. You, and C.-H. Yan, *Journal of the American Chemical Society* **2005**, *127*, 3260-3261.
- 23 X. Sun, Y.-W. Zhang, Y.-P. Du, Z.-G. Yan, R. Si, L.-P. You, and C.-H. Yan, *Chemistry – A European Journal* **2007**, *13*, 2320-2332.
- 24 W. T. Carnall, P. R. Fields, and K. Rajnak, *The Journal of Chemical Physics* **1968**, *49*, 4412-4423.
- 25 G. Wakefield, H. A. Keron, P. J. Dobson, and J. L. Hutchison, *Journal of Physics and Chemistry of Solids* **1999**, *60*, 503-508.
- 26 A. D. Buckingham and P. J. Stephens, *Annual Review of Physical Chemistry* **1966**, *17*, 399-432.
- 27 P. J. Stephens, *Annual Review of Physical Chemistry* **1974**, *25*, 201-232.
- 28 L. D. Barron, *Molecular Light Scattering and Optical Activity*. 311-324, Cambridge University Press.
- 29 Y. Hasegawa, M. Yamamuro, Y. Wada, N. Kanehisa, Y. Kai, and S. Yanagida, *The Journal of Physical Chemistry A* **2003**, *107*, 1697-1702.

Chapter 6

Summary

Hybrid nano-assemblies composed of different nanocrystals and photo-functional molecules are expected not only to combine the properties of the constituent building blocks but also to generate new, collective phenomena based on interparticle interactions at the nanoscale. In this thesis, the synthesis and surface functionalization of magneto-optical lanthanide nanocrystals have been described. The results obtained in this study are summarized briefly below.

In Chapter 1, the scientific background about lanthanide magnetic semiconductor nanocrystals was provided. Studies on the magneto-optical properties of europium chalcogenide nanocrystals were introduced as well. Then, strategies for forming nano-assemblies of lanthanide nanocrystals, metal nanocrystals, and linker molecules as building blocks were described.

In Chapter 2, photo-functional naphthalenedithiol (1,4-bisdecane-thio-naphthalene: NpDDT) was used as a linker molecule to form EuS nano-assemblies. The

formation of EuS nano-assemblies using NpDDT linkers was confirmed using TEM and UV-vis absorption measurements. The peak position and angle of Faraday rotation were found to depend on the ligand replacement time of oleylamine to NpDDT on the surface of EuS nanocrystals and the subsequent formation of EuS nano-assemblies. Additionally, the emission quantum yields of naphthalene units in NpDDT were found to depend on the aggregation size of EuS nano-assemblies. According to these results, the NpDDT molecule is expected to be a sensing linker unit for analysis of EuS nano-assemblies.

In Chapter 3, EuS nanocrystals linked directly with gold nanocrystals (EuS-Au nanosystems) were synthesized successfully. The distance between the EuS and the Au nanocrystals was controlled accurately using the organic molecules 1,2-ethanedithiol (EDT), 1,6-hexanedithiol (HDT), 1,10-decanedithiol (DDT), 1,4-bisethanethionaphthalene (NpEDT), and NpDDT. The magneto-optical properties of a EuS-Au nanosystem depend on the interparticle distance between EuS and Au and the size of the Au nanoparticles. The enhanced spin-polarization of the EuS-Au nanosystems excited at the LSPR band of the Au nanoparticles was confirmed by photo-assisted EPR spectroscopy. The results obtained in this chapter will provide new EuS-Au nanosystems with amplified Faraday rotation under irradiation in the plasmon band of the gold parts.

In Chapter 4, novel photo-switching Faraday effects of EuS-Au nanosystems were demonstrated. The Faraday effects of the toluene solution containing EuS-Au nanosystems were estimated using a MCD measurement system equipped with a visible light irradiation system (> 440 nm). The author found a drastic change in the absorption

band and the MCD signal of the EuS-Au nanosystems under irradiation. Additionally, effective reversible changes in the MCD spectra at 670 nm under alternating irradiation cycles of visible light (> 440 nm) and dark were shown. These results imply that the effective change in the MCD spectra of the EuS-Au nanosystems would be dominated not only by a drastic change in the absorption band related to the enhanced LSPR of Au nanoparticles but also by specific interactions between EuS and Au in the nanosystem under irradiation.

In Chapter 5, novel nano-materials composed of Tb lattice structures, TbX nanocrystals (terbium oxides (Tb_2O_3), terbium fluorides (TbF_3) and terbium oxyfluorides (TbOF)), were synthesized successfully via thermal decomposition of single-source precursors Tb(III) complex $[\text{Tb}(\text{acac})_3(\text{CH}_3\text{OH})_2]$, $[\text{Tb}(\text{acac})_3(\text{tppo})_2]$, $[\text{Tb}(\text{hfa})_3(\text{CH}_3\text{OH})_2]$, and $[\text{Tb}(\text{hfa})_3(\text{tppo})_2]$. In particular, Tb(III) complexes with fluorine atoms, $[\text{Tb}(\text{hfa})_3(\text{CH}_3\text{OH})_2]$ and $[\text{Tb}(\text{hfa})_3(\text{tppo})_2]$, provided TbOF or TbF_3 nanocrystals for the first time. These methods using $\text{Tb}(\text{hfa})_3$ derivatives are superior to those reported previously for LnOF and LnF_3 ($\text{Ln} = \text{Ce}, \text{Nd}, \text{Sm}, \text{Gd}, \text{Ho}, \text{and Yb}$) given the simple and safe preparation procedures involved. The prepared TbOF and TbF_3 nanocrystals showed effective Faraday rotation under magnetic field.

A variety of nano-assemblies composed of semiconductors, metals, and magnetic nanocrystals have been studied extensively. However, magnetic semiconductor nano-assemblies may not have been studied extensively because few classes of materials exhibit both intrinsic magnetic and semiconducting properties. In

this thesis, the formation of lanthanide magnetic semiconductor nano-assemblies with photo-functional linker molecules and the formation of hybrid nano-systems composed of magnetic semiconductors and metal nanocrystals were demonstrated. Additionally, the synthesis and characterization of novel terbium nanocrystals with magneto-optical properties were described as well. This thesis is the first systematic report on the synthesis and surface-functionalization of magneto-optical lanthanide nanocrystals.

The author believes that the strategies for hybrid nano-assemblies of magneto-optical lanthanide nanocrystals described in this thesis would contribute to the development of applications involving novel magnetic semiconducting devices, such as optical isolators, circulators, photo-switches, hard drives, transistors, and catalysts. The photochemistry of hybrid nano-assemblies of magneto-optical lanthanide nanocrystals is expected to open up new fields of inorganic nanomaterials and photonic science.

List of Publications

- [1] A. Kawashima, T. Nakanishi, K. Fushimi, Y. Hasegawa, “EuS Nano-assemblies Linked with Photo-functional Naphthalenedithiols”, *Molecular Crystals and Liquid Crystals* **2013**, 579, 69–76.
- [2] A. Kawashima, T. Nakanishi, T. Shibayama, S. Watanabe, K. Fujita, K. Tanaka, H. Koizumi, K. Fushimi, Y. Hasegawa, “Enhanced Magneto-optical Properties of Semiconductor EuS Nanocrystals Assisted by Surface Plasmon Resonance of Gold Nanoparticles”, *Chemistry – A European Journal* **2013**, 19, 14438–14445 (Highlighted as frontispiece).
- [3] A. Kawashima, T. Nakanishi, Y. Kitagawa, K. Fushimi, Y. Hasegawa, “Synthesis of TbO_x Nanoparticles from the Thermal Decomposition of Tb(III) Complexes”, *e-Journal of Surface Science and Nanotechnology* **2015**, 13, 23–26.
- [4] A. Kawashima, T. Nakanishi, Y. Kitagawa, K. Fujita, K. Tanaka, K. Fushimi, M. A. Malik, P. O’Brien, Y. Hasegawa, “Terbium Oxide, Fluoride, and Oxyfluoride Nanoparticles with Magneto-optical Properties”, *Bulletin of Chemical Society of Japan* **2015**, 88, 1453–145826.
- [5] A. Kawashima, T. Nakanishi, Y. Kitagawa, K. Fushimi, Y. Hasegawa, “Photo-switchable Faraday Effect in EuS-Au Nanosystems”, *Physica Status Solidi A*, in press.

Other Publications

- [1] Y. Hasegawa, M. Kumagai, A. Kawashima, K. Fujita, K. Tanaka, T. Nakanishi, K. Fushimi, “First Synthesis of EuS Nanoparticle Thin Film with a Wide Energy Gap and Giant Magneto-Optical Efficiency on a Glass Electrode”, *Journal of Physical Chemistry C* **2012**, *116*, 19590–19596.
- [2] T. Nakanishi, M. Maeda, A. Kawashima, S. Kamiya, K. Fujita, K. Tanaka, K. Fushimi, Y. Hasegawa, “Novel Opto-magnetic Silicate Glass with Semiconductor EuS Nanocrystals”, *Journal of Alloys and Compounds* **2013**, *562*, 123–127.
- [3] M. Miyano, T. Nakanishi, S. Wada, Y. Kitagawa, A. Kawashima, K. Fushimi, Y. Morisaki, Y. Chujo, Y. Hasegawa, “Luminescent Silicon Nanoparticles Surface-Modified with Chiral Molecules”, *Journal of Photopolymer Science and Technology*, **2015**, *28*, 255–260.

Patents

- [1] 長谷川靖哉、川島祥、熊谷美那、伏見公志
「Eu(II)化合物及び金属を含有する複合ナノ結晶及び薄膜」
特願 2011-047595、PCT/JP2012/055263（国際特許）
- [2] 中西貴之、長谷川靖哉、前田将司、川島祥、伏見公志
「機能性材料の構造体及び機能性材料の構造体の製造方法」
特願 2011-264892

Awards and Others

- [1] 論文「Enhanced Magneto-optical Properties of Semiconductor EuS Nanocrystals Assisted by Surface Plasmon Resonance of Gold Nanoparticles」において、Chemistry – A European Journal 誌のハイライトに採用
- [2] 平成 25 年 3 月: 北海道大学 物質化学部門 大塚博先生記念賞を受賞
- [3] 平成 25 年 3 月: 新学術領域研究「元素ブロック高分子材料の創出」第 1 回合同修論発表会において優秀発表賞を受賞 「プラズモン電場増強を用いた EuS-Au ナノ複合体の光磁気特性変化」
- [4] 平成 25 年 9 月: 2013 年光化学討論会において優秀学生発表賞 (口頭発表)を受賞 「プラズモン電場増強下における EuS-Au ナノ複合体の光磁気特性変化」
- [5] 平成 25 年 12 月: Nagoya Univ. –Tsinhghua Univ. –Toyota Motor Corp. – Hokkaido Univ. –Guangxi Univ. Joint Symposium において Poster Award を受賞 「Enhanced Faraday effect of EuS nanocrystals with Au nanoparticles」
- [6] 平成 26 年 6 月: The 3rd Frontier Chemistry Center International Symposium において Poster Award を受賞 「Remarkable Faraday Effects of EuS–Au Nanosystems」
- [6] 平成 27 年 6 月: The 11th Korea-Japan Symposium on Frontier Photoscience において Poster Award を受賞 「Magneto-optical Properties of Europium Sulfide Nano-systems Attached with Gold Nanoparticles」

Acknowledgements

I wish to express my sincere gratitude to professor Yasuchika Hasegawa, Laboratory of Advanced Materials Chemistry (AMC Laboratory), Division of Applied Chemistry, Faculty of Engineering, Hokkaido University for his kind guidance, valuable suggestions, and hearty encouragement through this work.

I would like to express my gratitude to professor Kazuhisa Azumi, Graduate School of Engineering, Hokkaido University, and professor Noboru Kitamura, Graduate School of Science, Hokkaido University, for their readings, beneficial discussions and assessments of this thesis.

My sincere thanks extend to associate professor Koji Fushimi, assistant professor Takayuki Nakanishi, and assistant professor Yuichi Kitagawa, Graduate School of Engineering, Hokkaido University, for their kind help and useful advices in AMC Laboratory.

I would like to sincerely thank professor Paul O'Brien and Dr. M. Azad Malik, School of Materials, The University of Manchester, for their helpful suggestions and guidance in studying abroad.

I acknowledge professor Katsuhisa Tanaka and associate professor Koji Fujita,

Graduate school of Engineering, Kyoto University, for Faraday measurements of lanthanide nanocrystals, associate professor Hitoshi Koizumi, Graduate School of Engineering, Hokkaido University, for ESR measurements of EuS-Au nanosystems, professor Seichi Watanabe and associate professor Tamaki Shibayama, Graduate School of Engineering, Hokkaido University, for TEM observations of EuS-Au nanosystems, professor Yukio Hinatsu and assistant professor Yoshihiro Doi, Graduate School of Science, Hokkaido University, for measurements of magnetic properties of terbium nanocrystals, and their kind help.

I would like to take this opportunity to thank for the member of AMC laboratory; Dr. Shin-ichiro Kishimoto, Dr. Kohe Miyata, Lee Jun-seob, Ken-ichiro Matsushita, Mina Kumagai, Harunori Watanabe, Tomoki Ohkubo, Yoko Otogawa, Kazunori Kurauchi, Nao Sato, Yuki Suzuki, Yu Takabatake, Kazune Watanabe, Haruya Ikeyama, Misako Jin, Takeshi Sugawara, Shiori Tateno, Yuichi Hirai, Kazuki Matsui, Kei Yanagisawa, Shun Ohmagari, Masanori Yamamoto, Yudai Yamamoto, Satoshi Wada, Ryosuke Ohno, Tsubasa Okai, Masa-aki Goto, Ayako Nakajima, Shiori Natori, Hajime Nishimura, Tomomi Kanazawa, Sho Hakadama, Takafumi Matsui, Yui Miura, Ryuto Yachi, Mari Miyano, Hiromitsu Onodera, Hisataka Kataoka, Toru Koizuka, Makiko Abe, and Yui Koizumi.

I express appreciation for professor Kazuyuki Ishii and all members of Ishii Laboratory at Institute of Industrial Science, The University of Tokyo, and professor Takashi Kajiwara and all members of Kajiwara laboratory at Graduate School of Humanities and Sciences, Nara Woman's University.

I would like to acknowledge for the supports by Japan Society for the Promotion of Science (Grant-in-Aid for JSPS fellows).

Finally, I am particularly grateful to my family, Atsushi Kawashima, Kumiko Kawashima, and my younger siblings for their perpetual understandings and supports.

December 2015

Akira Kawashima